

**UNIVERSITÉ DU QUÉBEC À CHICOUTIMI**

**MEMOIRE PRESENTE A  
L'UNIVERSITÉ DU QUÉBEC À CHICOUTIMI  
COMME EXIGENCE PARTIELLE  
DE LA MAÎTRISE EN INGÉNIERIE**

**PAR  
GAOFENG LI**

**EFFECT OF TRACE ELEMENTS V AND NI ON  
FE INTERMETALLIC PHASES FORMATION AND  
DISTRIBUTION IN DC CAST 5XXX SERIES AL INGOTS**

**JANUARY 2012**

## Abstract

AA5657 alloy is one of the important members of 5xxx-series alloys. It has application in many fields as packing, electricity, architectural, and printing. These applications require high quality surface finishing, and the alloy ingots require homogeneous microstructure. In the industry of DC (direct-chill) casting of 1xxx and 5xxx-series aluminium ingots, there exist different cooling rates from the casting surface to the ingot center. Thus, different Fe intermetallic phases such as  $\text{Al}_m\text{Fe}$ ,  $\text{Al}_6\text{Fe}$ ,  $\alpha\text{-AlFeSi}$  and  $\text{Al}_3\text{Fe}$  can form preferentially in different positions of the ingot. The Fe intermetallic phase transition in DC casting ingot may cause microstructure inhomogeneities, which in turn cause the so called fir-tree zones (FTZs) in the ingots as well as streaks and bands on the Al sheets.

Nowadays, with the increase of impurity in aluminium smelting raw materials (coke, alumina, etc.), the levels of trace elements present in the primary metal is gradually increasing. The impact of this increase on the aluminium transformation process and the final products is uncertain. Thus, there is a clear need to better understand these impacts, which will allow identifying ways to mitigate the negative impacts.

The study presented in this thesis was performed on AA5657 alloys to study the effect of trace elements V and Ni on Fe intermetallic phases formation and distribution. A slice of AA1050 alloy ingot with visible FTZs was also studied to characterize the Fe intermetallic phases transition across the FTZs. A DC simulator was built in the lab, which can reproduce the solidification conditions in the sub-surface regions of industry ingots.

The methods for the characterization of Fe intermetallic particles were developed in this research.  $\text{Al}_m\text{Fe}$ ,  $\text{Al}_6\text{Fe}$ ,  $\alpha\text{-AlFeSi}$  and  $\text{Al}_3\text{Fe}$  intermetallic phases were successfully identified by using Deep-etching method, EDS and EBSD technique in combination. Quantitative analysis of the Fe intermetallic particles was carried out by

using the image analysis technique.

The results show that AA5657 ingot contains four types of Fe intermetallic phases namely  $\text{Al}_m\text{Fe}$ ,  $\text{Al}_6\text{Fe}$ ,  $\text{Al}_3\text{Fe}$  and  $\text{Al}_7\text{Fe}_2\text{Si}$  ( $\alpha\text{-AlFeSi}$ ). Moreover, it was found that the local cooling rates have great effect on the type of phase formation,  $\text{Al}_m\text{Fe}$  and  $\alpha\text{-AlFeSi}$  are dominant phases in the zone near ingot surface where it has high cooling rates, while  $\text{Al}_3\text{Fe}$  becomes the major phase in the ingot center where the low cooling rate prevails.

It was observed in an industry AA1050 ingot that  $\text{Al}_m\text{Fe}$ ,  $\text{Al}_6\text{Fe}$ ,  $\text{Al}_3\text{Fe}$ ,  $\alpha\text{-AlFeSi}$  and a Ni containing intermetallic phases distribute across the FTZs, and the transition from  $\text{Al}_m\text{Fe}$  to  $\text{Al}_6\text{Fe}$  is the main factor that makes the FTZs visible.

It was found that the trace element V in AA5657 alloy heavily promotes  $\text{Al}_m\text{Fe}$  and suppresses  $\text{Al}_3\text{Fe}$ ,  $\text{Al}_6\text{Fe}$ ,  $\text{Al}_7\text{Fe}_2\text{Si}$  ( $\alpha\text{-AlFeSi}$ ). Ni promotes  $\text{Al}_3\text{Fe}$  and suppresses  $\text{Al}_m\text{Fe}$  and  $\text{Al}_6\text{Fe}$ . In the DC simulator cast AA5657 samples that with high levels of Ni addition (over 390 ppm), a Ni containing phase forms. The mechanism of the effect of V and Ni on Fe intermetallic phases was discussed based on the theory of the trace elements effects on competitive nucleation and competitive growth.

## Résumé

L'alliage AA5657 est l'un des plus importants alliages de la série 5xxx. Ces applications sont essentiellement tournées vers de nombreux domaines, comme l'électricité, l'emballage l'architecture, et l'impression. Par ailleurs, les différents domaines d'applications nécessitent une finition de surface de qualité supérieure, et une microstructure homogène des lingots d'alliages. Dans l'industrie de la coulée semi-continue verticale (Direct Chill) des lingots d'alliages d'aluminium des série 1xxx et 5xxx, il existe différents taux de refroidissement entre la surface de coulée et le centre des lingots. C'est ainsi que plusieurs phases intermétalliques de Fer, tel que,  $Al_mFe$ ,  $Al_6Fe$ ,  $\alpha-AlFeSi$  et  $Al_3Fe$  se forment préférentiellement dans différentes positions du lingot. La transition de la phase intermétallique de Fer dans le lingot issu de la coulée semi-continue verticale peut causer des inhomogénéités microstructurales, qui a leur tour provoqueraient ce qu'on appelle, la structure en sapin (FTZs) dans les lingots, ainsi que des stries et des bandes sur les feuilles d'aluminium.

De nos jours, avec l'augmentation des impuretés dans les matières premières (coke, alumine, etc.), la quantité des éléments de trace présent dans le métal primaire croît progressivement. Cependant, l'impact de cette croissance sur le processus de transformation de l'aluminium et sur le produit final n'est pas encore élucidé. En conséquence, il y a un besoin évident de comprendre cet effet, et permettre ainsi de proposer des solutions afin d'atténuer les effets négatifs de ces impuretés.

L'étude présentée dans ce mémoire a été réalisée sur l'alliage AA5657 dans le but d'examine l'effet des éléments de trace V et Ni sur la formation et la distribution des phases intermétalliques de Fer. Une tranche d'un lingot d'alliage AA1050 avec une structure en sapin visible a également été étudiée fin de caractériser la transition des phases intermétalliques à travers la structure en sapin. Un simulateur de coulée semi continue, capable de reproduire les conditions de solidification dan les régions des lingots a été construit dans le laboratoire du CURAL.

Les méthodes utilisées pour caractériser les particules intermétalliques de Fer ont



été développés dans ce travail de recherche. Les phases intermétalliques  $\text{Al}_m\text{Fe}$ ,  $\text{Al}_6\text{Fe}$ ,  $\alpha\text{-AlFeSi}$  et  $\text{Al}_3\text{Fe}$  ont été identifiées avec succès sur des échantillons ayant subi une attaque chimique et en utilisant ensuite une combinaison de deux techniques, spectroscopie de dispersion d'énergie et l'imagerie en diffraction d'électron rétrodiffusé. Une analyse quantitative des particules intermétalliques de Fer a été aussi réalisée en utilisant la technique d'analyse d'image.

Les résultats montrent la présence de quatre types de phases intermétalliques de Fer dans le lingot AA5657. Ces phases sont  $\text{Al}_m\text{Fe}$ ,  $\text{Al}_6\text{Fe}$ ,  $\text{Al}_3\text{Fe}$  et  $\text{Al}_7\text{Fe}_2\text{Si}$  ( $\alpha\text{-AlFeSi}$ ). Par ailleurs, il a été constaté que les taux de refroidissement locaux ont un effet considérable sur le type de phase formée. De plus, les phases  $\text{Al}_m\text{Fe}$  et  $\text{Al}_7\text{Fe}_2\text{Si}$  paraissent dominantes dans la zone près de la surface du lingot où le taux de refroidissement est élevé, pendant que la phase  $\text{Al}_3\text{Fe}$  devient majoritaire dans le centre du lingot où le taux de refroidissement est bas.

Il a été observé dans l'alliage AA1050 que  $\text{Al}_m\text{Fe}$ ,  $\text{Al}_6\text{Fe}$ ,  $\text{Al}_3\text{Fe}$ ,  $\text{Al}_7\text{Fe}_2\text{Si}$  et les phases intermétalliques contenant l'élément Ni sont distribuées le long des structures en sapin, et la transition de la phase  $\text{Al}_m\text{Fe}$  vers la phase  $\text{Al}_6\text{Fe}$  est le facteur principal qui rend les structures en sapin visibles.

Il a été constaté que l'élément de trace V favorise fortement la formation de la phase  $\text{Al}_m\text{Fe}$  et la suppression des phases  $\text{Al}_6\text{Fe}$ ,  $\text{Al}_3\text{Fe}$ ,  $\text{Al}_7\text{Fe}_2\text{Si}$  dans l'alliage AA5657. L'élément Ni favorise la formation de la phase  $\text{Al}_3\text{Fe}$  et supprime les phases  $\text{Al}_m\text{Fe}$  et  $\text{Al}_6\text{Fe}$ . Dans les échantillons d'alliage AA5657 issus de la coulée semi-continue avec une teneur élevée en Ni (plus de 390 ppm), la formation de la phase contenant l'élément Ni est plus favorable. Le mécanisme expliquant l'effet des éléments V et Ni sur les phases intermétalliques de Fer a été discuté en se basant sur la théorie de l'effet des éléments de trace sur la compétitivité dans la germination et la croissance des phases.

*(Merci à doctorat Mehand pour la traduction de l'anglais vers le français)*

## **ACKNOWLEDGMENTS**

It is a great pleasure to have the chance to convey my thanks to all those who were involved, directly or indirectly, in making this project a success. I would like to express my sincere thanks to my supervisors, Professors X.-Grant Chen and Zhan Zhang, for giving me the opportunity to undertake this research. I would like to convey my appreciation to all members of the CIMTAL group for their assistance during my over two years of research, particularly to M. Bouchard and E. Brideau, technicians of the Chair for their help with the DC simulator casting and sample preparation. Thanks to Kun Liu and Cangji Shi, who are my friends for their help with the sample analysis.

Finally, I would like to express my profound gratitude to the members of my family, especially my wife Yumei Han, who recommended me to UQAC, without her help, I would not have been able to fulfill my goal of completing a Master's Degree successfully.

This work was carried out with financial support of Natural Sciences and Engineering Research Council of Canada NSERC and Rio Tinto Alcan, through the NSERC/Rio Tinto Alcan Industrial Research Chair in Metallurgy of Aluminium Transformation, Professor X.-Grant Chen. In addition, this work was awarded the prize of CQRDA and MACE3 on REGAL Students' Day poster contest for two consecutive years in 2010 and 2011.

# TABLE OF CONTENTS

<b>ABSTRACT .....</b>	<b>I</b>
<b>RÉSUMÉ .....</b>	<b>错误！未定义书签。</b>
<b>ACKNOWLEDGMENTS.....</b>	<b>V</b>
<b>TABLE OF CONTENTS .....</b>	<b>VI</b>
<b>LIST OF FIGURES .....</b>	<b>VIII</b>
<b>LIST OF TABLES.....</b>	<b>XII</b>
<b>CHAPTER 1 DEFINITION OF THE PROBLEM.....</b>	<b>1</b>
1.1 INTRODUCTION.....	1
1.1.1 DC casting AA5657 alloy .....	2
1.2 OBJECTIVE AND METHODOLOGY OF PRESENT WORK .....	6
<b>CHAPTER 2 REVIEW OF THE LITERATURE.....</b>	<b>8</b>
2.1 FINDINGS FOUND IN PREVIOUS RESEARCHES .....	8
2.2 FTZs AND Fe INTERMETALLIC PHASES IN DC CAST Al ALLOYS.....	9
2.2.1 Iron intermetallic phases in the Al-Fe-Si system .....	13
2.2.1.1 Al <sub>3</sub> Fe phase.....	16
2.2.1.2 Al <sub>6</sub> Fe phase.....	17
2.2.1.3 Al <sub>m</sub> Fe phase.....	18
2.2.1.4 Al <sub>x</sub> Fe phase.....	19
2.2.1.5 α-AlFeSi.....	20
2.2.1.6 β- AlFeSi .....	21
2.2.2 Factors that affect Fe phases selection in Al alloys.....	22
2.2.2.1 Cooling rates.....	23
2.2.2.2 Fe/Si ratio.....	25
2.2.2.3 Grain refinement .....	25
2.2.2.4 Trace elements effects .....	26
2.3 DC CASTING SIMULATOR TECHNIQUES .....	28
2.4 EBSD TECHNIQUE .....	29
<b>CHAPTER 3 EXPERIMENTAL PROCEDURES .....</b>	<b>31</b>
3.1 ALLOY PREPARATION .....	31
3.2 MELTING AND CASTING .....	31
3.3 SAMPLE ANALYSIS AND CHARACTERIZATION .....	34
3.3.1 Chemical analysis .....	34
3. 3.2 Optical Microscopy .....	35
3.3.3 Deep-etching of metallographic sample .....	36
3. 3.4 Electron Backscatter Diffraction (EBSD).....	37
3. 3.4.1 Fe intermetallic phases database creation.....	38
3. 3.4.2 EBSD sample preparation .....	38

3. 3.4.3 Fe intermetallic Phases quantitafiction.....	39
<b>CHAPTER 4 RESULTS AND DISCUSSION .....</b>	<b>41</b>
4.1 PHASE CHACTERIZATION IN AN AA5657 DC CAST INGOT .....	41
4.1.1 Ingot microstructure .....	41
4.1.2 Fe intermetallic phases morphology and EDS results .....	42
4.1.3 Phase identification using EBSD technique .....	45
4.1.4 Phase quantitafiction.....	47
4.2 PHASE CHARACTERIZATION IN AN AA1050 DC CAST INGOT ACROSS THE FTZs .....	50
4.2.1 Ingot microstructure .....	51
4.2.2 EDS and Deep-etching morphology .....	52
4.2.3 Fe Phase characterization using EBSD technique .....	56
4.2.4 Phase quantitafiction.....	57
4.3 DC SIMULATOR AND FE INTERMETALLIC PHASES IN DC SIMULATOR CAST AA5657 INGOTS .....	59
4.3.1 DC simulator.....	59
4.3.2 Fe intermetallic phases in the base material of DC simulator cast AA5657 ingots (A01 alloy in Table 3.2) .....	62
4.3.2.1 Ingot microstructure .....	62
4.3.2.2 EBSD diffraction patterns .....	65
4.3.2.3 Image analysis results .....	66
4.4 EFFECT OF NI ON FE INTERMETALLIC PHASES IN DC SIMULATOR CAST AA5657 INGOTS .....	70
4.4.1 Ingots Microstructure .....	70
4.4.2 EBSD patterns.....	75
4.4.3 Image analysis results.....	77
4.5 EFFECT OF V ON FE INTERMETALLIC PHASES IN DC SIMULATOR CAST AA5657 INGOTS.....	82
4.4.1 Ingots structure .....	83
4.5.2 EBSD patterns.....	85
4.5.3 Image analysis results.....	86
4.6 EFFECT OF THE COMBINED ADDITION OF V AND NI ON FE INTERMETALLIC PHASES IN DC SIMULATOR CAST AA5657 INGOTS .....	94
4.6.1 Ingots Microstructure .....	94
4.2.2 EBSD patterns.....	96
4.6.3 Image analysis results.....	98
<b>CHAPTER 5 CONCLUSIONS AND SUGGESTIONS FOR FURTHER WORK .....</b>	<b>101</b>
5.1 CONCLUSIONS .....	101
5.2 SUGGESTIONS FOR FURTHER WORK.....	102
<b>APPENDICES.....</b>	<b>103</b>
<b>REFERENCES.....</b>	<b>108</b>

# LIST OF FIGURES

## Chapter 1

FIGURE 1.1: SCHEMATIC ILLUSTRATION OF A VERTICAL DC CASTER AND HEAT EXTRACTION MODE. ....	3
FIGURE 1.2: LONGITUDINAL SECTION OF 2 INGOTS SHOWING THE FIR-TREE ZONES OF DIFFERENT SIZES IN 1XXX SERIES AL ALLOY. ....	5
FIGURE 1.3: SCHEMATIC OF DIFFERENT ZONES FORMING IN DC-CAST ROLLING INGOTS AND THE ZEBRA STRUCTURE (BANDS AND STEAKS) FORMING IN SCALPED AND ROLLED INGOT <sup>10</sup> . ....	6

## Chapter 2

FIGURE 2.1: SCHEMATIC ILLUSTRATION OF VARIOUS ZONES ACROSS THE INGOT THICKNESS.....	10
FIGURE 2.2: THE AL RICH CORNER OF THE EQUILIBRIUM AL-Fe PHASES DIAGRAM. ....	13
FIGURE 2.3: LIQUIDUS PROJECTION NEAR THE AL-CORNER IN THE AL-Fe-Si PHASE DIAGRAM. ....	13
FIGURE 2.4: COMPOSITION OF THE INTERMETALLIC PARTICLES OBSERVED IN DC-CAST ALLOYS <sup>27</sup> .....	16
FIGURE 2.5: (A) $Fe_4Al_{13}$ AT GRAIN BOUNDARIES IN CAST INGOT ; (B) TYPICAL [110] DIFFRACTION PATTERN OF A FAULTED $Fe_4Al_{13}$ CRYSTAL .....	17
FIGURE 2.6: (A) $Al_6Fe$ PHASES IN A TEM SAMPLE; (B) SAD PATTERN IN THE (110) ZONES. ....	18
FIGURE 2.7: $Al_MFe$ AND CORRESPONDING [110] DIFFRACTION PATTERN <sup>32</sup> .....	19
FIGURE 2.8: (A) $Al_xFe$ AND ITS DIFFRACTION PATTERN <sup>34</sup> .....	20
FIGURE 2.9: (A) EXTRACTED $A_c-AlFeSi$ ( $Al_8Fe_2Si$ ) (B) SAD PATTERN IN THE $\langle 111 \rangle$ ZONE <sup>34</sup> .....	21
FIGURE 2.10: B- $AlFeSi$ INTERMETALLIC PHASE. (A) SEM MICROGRAPH OF DEEP-ETCHED SAMPLE; (B) TEM IMAGE WITH SAD PATTERN. ....	22
FIGURE 2.11: COOLING RATE AND CORRESPONDING SECONDARY DENDRITE ARM SPACING AS A FUNCTION OF DISTANCE FROM INGOT SURFACE, CRITICAL COOLING RATE FOR $AlMFe$ IS GIVEN <sup>33</sup> .....	24

## Chapter 3

FIGURE 3.1: SCHEMATIC ILLUSTRATION OF DC SIMULATOR APPARATUS.....	32
FIGURE 3.2: DC CASTING SIMULATOR USED IN PRESENT RESEARCH. ....	32
FIGURE 3.3: THE ELECTRIC FURNACE USED IN THE LAB. ....	33
FIGURE 3.4: COOLING CURVE TEST APPARATUS USED IN THE LAB. ....	34
FIGURE 3.5: CLEMEX IMAGE ANALYSIS SYSTEM WITH NIKON ECLIPSE ME 600 OPTICAL MICROSCOPE. ....	36
FIGURE 3.6: JEOM JSM-6480LV SEM SYSTEM .....	37
FIGURE 3.7: FORMATION OF KIKUCHI BANDS BY BACK-SCATTERED ELECTRONS.....	30
FIGURE 3.8: SCHEMATIC ILLUSTRATES THE 6 FIELDS CHOSEN IN A SAMPLE.....	39

## Chapter 4

FIGURE 4.1: MICROSTRUCTURE OF AA5657 CAST INGOT AT THE POSITION AWAY FROM CASTING SURFACE AT 10 MM (A), 40 MM (B), 90 MM (C), 140 MM (D) AND 300 MM (E).....	41
FIGURE 4.2: TYPICAL FE PHASES MORPHOLOGIES IN THE AA5657 CAST INGOT.....	42
FIGURE 4.3: FE INTERMETALLIC PHASES MORPHOLOGY UNDER SEM.....	43
FIGURE 4.4: FE INTERMETALLIC PHASES MORPHOLOGY (DEEP-ETCHING) UNDER SEM..	43
FIGURE 4.5: TYPICAL EDS RESULTS OF FE INTERMETALLIC PHASES. ....	44
FIGURE 4.6: FOUR TYPES OF EBSD PATTERNS AND CORRESPONDING SOLUTIONS.....	46
FIGURE 4.8: FE INTERMETALLIC PHASES DISTRIBUTION AA5657 CAST INGOT. ....	47
FIGURE 4.7 SCHEMATIC SHOWS THE SAMPLING POSITION IN AN AA5657 DC CAST INGOT. ....	47
FIGURE 4.9: FTZ REVEALED IN AA1050 ALLOY INGOT.....	51
FIGURE 4.10: MICROSTRUCTURE OF AA1050 INGOT ACROSS THE FTZs. ....	52
FIGURE 4.11: EDS RESULTS OF FE INTERMETALLIC PHASES IN AA1050 INGOT. ....	53
FIGURE 4.12: MORPHOLOGIES OF FE INTERMETALLIC PHASES (DEEP-ETCHED)..	53
FIGURE 4.13: MORPHOLOGY OF NI CONTAINING INTERMETALLIC PHASE UNDER SEM IN SEI MODE. A) BEFORE DEEP-ETCHING, B) AFTER DEEP-ETCHING. ....	54
FIGURE 4.14: EDS RESULTS OF A NI CONTAINING PARTICLE. ....	55
FIGURE 4.15: EBSD DIFFRACTION PATTERNS AND CORRESPONDING SOLUTIONS OF DIFFERENT TYPE OF FE INTERMETALLIC PHASES IN AA1050 ALLOY INGOT.....	57
FIGURE 4.16: FE INTERMETALLIC PHASE DISTRIBUTION ACROSS THE FTZs IN AA1050 ALLOY INGOT. .	57
FIGURE 4.17: DC SIMULATOR CASTING INGOTS IN THE LAB. ....	59
FIGURE 4.18: COOLING CURVES GOT FROM DC SIMULATOR CASTING AA5657 ALLOY. ....	60
FIGURE 4.19: THE AVERAGE COOLING RATES IN DIFFERENT POSITION OF THE INGOT FROM 700°C TO 650°C .....	60
FIGURE 4.20: COOLING CURVE AND FIRST DERIVATION OBTAINED FROM THE AA5657 ALLOY COOLED AT 1.28 °C/s.....	61
FIGURE 4.21: MICROSTRUCTURE OF DC SIMULATOR CASTING AA5657 ALLOY TAKEN FROM (A) 20 MM, (B) 40 MM, (C) 60 MM, (D) 100 MM FROM THE CHILL END. ....	62
FIGURE 4.22: FE INTERMETALLIC PHASES MORPHOLOGY UNDER SEM.....	63
FIGURE 4.23: FE INTERMETALLIC PHASES MORPHOLOGY UNDER SEM (DEEP-ETCHING).....	64
FIGURE 4.24: TYPICAL EDS RESULTS OF FE INTERMETALLIC PHASES IN A01.....	64
FIGURE 4.25:EBSD DIFFRACTION PATTERNS AND CORRESPONDING SOLUTIONS OF DIFFERENT TYPE OF FE INTERMETALLIC PHASES IN A01 ALLOY INGOT. ....	66
FIGURE 4.26: FE INTERMETALLIC PHASE DISTRIBUTION IN INGOT A01.....	67
FIGURE 4.27: DISTRIBUTION OF TOTAL PHASE VOLUME FRACTION IN THE INGOT A01.....	68
FIGURE 4.28: PARTICLE DENSITY OF EACH PHASE IN A01 INGOT.....	68
FIGURE 4.29: SURFACE AREA OF EACH PHASE IN A01 INGOT.....	69
FIGURE 4.30: EDS SHOWS THE HIGH CONTENT OF NI IN THE GRAIN BOUNDARY AFTER THE ADDITION OF	

Ni. ....	70
FIGURE 4.31: PHOTO MICROSTRUCTURE TAKEN FROM DIFFERENT Ni CONTAINING INGOTS WITH A DISTANCE OF 40 MM FROM THE CHILL ENDS. ....	71
FIGURE 4.32: FE INTERMETALLIC PHASES MORPHOLOGY UNDER SEM IN A08 ALLOY.....	72
FIGURE 4.33: EDS SPECTRA OF FE INTERMETALLIC PARTICLES IN A08 ALLOY.. ....	72
FIGURE 4.34: TYPICAL MORPHOLOGY OF AlFeNi IN A DC SIMULATOR CASTING INGOT UNDER SEM. (A) BEFORE DEEP-ETCHING, (B) AFTER DEEP-ETCHING. ....	73
FIGURE 4.35: EDS SPECTRA OF AlFeNi IN A DC SIMULATOR CASTING A08 INGOT. ....	73
FIGURE 4.36: AN AlFeNi PARTICLE UNDER THE SEM BEC MODE, A WHITE SPOT IS CLEARLY OBSERVED. .....	74
FIGURE 4.37: EDS SHOWS HIGH Ni CONTENT IN THE WHITE SPOT OF A AlFeNi PARTICLE. ....	74
FIGURE 4.38: DISTRIBUTION OF AlFeNi PARTICLE DENSITY IN A07, A08 ALLOY INGOTS.....	75
FIGURE 4.39:EBSD DIFFRACTION PATTERNS AND CORRESPONDING SOLUTIONS OF DIFFERENT TYPE OF FE INTERMETALLIC PHASES IN A08 ALLOY. ....	76
FIGURE 4.40: THE DISTRIBUTION OF FE INTERMETALLIC PHASES IN AA5657 ALLOY INGOTS WITH DIFFERENT Ni CONTENT. ....	78
FIGURE 4.41: TOTAL FE PHASES VOLUME FRACTION IN THE Ni CONTAINING INGOTS.....	79
FIGURE 4.42:EFFECT OF Ni ON Al <sub>3</sub> Fe PARTICLE DENSITY.....	81
FIGURE 4.43: INCREASE IN THE VANADIUM CONTENT OF COKE OVER TIME.....	82
FIGURE 4.44: PHOTOMICROGRAPH TAKEN FROM DIFFERENT V CONTAINING DC CAST INGOTS WITH A DISTANCE OF 40 MM FROM THE CHILL ENDS.....	83
FIGURE 4.45: FE INTERMETALLIC PHASES MORPHOLOGY UNDER SEM IN A04 ALLOY.....	84
FIGURE 4.46: EDS SPECTRA OF FE INTERMETALLIC PARTICLES IN A04 ALLOY.. ....	84
FIGURE 4.47: EBSD DIFFRACTION PATTERNS AND CORRESPONDING SOLUTIONS OF DIFFERENT TYPE OF FE INTERMETALLIC PHASES IN A04 ALLOY. ....	86
FIGURE 4.48: THE DISTRIBUTION OF FE INTERMETALLIC PHASES IN AA5657 ALLOY INGOTS WITH DIFFERENT LEVELS OF V CONTENT. ....	87
FIGURE 4.49: TOTAL FE PHASES VOLUME FRACTION IN THE V CONTAINING INGOTS.....	88
FIGURE 4.50: ENTRAINED DROPLET MELTING DIFFERENTIAL SCANNING CALORIMETER TRACES FROM Ixxx SERIES ALUMINIUM ALLOYS WITH A HIGH PURITY BASE, A LOW PURITY BASE, HIGH PURITY BASE PLUS HIGH AND LOW LEVELS OF VANADIUM, AND HIGH PURITY BASE WITH A COMBINATION OF LOW VANADIUM AND GRAIN REFINER ADDITION. ....	90
FIGURE 4.51: SCHEMATIC ILLUSTRATION OF THE FORMATION OF V CONTAINING PARTICLES ACT AS PREFERENTIAL NUCLEATION SITES OF Al <sub>M</sub> Fe, RAISING THE NUCLEATION TEMPERATURE AND LOWER THE CRITICAL COOLING RATE T <sub>C</sub> FOR Al <sub>M</sub> Fe FORMATION.....	91
FIGURE 4.52: SCHEMATIC ILLUSTRATION OF THE V ADDITION DECREASE THE GROWTH TEMPERATURE OF Al <sub>3</sub> Fe, LOWER THE CRITICAL GROWTH VELOCITY FOR Al <sub>M</sub> Fe.....	93
FIGURE 4.53: MICROSTRUCTURE TAKEN FROM DIFFERENT V AND Ni CONTAINING INGOTS WITH A DISTANCE OF 40 MM FROM THE CHILL ENDS.. ....	94
FIGURE 4.54: FE INTERMETALLIC PHASES MORPHOLOGY UNDER SEM IN A10 ALLOY.....	95

FIGURE 4.55: EDS SPECTRA OF Fe INTERMETALLIC PHASES IN A10 ALLOY .....	96
FIGURE 4.56: EBSD DIFFRACTION PATTERNS AND CORRESPONDING SOLUTIONS OF DIFFERENT TYPE OF Fe INTERMETALLIC PHASES IN V CONTAINING INGOTS .....	97
FIGURE 4.57: THE DISTRIBUTION OF Fe INTERMETALLIC PHASES IN AA5657 ALLOY INGOTS WITH DIFFERENT LEVELS OF V AND Ni CONTENT.. .....	99
FIGURE 4.58: EFFECT OF V AND Ni ON TOTAL Fe INTERMETALLIC PHASES VOLUME FRACTION. ....	100



# LIST OF TABLES

## Chapter 1

TABLE 1.1 CHEMICAL COMPOSITION OF 1XXX AND 5XXX AL ALLOYS.....	1
TABLE 1.2 LOCAL HEAT TRANSFER COEFFICIENTS AND COOLING RATES IN DC-CASTING <sup>7</sup> .....	4

## Chapter 2

TABLE 2.1 FE-CONTAINING PHASES IDENTIFIED IN DIFFERENT REGIONS IN A 1XXX-SERIES AL INGOT <sup>8</sup> ...	11
TABLE 2.2: SOLIDIFICATION REACTIONS IN THE AL-FE-SI SYSTEM <sup>5,9</sup> .....	14
TABLE 2.3: CRITICAL COOLING RATES FOR THE FORMATION OF SOME FE INTERMETALLIC PHASES.....	24
TABLE 2.4: EFFECT OF FE/SI RATIO ON FTZs WIDTH IN AL-FE-SI ALLOY INGOTS <sup>11</sup> .....	25
TABLE 2.5: EFFECT OF TRACE ELEMENTS ON THE FORMATION OF FE INTERMETALLIC PHASES <sup>12, 13</sup> .....	27

## Chapter 3

TABLE 3.1: CHEMICAL COMPOSITION OF THE INDUSTRIAL DC CAST AA5657 INGOT .....	31
TABLE 3.2: CHEMICAL COMPOSITIONS OF THE DC SIMULATOR CAST ALLOYS (WT. %).....	35
TABLE 3.3: FOUR STEPS PROCEDURES FOR THE EBSD SAMPLE PREPARATION.....	38

## Chapter 4

TABLE 4.1 CHEMICAL COMPOSITION OF AN AA1050 DC CAST INGOT (WT.%). .....	50
TABLE 4.2: CHEMICAL COMPOSITION OF NI CONTAINING PARTICLES IN 1XXX-SERIES ALLOY INGOT, ATOMS% .....	55

# CHAPTER 1 DEFINITION OF THE PROBLEM

## 1.1 INTRODUCTION

Nowadays, approximate 40% of Aluminium products are flat rolled products, in which about 90% are produced by the direct chill (DC) casting. The 1xxx and 5xxx-series aluminium alloys are two major non-heat-treatable (NHT) alloy groups used in 50% of all the flat rolled Al products<sup>1</sup>. When these products are used in the fabrication of products that demand high quality surface finishing such as lithographic sheets and plates, architectural panels, wine cans and so on, the Al sheets require high quality surface and the DC cast ingots require microstructure homogeneous<sup>1, 2</sup>.

In the industry DC (direct-chill) casting of 1xxx and 5xxx-series aluminium ingots (Table 1.1), there often exist a macro defect in the ingots called Fir-tree Zones (FTZs), which can cause serious surface defect on the rolling sheets.

Table 1.1 Chemical composition of 1xxx and 5xxx Al alloys<sup>1</sup>

Alloy	Element (wt %)							
	Fe max	Si max	Cu max	Mn max	Mg	Cr max	Zn max	Al min
AA1050	0.4	0.25	0.05	0.05	< 0.05	-	0.05	99.50
AA1100	*	*	0.2	0.05	-	-	0.1	99.00
AA5005	0.7	0.3	0.2	0.2	0.5-1.1	0.1	0.25	rem

\* 0.95 (Si+Fe)

In the past decades, although a lot of effort has been put in the aluminium

industry to eliminate the FTZ defect, success is only limited.

### **1.1.1 DC casting AA5657 alloy**

According to the wrought aluminium alloys designation system, the alloy of series that containing magnesium as the major alloy element are designate as 5xxx. As it is known, the addition of magnesium can markedly increase the strength of aluminum without decreasing the ductility, the corrosion resistance and weld ability are also good<sup>3</sup>. AA5657 alloy is one of the important members of 5xxx series. This alloy has application in many fields, such as packing, electricity, architectural, printing, and so on. Such application of AA5657 alloy requires high surface qualities Al sheets<sup>8</sup>.

In AA5657 alloy ingots, the elements Si and Fe are the most common impurities appear. When compared Si with Fe, Si has higher solubility in molten aluminum and during solidification, which can reach 1.6%. Lower levels of Si are therefore easily dissolved at all molten stages of production and would be rejected into the liquid between dendrite arms during solidification process<sup>4</sup>. But the solubility of iron in the solid state is very low (~0.05 wt %) and therefore, most of the iron present in aluminum over this amount appears as an intermetallic second phase in combination with aluminum and often other elements<sup>5,6</sup>.

A sketch of the DC semi-continuous casting process is shown in Figure 1.1. At beginning, the starting block is positioned inside the mold and the liquid metal is poured into the open mold from the top. A solidified shell is formed above the starting

block and along the mold wall (primary cooling). As soon as the solidified shell (about 10 mm in thickness) is strong enough to hold the molten metal inside, the starting block is lowered. As the ingot emerges from the bottom of the mold, the cooling water impinges directly on the casting surface (Secondary cooling). The maximum heat extraction and main part of the solidification of the ingot occurs due to the secondary cooling, and this is why it is called DC casting. After some distance, e.g., 1 m for a commercial-size sheet ingot, a nearly steady-state regime (the stationary period) is established for the thermal field.

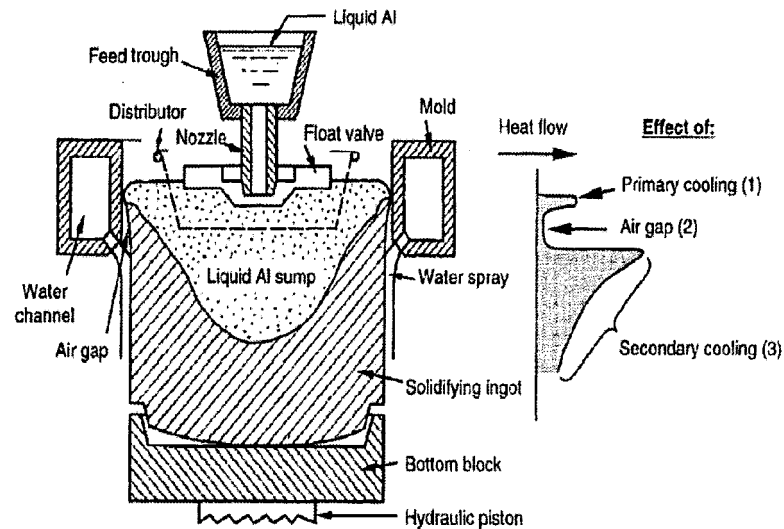


Figure 1.1: schematic illustration of a vertical DC caster and heat extraction mode<sup>7</sup>.

During DC-casting of aluminium alloy ingots, the Al liquid is first cooled and solidified by the heat conduction between the walls of water-cooled mold, due to a high heat transfer coefficient<sup>7</sup>. It forms the shell, which takes the shape of the mold and acquires sufficient strength to hold Al liquid sump in the center.

In the air gap region, the heat extraction caused by the ingot surface radiation is reduced due to lower heat transfer coefficient of air, which leads to shell reheating, or

even re-melting of the shell from inside.

The out skin formed during rapid primary cooling and the inner layer formed in the air gap region together is often called shell zone<sup>8</sup>. Following the shell zone is a zone subjected to secondary cooling due to the directly impingement of water spray<sup>9</sup>. The cooling rate becomes very high, because of the very high heat transfer coefficients. Thus, most of the heat extracted during this process by convection<sup>7</sup>. The cooling rates decreases gradually towards the ingot center due to longer diffusion paths.

Table 1.2 Local heat transfer coefficients and cooling rates in DC-casting<sup>7</sup>

Region	Cooling Stage	$h(\text{W/m}^2\text{K})$	Cooling rate
Water cooled Al mold	Primary cooling	2,000-5,500	High
Air-gap	Shell reheating	200-500	Low
Direct chill(water spray)	Secondary cooling	8,000-70,000	High

During the solidification process of DC casting Al ingots, the first phase solidified is the primary  $\alpha\text{-Al}$ , while Fe is eject into the remaining interdendritic Al liquid due to the low solubility, when Fe reaches the eutectic composition at 1.8wt% and 655°C, an equilibrium intermetallic phase  $\text{Al}_3\text{Fe}$  forms under equilibrium cooling rates between the dendrite arms of  $\alpha\text{-Al}$  matrix<sup>5</sup>. Under higher cooling rates, several nonequilibrium phases form, such as  $\text{Al}_m\text{Fe}$ ,  $\text{Al}_6\text{Fe}$ ,  $\alpha\text{-AlFeSi}$  and so on. In a DC casting Al ingot from the casting surface to the ingot center, the cooling rates varies from 20°C to  $\leq 0.5^\circ\text{C}^5$ . Because of the existence of the cooling rates difference in varies location of the DC casting ingot, different eutectic Fe intermetallic phases form

preferentially in different position of the ingot, and causes microstructure inhomogeneities, which can be easily observed by naked eyes after etching and/or anodizing. The FTZs caused in DC casting process can be highlight by the chemical etching and anodizing treatment, and can cause streaks and bands on the final rolling products. For the alloy ingots as AA5657 that are sold especial for their ability to develop and exhibit a pleasing surface, often undergo processes as etching and anodizing treatment, should be free from the defect of FTZs.

Nowadays, DC casting ingots with big size like 600mm X 2000mm in cross-section and more than 7000mm in length are commonly produced in Al industry. Such a shape makes the FTZs easier to appear. In industry practice, in order to eliminate the effect of FTZs, scalp the out skin of a ingot is carried out, the scalping depth normally is between 10mm and 20mm, but sometimes this depth is not enough to totally remove the FTZs, the remaining zones can be elongated into light and dark longitudinal streaks and bands in the rolling process, which greatly decrease the quality of the products<sup>10, 11</sup>. The appearance of the zones and the streaks is shown in Figure 1.2 and Figure 1.3.

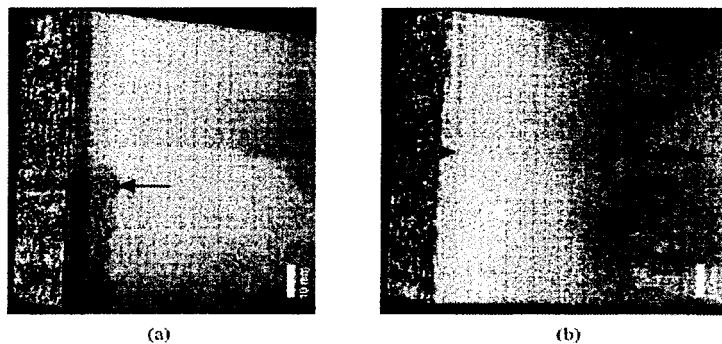


Figure 1.2: Longitudinal section of 2 ingots showing the fir-tree zones of different sizes in 1xxx series Al alloy. (a) Small FTZ, Fe/Si=3.4; (b) Large FTZ, Fe/Si=1. The FTZ locations are shown between 2 arrows. Alloy was etched in 10% NaOH at 70°C for 20mins<sup>11</sup>.

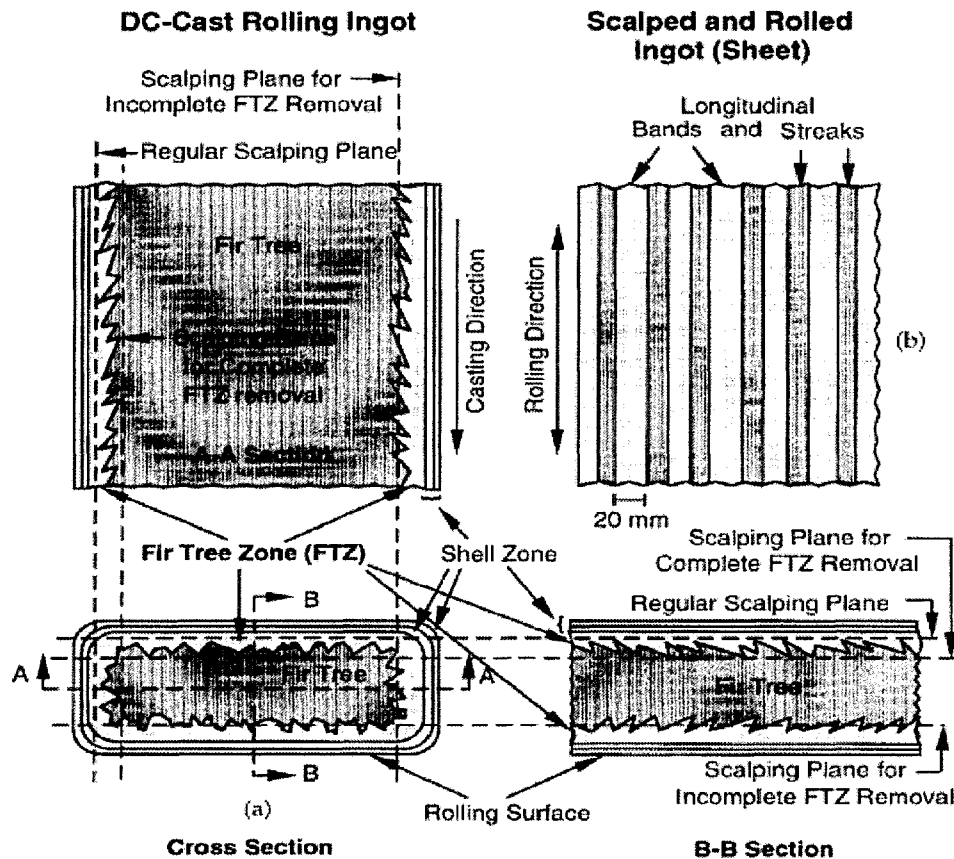


Figure 1.3: Schematic of different zones forming in DC-cast rolling ingots and the zebra structure (bands and steaks) forming in scalped and rolled ingot<sup>10</sup>.

## 1.2 Objective and methodology of present work

For the past several decades, a lot of research has been carried out to study the effect of DC casting ingot structure. Until now, it is widely accepted that the solidification process and resultant cast microstructure plays an important role in the product quality. It is quite clear that the formation of Fir-tree zone is a function of the cooling rates, Fe/Si ratio, grain refiner, and small quantities of trace elements<sup>12,13,14</sup>. But it is still not clear about the effect of trace elements V and Ni on Fe intermetallic phases and Fir-tree zones. Moreover, nowadays, with decreasing quality of aluminium

smelting raw material supply (coke, alumina ...) and alloying elements, the levels of trace elements present in the primary metal will increase<sup>15</sup>. The impact of this increase on the aluminium transformation processes and the final products is uncertain. Thus, there is a need to better understand these impacts, which will allow identifying ways to mitigate the negative impacts, to use the positive impacts for product/process improvement.

The methods used in this research are as follows:

1. DC casting simulator: A DC casting simulator apparatus is used in the laboratory to cast Al alloy ingots, which provides similar solidification conditions in the sub-surface regions as industry DC ingots.

2. Metallographic Studies: The ingot microstructure and Fe intermetallic phase morphologies were studied using Optical microscope, deep-etching and SEM techniques. SEM-EDS technique was also used to give an analysis of the elements containing in the Fe intermetallic phases.

3. Electron Backscattered Diffraction (EBSD): HKL Nordlys EBSD detector and Channel 5 system software are used for identification of intermetallic particles.

4. CLEMEX Image Analyzer: By using this technique, a quantitative analysis of the Fe intermetallic particles was performed.



## CHAPTER 2 REVIEW OF THE LITERATURE

Until now, most of the researches on Fir-tree Zones and Fe intermetallic phases were carried out in 1xxx-series. It is widely accepted that the formation of FTZs is caused by the Fe intermetallic phases formation in the Al ingots. In this chapter, a summary of previous finding is given firstly, after that a detailed review of existing literatures is presented.

### 2.1 Findings found in previous researches

It is well-known that the elimination of fir-tree zones in aluminium ingots can automatically eliminate the streaks and bands on aluminium sheets. Hence, in order to eliminate the fir tree-zones, a lot of studies were carried out by investigating the effect of DC cast process parameters, Si and Fe/Si ratio, the use of grain refiners and existence of trace elements. The following are the findings<sup>11, 12, 13, 14, 16</sup>.

1) High cooling rates (e.g.  $dT/dt > 10\text{ }^{\circ}\text{C/s}$ ) during secondary cooling in DC-casting promote  $\text{Al}_m\text{Fe}$  and FTZ formation.

2) High casting speeds promote  $\text{Al}_m\text{Fe}$  and FTZs formation.

3) Si promotes  $\text{Al}_m\text{Fe}$  and FTZs formation and Fe/Si has an effect on the thickness of FTZs. The largest FTZs width occurs at a Fe/Si ratio of about 2, it was reported that higher Fe/Si ratio caused smaller FTZs.

4) Grain refiner addition and a higher B/Ti ratio promote  $\text{Al}_m\text{Fe}$  and FTZ formation.

5) Some trace elements were reported to have effects on the fir-tree zone, but this

is still controversial and uncertain.

## **2.2 FTZs and Fe intermetallic phases in DC cast Al alloys**

As mentioned in chapter 1, in industrial DC casting of Aluminium, a wide range of solidification conditions exists. Thus, there form a number of Fe intermetallic phases in the ingot and cause the formation of FTZs. In DC casting of AA1xxx and AA5xxx sheet alloys, elements Fe and some Si usually present in the ingots. Depending on the chemistry composition and solidification conditions, the presence of elements Fe and Si can form a number of binary Al-Fe and ternary Al-Fe-Si intermetallic phases while casting 1xxx alloys<sup>4</sup>. When the solidification is in equilibrium conditions ( $dT/dt < 0.015^{\circ}\text{C/s}$ ), the part of iron that excess its solubility limit will form a eutectic  $\alpha\text{-AlFeSi}$  and an intermetallic phase  $\text{Al}_3\text{Fe}$  (often designated as  $\text{Al}_{13}\text{Fe}_4$ ). But in the industry practice of Direct-Chill casting aluminium alloys, the ingot surface usually has higher cooling rate due to its direct contact with the mould of cooling water, so we should consider the difference between cooling rates variation in the casting ingot ( $dT/dt$ ). Celil A. Aliravci<sup>5</sup> found at cooling rates decreasing from  $\sim 20^{\circ}\text{C}$  near the surface to  $\leq 1^{\circ}\text{C}$  in the ingot center can cause the formation of metastable intermetallic phases besides the stable phase  $\text{Al}_3\text{Fe}$ , such as  $\text{Al}_6\text{Fe}$ ,  $\text{Al}_m\text{Fe}$  and so on. These phases form preferentially under varies cooling rates in different location of DC cast ingots.

On sectioning and surface treatment of an ingot, the areas of different phase

content have different responses to a given etchant, the surface appears alternate dark and light etching zones, which is often referred to as “fir-tree” zones. The fir-tree zones are mainly caused by the Fe intermetallic phases transition microscopically, it is a macro-defect in the sub-surface regions in DC cast ingots. In the past, the fir-tree zone was often described as transitional process from metastable phase  $\text{Al}_6\text{Fe}$  to stable phase  $\text{Al}_3\text{Fe}$ . But more recently, people have found that the fir-tree zones is a phenomena which involves transitions of different intermetallic phases at the same time, such as  $\alpha\text{-AlFeSi}$  to  $\text{Al}_3\text{Fe}$ ,  $\alpha\text{-AlFeSi}$  to  $\text{Al}_6\text{Fe}$ ,  $\text{Al}_m\text{Fe}$  to  $\text{Al}_6\text{Fe}$ . Thus, in DC casting Al ingots, a mixture of iron intermetallic phases can be observed on both sides of the fir-tree zones and the phases vary across the zones.

H. Wenstengen observed five distinct regions across the thickness of a DC casting Al ingot using caustic soda etching method<sup>8</sup> (Figure 2.1).

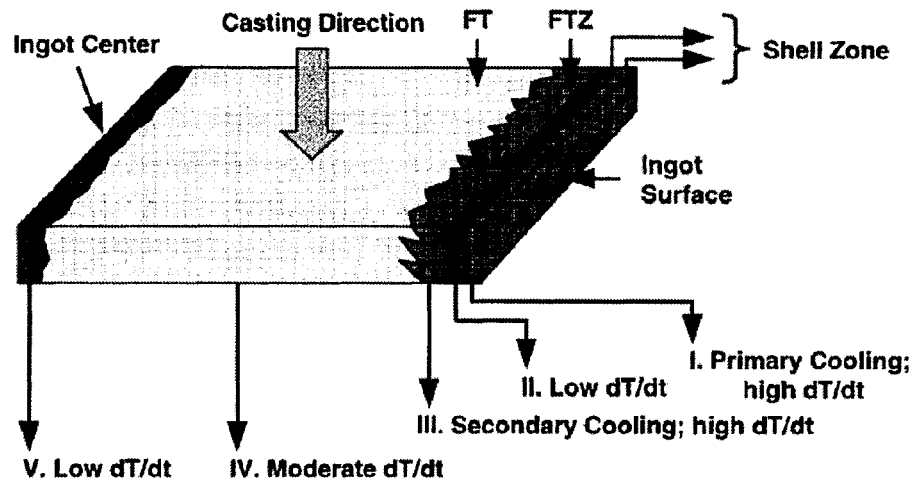


Figure 2.1: Schematic illustration of various zones across the ingot thickness. The slice is from a 1xxx-series Al ingot, and etched in 10% NaOH at 70°C for 5~20 mins<sup>8</sup>.

H. Wenstengen identified five different Fe intermetallic phases (Table 2.1) in the regions. The phases form due to different local cooling rates in each region<sup>18</sup>.

According to Figure 2.1, the following observations were made:

Table 2.1 Fe-containing phases identified in different regions in a 1xxx-series Al ingot<sup>8</sup>

Phase proportion	Phases Forming in regions I to V				
	V	IV	III	II	I
Major	Al <sub>3</sub> Fe	Al <sub>6</sub> Fe	Al <sub>m</sub> Fe	Al <sub>3</sub> Fe	Al <sub>m</sub> Fe
Intermedia	Al <sub>6</sub> Fe	Al <sub>x</sub> Fe			
Minor		Al <sub>3</sub> Fe			
Trace	$\alpha_c$ -AlFeSi*	$\alpha_c$ -AlFeSi*	$\alpha_c$ -AlFeSi*	$\alpha_c$ -AlFeSi*	$\alpha_c$ -AlFeSi*

\* Metastable cubic  $\alpha$  forms instead of stable hexagonal  $\alpha$ .

1. Primary cooling region (I): This region is always called the shell zone. Al<sub>m</sub>Fe phase forms at the boundaries of the dendrite  $\alpha$ -Al primary phase due to the high cooling rates ( $dT/dt > 20$  °C/s). The thickness of this region varies between 1 mm to 3 mm.
2. Air-gap region (II): A stable Al<sub>3</sub>Fe phase forms in this region due to the low cooling rates caused by the reheating and partially remelting of the ingot shell from inside. The thickness of this region varies between 5 mm and 7 mm.
3. Second cooling region (III): Mainly the metastable Al<sub>m</sub>Fe forms in this region due to high cooling rates ( $dT/dt \sim 10$  °C/s) caused by direct water impingement.
4. Region IV: The cooling rates are moderate and slowly decrease to the ingot center. The metastable phases Al<sub>6</sub>Fe, Al<sub>x</sub>Fe and stable phase Al<sub>3</sub>Fe form.
5. Region V: Mainly Al<sub>3</sub>Fe and small amount of Al<sub>6</sub>Fe form in this region due to low cooling rates ( $dT/dt < 1$  °C/s).

The so called FT-FTZ which is shown in Figure 2.1 forms mostly after the Shell Zone. After casting an ingot, common practice is to scalp the ingot so that the fir-tree zones can be removed, which is time consuming and uneconomic. Also, it is desirable

to cast as quickly as possible. Thus, it is of great importance to control the formation of Al-Fe and Al-Fe-Si phases in the cast ingots in order to eliminate the fir-tree zone defects.

Iron-containing phases in aluminium alloys can be separated into either eutectic or peritectic reaction, the identification of the phases in metallographic section has many ways. In modern studies, the structure of phases is frequently carried out under scanning electron microscope (SEM) in backscattered electrons or secondary electrons mode. The backscattered electrons mode permits one to obtain the maximum phase contrast and to distinguish most of the phases present by their brightness. This facilitates the identification of the iron-containing phases, which are bright by contrast the aluminium matrix because the atom number of iron is bigger than that of aluminum<sup>17</sup>.

As the cooling rate decrease from the out region to the ingot interior, that is from outer (>8 k/s) to inner (2-6 k/s), different iron-containing phases are formed. The transition is from phases  $\alpha$ -AlFeSi + Al<sub>m</sub>Fe to  $\alpha$  + Al<sub>x</sub>Fe + Al<sub>6</sub>Fe, and then to the equilibrium  $\alpha$ -AlFeSi + Al<sub>3</sub>Fe<sup>17</sup>.

Until now, it is commonly accepted that the occurrence of the metastable intermetallic phase Al<sub>m</sub>Fe is the main cause of fir-tree zone in DC cast 1xxx-series ingots, and it has been determined that the fir-tree zone was caused by the following two reason<sup>18</sup>:

- 1) Because the existence of different local cooling rates, different metastable phases form in the two adjoining zones separated by the jagged FTZ-FT interface.

2) Different phases exhibits different etching characteristics upon etching or/and anodizing. It is the etching/anodizing responses difference between the phases that makes fir-tree zone visible in ingots and structural streaks visible in sheets.

### 2.2.1 Iron intermetallic phases in the Al-Fe-Si system

Figure 2.2 shows the Al rich corner of the equilibrium Al-Fe phases diagram.

Figure 2.3 shows Liquidus projection near the Al-corner in the Al-Fe-Si phase diagram.

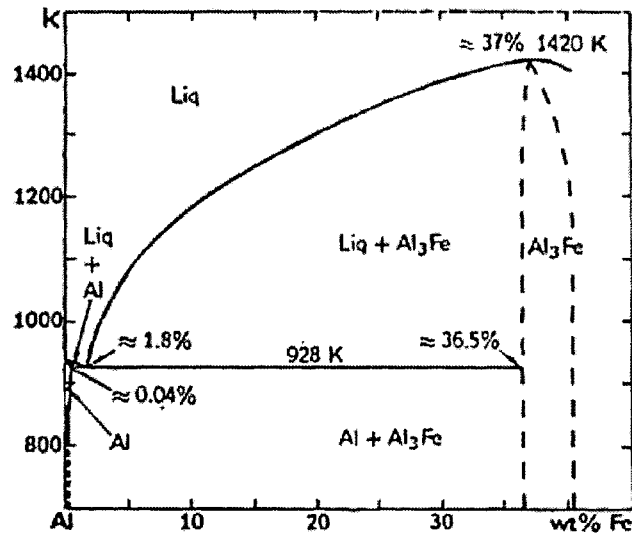


Figure 2.2: The Al rich corner of the equilibrium Al-Fe phases diagram.

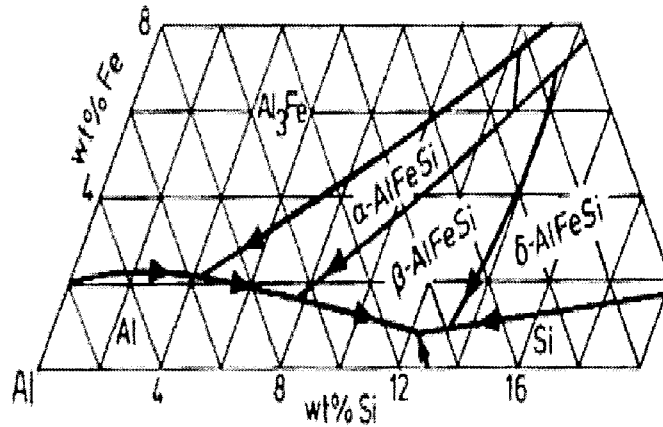


Figure 2.3: Liquidus projection near the Al-corner in the Al-Fe-Si phase diagram.

As shown in the figures above, during the solidification of Al-Fe-Si alloys, the primary  $\alpha$ -Al is the first phase solidified. Because of low solubility of Fe in solid Al, most of Fe enriched continuously in the remaining interdendritic liquid, as it reaches the eutectic composition at 1.8wt% and 655 °C, the stable eutectic intermetallic phase  $\text{Al}_3\text{Fe}$  forms between  $\alpha$ -Al phase at equilibrium cooling rates.

It is known that the existing phase diagram can be used to estimate the iron-containing phases formed in equilibrium conditions. However, in real industrial production there exists conditions nonequilibrium, so some other metastable phases such as  $\text{Al}_x\text{Fe}$ ,  $\text{Al}_6\text{Fe}$ ,  $\text{Al}_m\text{Fe}$ ,  $\alpha$ -AlFeSi,  $\beta$ -phase may form respectively. Thus, the phase diagrams are not useful to predict the metastable phases formation.

Table 2.2: Solidification reactions in the Al-Fe-Si system<sup>5, 19, 20</sup>

Reaction	Re. Temp. (°C)	Wt% Fe	Wt% Si
Binary equilibrium Liquid $\rightarrow$ Al + $\text{Al}_3\text{Fe}$	655	1.8	---
Binary non-equilibrium Liquid $\rightarrow$ Al + $\text{Al}_x\text{Fe}$	---	---	---
Liquid $\rightarrow$ Al + $\text{Al}_6\text{Fe}$	---	---	---
Liquid $\rightarrow$ Al + $\text{Al}_m\text{Fe}$	---	---	---
Ternary equilibrium liquid + $\text{Al}_3\text{Fe} \rightarrow$ Al + $\text{Al}_8\text{Fe}_2\text{Si}(\alpha\text{-AlFeSi})$	620-638	---	---
liquid + $\text{Al}_8\text{Fe}_2\text{Si} \rightarrow$ Al + $\text{Al}_5\text{FeSi}(\beta\text{-AlFeSi})$	611-615	---	---
Liquid $\rightarrow$ Al + Si + $\text{Al}_5\text{FeSi}(\beta\text{-AlFeSi})$	576-577	---	---

\* $\alpha$ -AlFeSi and  $\beta$ -AlFeSi were also reported as results of peritectic reactions<sup>21</sup>.

For the identification of different types of Fe intermetallic phases, early work was focused on the phase morphology via optical microscopy, two important Fe phases Chinese script  $\alpha$ -AlFeSi and plate-shaped  $\beta$ -AlFeSi were identified<sup>22,23</sup>. When mention the phase morphology of  $\text{Al}_6\text{Fe}$ ,  $\text{Al}_m\text{Fe}$ ,  $\alpha$ -AlFeSi,  $\text{Al}_3\text{Fe}$  and  $\beta$ -AlFeSi, two

types of phases can be identified by their morphologies<sup>24</sup>,  $\text{Al}_3\text{Fe}$  and  $\beta\text{-AlFeSi}$  can be grouped in the first group for their plate-shaped and their crystals exhibit a faced growth.  $\text{Al}_6\text{Fe}$ ,  $\text{Al}_m\text{Fe}$ ,  $\alpha\text{-AlFeSi}$  can be grouped in the second group for their shape of interdendritic channels and their complex-shaped crystals growth. The morphology of the Fe intermetallic particles cannot be established by conventional morphology in 2-D. In addition, the Fe phases can adopt morphology of great difference in different series of Al alloys<sup>25</sup>. In such a situation, identification of Fe phases based on morphology can be misleading.

In the recent years, in addition to identify Fe intermetallic phases based on their morphologies, Energy Dispersive Spectra (EDS) and Electron Backscattered Diffraction (EBSD) has been employed to study the chemical component and crystallography of the Fe phases<sup>26</sup>. As mentioned, phase identification based on the morphology is inaccurate. Also, EDS is not sufficient to determine the stoichiometry of a certain phase, because the intermetallic particles are sometimes adopt relatively small size, which may cause the EDS signal obtained from the matrix. Thus, the main purpose of getting EDS spectra is to reveal which elements are present rather than to give a quantitative analysis of the particle composition. In M.V. Kral et al's work<sup>26</sup>, EDS and EBSD technique were used as the principal methods to identify the Fe intermetallic particles accurately.

Known in the low Si content Al alloys, the  $\beta$ -phase cannot form under DC-casting conditions, so only binary phases  $\text{Al}_3\text{Fe}$ ,  $\text{Al}_x\text{Fe}$ ,  $\text{Al}_6\text{Fe}$ ,  $\text{Al}_m\text{Fe}$  and ternary phase  $\alpha\text{-AlFeSi}$  ( $\text{Al}_8\text{Fe}_2\text{Si}$ ) forms (Figure 2.4)<sup>27</sup>.



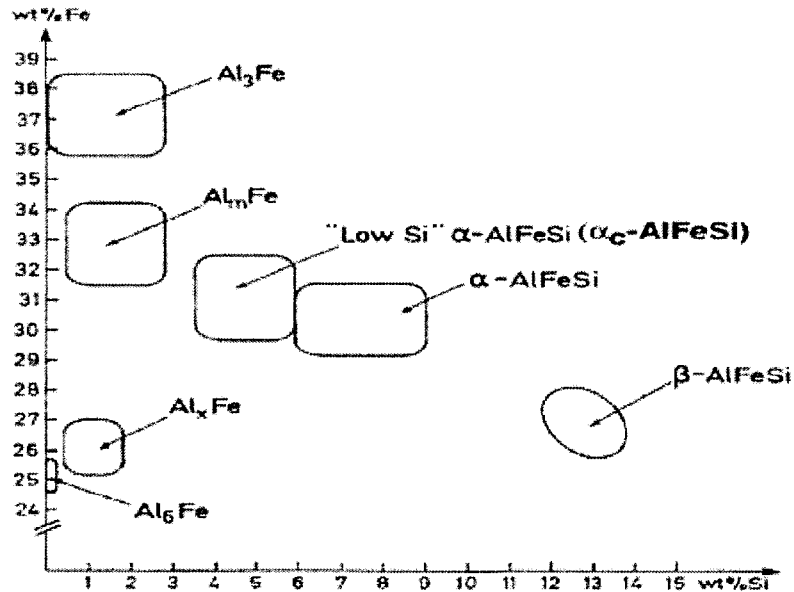


Figure 2.4: Composition of the intermetallic particles observed in DC-cast alloys<sup>27</sup>.

A review of the studies that have been carried out on the most commonly occurring Fe intermetallic phases morphology and their crystallography are present in the following section.

### 2.2.1.1 Al<sub>3</sub>Fe phase

The Al<sub>3</sub>Fe phase, which is often denoted as Al<sub>13</sub>Fe<sub>4</sub>, it is revealed by X.-Grant Chen and other researchers that the typical morphology of Al<sub>3</sub>Fe is plate like<sup>4</sup>. It is C-centered monoclinic in space group C2/m. The lattice parameters are: a=1.5489 nm, b=0.808 nm, c=1.2476 nm and  $\beta=107^{\circ}43'$ <sup>28</sup>.

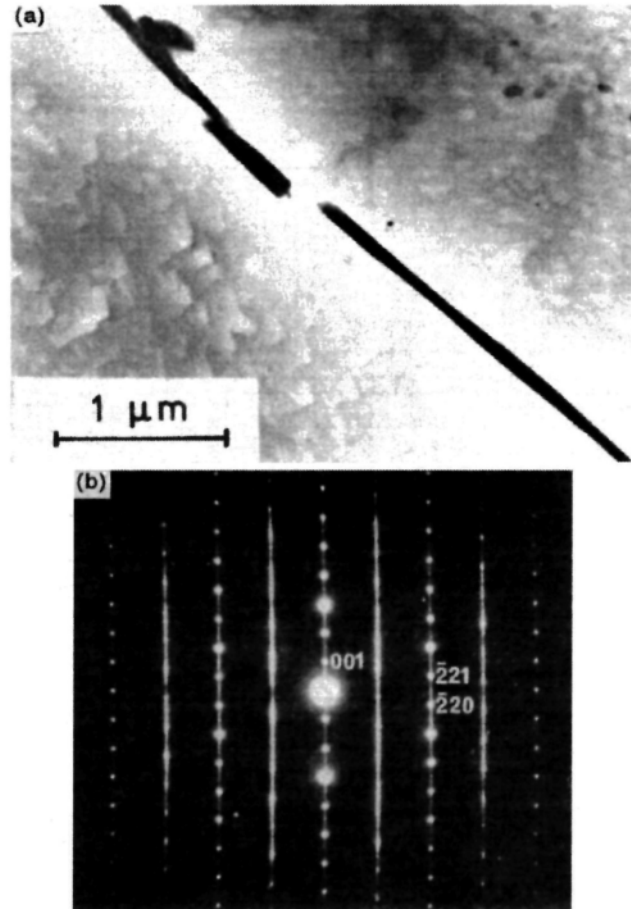


Figure 2.5: (a)  $\text{Fe}_4\text{Al}_{13}$  at grain boundaries in cast ingot 29; (b) Typical  $[110]$  diffraction pattern of a faulted  $\text{Fe}_4\text{Al}_{13}$  crystal<sup>30</sup>.

### 2.2.1.2 $\text{Al}_6\text{Fe}$ phase

$\text{Al}_6\text{Fe}$  is often found in relative rapidly solidified region in Al alloys, it has morphology of flake with several short wings. For three-dimensional morphology after deep-etching, it shows a curved plate with a number of rod-like branches<sup>4</sup>.  $\text{Al}_6\text{Fe}$  is a common intermetallic phase in DC cast Al ingots. It is isomorphous with  $\text{Al}_6\text{Mn}$ , thus the Fe can be substituted freely by Mn in the  $\text{Al}_6\text{Fe}$  lattice and lower its free energy. This can raise the thermodynamic stability of the  $\text{Al}_6\text{Fe}$  in the Mn containing alloys<sup>13,44</sup>.

The crystal has a C-centered orthorhombic structure, space group  $Cmc2_1$ . The lattice parameters are  $a=0.6492$  nm,  $b=0.7437$  nm,  $c=0.8788$  nm<sup>28</sup>. Figure 2.6 shows a typical morphology of  $Al_6Fe$  in a TEM sample and its select area diffraction pattern:

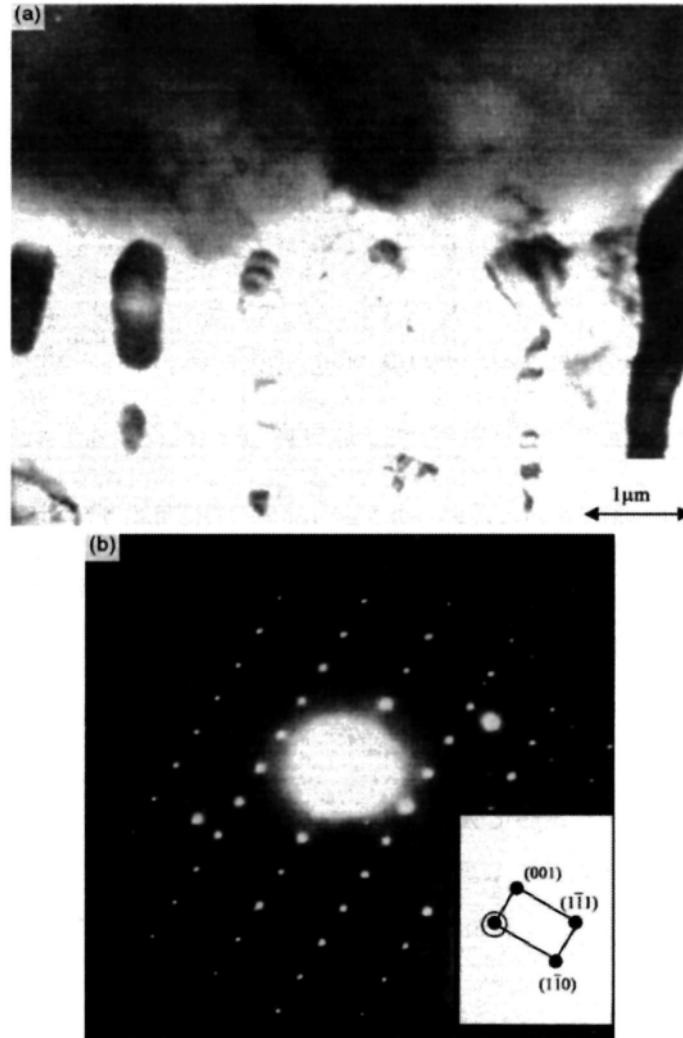


Figure 2.6: (a)  $Al_6Fe$  phases in a TEM sample; (b) SAD pattern in the  $(110)$  zones<sup>31</sup>.

### 2.2.1.3 $Al_mFe$ phase

$Al_mFe$  phase forms at regions with the highest cooling rates in the DC-casting ingots. The morphology is mostly dendrite-like, while the morphology after deep-etching exhibits a fine feathery characteristic with many fibers growing in

different orientations under SEM<sup>4</sup>. Till now, it was commonly accept that the occurrence of the  $Al_mFe$  metastable intermetallic phase is the main factor of fir-tree zones in DC cast 1xxx-series ingots<sup>18</sup>.  $Al_mFe$  phases have a body-centered tetragonal crystal structure, it has been reported by P. Skjerpe that the lattice parameters are:  $a=0.884$  nm,  $c= 2.16$  nm, space group  $I4/mmm$ <sup>32</sup>.

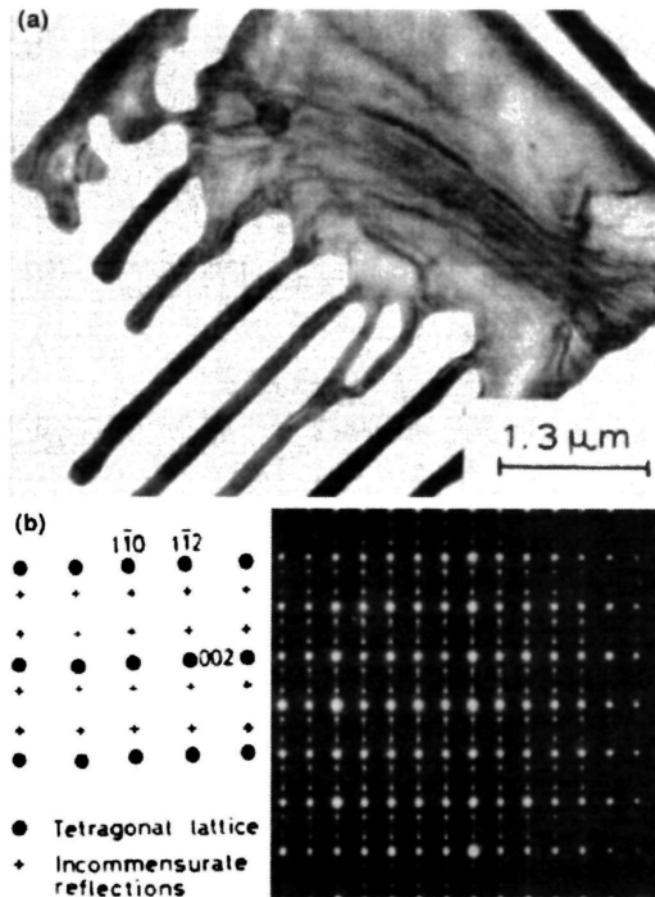


Figure 2.7:  $Al_mFe$  and corresponding [110] diffraction pattern<sup>32</sup>.

#### 2.2.1.4 $Al_xFe$ phase

It has been reported that  $Al_xFe$  forms in rapid solidification Al alloys, but the cooling rate required is less than  $Al_6Fe$ <sup>33</sup>. According to Skjerpe, the crystal structure of this phase is similar to  $Al_6Fe$ , and he found the unit cell parameters are:  $a=0.6$  nm,

$b=0.7 \text{ nm}$ ,  $c=0.47 \text{ nm}$ <sup>34</sup>.

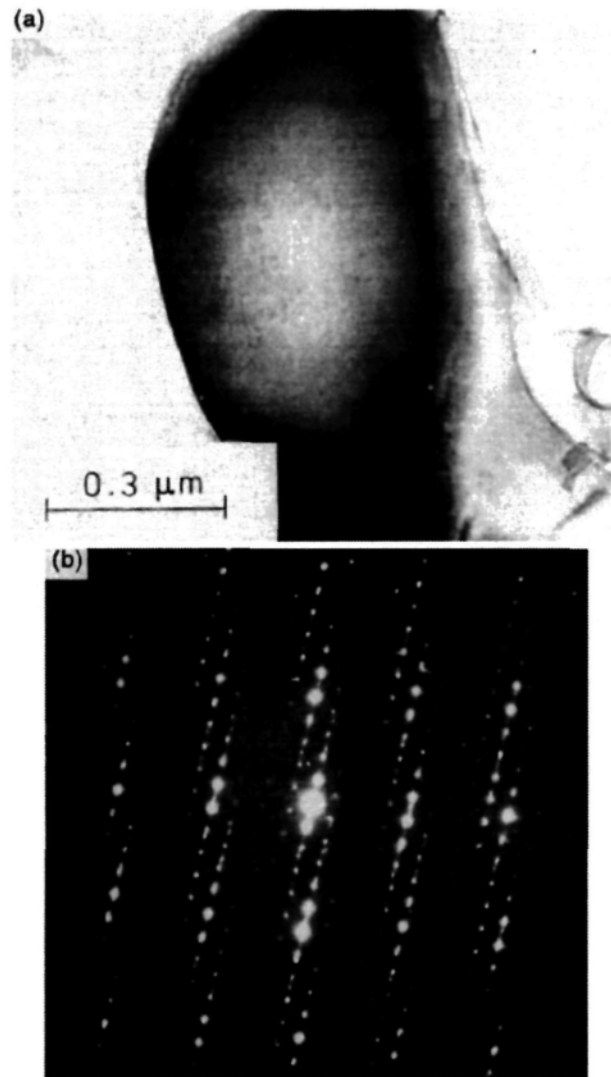


Figure 2.8: (a)  $\text{Al}_x\text{Fe}$  and its diffraction pattern<sup>34</sup>.

### 2.2.1.5 $\alpha\text{-AlFeSi}$

The  $\alpha\text{-AlFeSi}$  (sometimes write as  $\text{Al}_8\text{Fe}_2\text{Si}$ ,  $\text{Al}_7\text{Fe}_2\text{Si}$  or  $\text{Al}_{12}\text{Fe}_3\text{Si}$ ) appears a complicated dendrite form, and often described as Chinese script under optical microscope image. It can be distinguished easily from the binary Al-Fe intermetallics with its triangular edge on the front of each plate<sup>4</sup>. Some research identified  $\alpha\text{-AlFeSi}$  as cubic and some identified as hexagonal<sup>21, 35</sup>. For the hexagonal structure  $\alpha\text{-AlFeSi}$ :

the space group is  $p6_3/mmc$ . The unit cell parameters are  $a = 1.24 \text{ nm}$ ,  $c = 2.623 \text{ nm}$ <sup>28</sup>.

It was reported this phase appear at high cooling rates and low Fe and Si levels<sup>33</sup>.

It is known in the literatures that relatively high cooling rates and additions of elements of V, Cr, Mn, Cu, Mo and W can promote a body-centered structure for the  $\alpha_c\text{-AlFeSi}$ <sup>15,33</sup>.

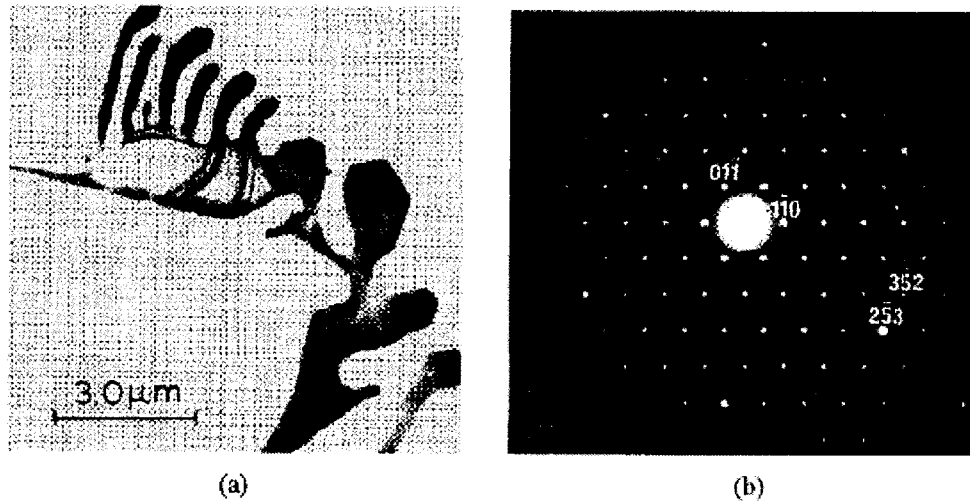


Figure 2.9: (a) Extracted  $\alpha_c\text{-AlFeSi}$  ( $\text{Al}_8\text{Fe}_2\text{Si}$ ) (b) SAD pattern in the  $\langle 111 \rangle$  zone<sup>34</sup>.

#### 2.2.1.6 $\beta\text{-AlFeSi}$

The  $\beta\text{-AlFeSi}$  ( $\text{Al}_5\text{FeSi}$  or  $\text{Al}_9\text{Fe}_2\text{Si}_2$ ) forms as thin platelets and often observed as long thin needles, sometimes with curves. It has monoclinic structure<sup>21</sup>. The lattice parameters are:  $a = b = 0.612 \text{ nm}$ ,  $c = 4.15 \text{ nm}$ ,  $\beta = 91^\circ$ .

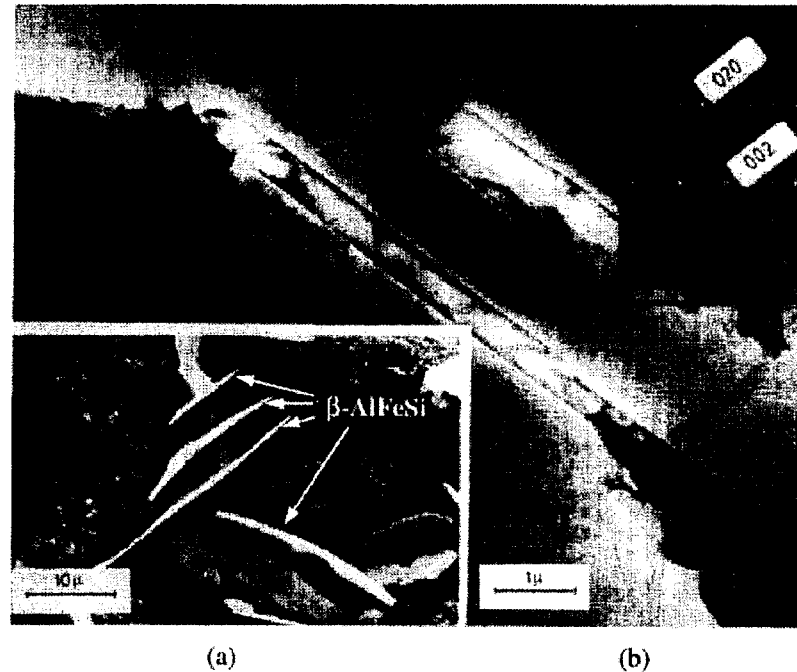


Figure 2.10:  $\beta$ -AlFeSi intermetallic phase. (a) SEM micrograph of deep-etched sample; (b) TEM image with SAD pattern<sup>36</sup>.

### 2.2.2 Factors that affect Fe phases selection in Al alloys

Different Iron phases in the aluminum alloys have varies effect to the alloy properties, so it is of great importance to have a good understanding of the factors under non-equilibrium solidification conditions that effect phase selection in Al alloys. Investigations into the intermetallic phase selection in dilute Al alloys have been ongoing for many years. Until now, it has been found that the formation of Fir-tree zones and corresponding Fe intermetallic phases is effected by the parameters such as the cooling rates, Fe/Si ratio, grain refiner, and small quantities of trace elements. A brief review of the parameters and its effects are described in the following sections:

### 2.2.2.1 Cooling rates

The cooling rates are a factor of great importance to the Fe intermetallic phases selection in Al alloy ingots. Till now, a lot of researches have been carried out to study the effect of cooling rates on the formation of Fe intermetallic phases. In B. Dutta and M. Rettenmayr's research<sup>37</sup>, it was found that with the cooling rate increase from 0.04 K/s to 3.5 K/s, the fraction of eutectic content in the alloy increased, the phase types and phase morphology are also changed. Similarly, D. Panahi et al<sup>38</sup> found that the very high cooling rates limited the precipitation of binary Al-Fe compounds and favored the formation of the ternary phase.

According to Belov's findings<sup>17</sup>, As the cooling rate decrease from the out region to the ingot interior, that is from outer (>8 k/s) to inner (2-6 k/s), different iron-containing phases are formed. The transition of phases is from  $Al_mFe$  to  $\alpha-AlFeSi$  +  $Al_xFe$  +  $Al_6Fe$ , and then to the equilibrium  $\alpha-AlFeSi$  +  $Al_3Fe$ . While PER SKJEPPE's<sup>39</sup> discover that at a cooling rate of 6 to 8 K/s, the dominating phases are  $\alpha-AlFeSi$  and  $Al_mFe$ , while at a cooling rate of 1 K/s, the dominating phases are  $Al_3Fe$  and  $Al_xFe$ ,  $Al_6Fe$  forms at cooling rates 1 to 10 K/s and  $Al_mFe$  forms at cooling rates exceeding 10 K/s.

In previous studies, a critical (minimum) cooling rate required for the  $Al_mFe$  phase formation was determined in some alloys. In AA1050 alloy (0.25wt% Fe, 0.13wt% Si, 0.03wt% Ti), the cooling rate is 8°C/s, as shown in Figure 2.11. In AA5005 alloy (0.43wt% Fe, 0.13wt% Si, 0.85wt% Mg, 0.03wt% Ti)<sup>40</sup>, the cooling rate is 8.5°C/s.



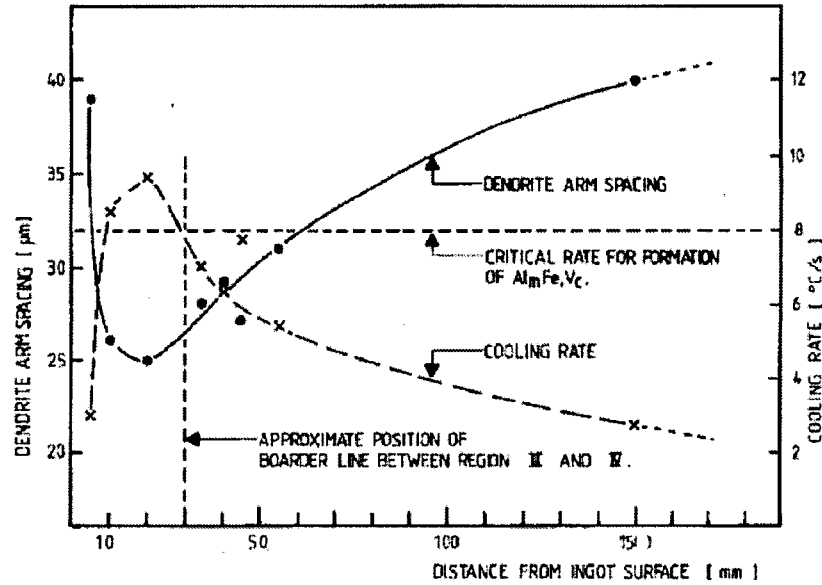


Figure 2.11: Cooling rate and corresponding secondary dendrite arm spacing as a function of distance from ingot surface, critical cooling rate for  $\text{Al}_m\text{Fe}$  is given<sup>33</sup>.

In some literatures, the critical cooling rates for  $\text{Al}_3\text{Fe}$ ,  $\text{Al}_6\text{Fe}$  and  $\text{Al}_m\text{Fe}$  are also given, see Table 2.3.

Table 2.3: Critical cooling rates for the formation of some Fe intermetallic phases

Researcher	Composition	Critical cooling rates ( $^{\circ}\text{C/s}$ )		
		$\text{Al}_3\text{Fe}$	$\text{Al}_6\text{Fe}$	$\text{Al}_m\text{Fe}$
H. Kosuge and I. Mizukami <sup>41</sup>	Al-0.6wt Fe-0.01wt% Si	$dT/dt < 2$	$2 < dT/dt < 20$	$dT/dt > 20$
Young et al <sup>42</sup>	Hypoeutectic Al-Fe alloy	$dT/dt < 0.9$	$3 < dT/dt < 11$	$dT/dt > 11$
Miki et al <sup>43</sup>	1xxx-series	$dT/dt < 1$	$1 < dT/dt < 10$	$dT/dt > 10$
Backerud <sup>44</sup>	Al-1wt% Fe	$dT/dt < 3.2$	$dT/dt \geq 3.2$	---

From the findings that has been made, we can find there is a similar point that under the higher cooling rates, form the more metastable phases.

### 2.2.2.2 Fe/Si ratio

There is no doubt that the impurities Fe and Si play an important role for the formation of Iron intermetallic phases<sup>17, 45</sup>. In addition, Fe/Si ratio also has effect on the Fe intermetallic phases selection. S. Brusethaug et al found that Fir-tree zones appear at Fe/Si of about 2, while the Fir-tree zone can be eliminate at Fe/Si ration of larger than 3<sup>16</sup>. Furu et al found when the Fe/Si is of 1, the Fir-tree zones is much larger than that of 3.4 and 6.3<sup>11</sup>.

Table 2.4: Effect of Fe/Si ratio on FTZs width in Al-Fe-Si alloy ingots<sup>11</sup>

Cast No.	Fe (wt%)	Si (wt%)	Fe/Si ratio	FTZ Width (mm)
1	0.15	0.15	1	70
2	0.48	0.14	3.4	9
3	0.82	0.13	6.3	0

### 2.2.2.3 Grain refinement

The purpose of grain refinement is to produce a refined, equiaxed grain structure with modified second phase particle morphology through the thickness of the DC cast ingot. The most common grain refiner being used are 6%Ti, 3%Ti, 5%Ti-0.1%B, 5%Ti-1%B, and 5%Ti-0.2%B. All these are based on Al, and its compositions are in commercial use for a variety of applications and products.

In addition of grain refinement, experiments have shown that the morphology of the insoluble iron-rich phase can be influenced, not only by the grain refiner composition, but also by the manufacturing route used by different suppliers. This would indicate that the nucleation mechanism of the iron-rich particles is strongly

influenced by the grain refinement process<sup>46</sup>.

It was found by X.-G. Chen<sup>12</sup> that addition of AlTiB, AlTiC and AlB refiner promotes Al<sub>m</sub>Fe formation and enlarges the fir-tree zones. Moreover, he had an observation of direct nucleation of Al<sub>m</sub>Fe on TiB<sub>2</sub> and TiC particles which maybe the cause of promote Al<sub>m</sub>Fe<sup>12</sup>. In S.J. Magges et al's research<sup>13</sup>, the addition of Ti-B grain refiner, which can introduce TiB<sub>2</sub> particles, caused cubic  $\alpha$  phase to become the dominant intermetallic phase and eliminated a visible FTZ boundary in certain Fe/Si ratio. He gave the reason why the TiB<sub>2</sub> assisted the nucleation of Al<sub>m</sub>Fe, which is probably hexagonal TiB<sub>2</sub> promotes the nucleation of phases with higher symmetry, such as cubic  $\alpha$  phase and tetragonal Al<sub>m</sub>Fe rather than those in lower symmetry, such as orthorhombic Al<sub>6</sub>Fe and monoclinic Al<sub>3</sub>Fe. M. W. Meredith and et al<sup>14</sup> found in their research that the addition of grain refiner to a dilute Al-Fe binary alloy can slightly change the phase balance, increasing the presence of Al<sub>3</sub>Fe and decreasing Al<sub>6</sub>Fe, while the dominant phase is always Al<sub>6</sub>Fe. The addition of refiner radically changes the morphology of these phases as the classical rod-like appearance of Al<sub>6</sub>Fe is replaced by the curved, plate-like intermetallic phases.

#### **2.2.2.4 Trace elements effects**

Some trace levels of elements, such as Cu, Mn, Zn, Ti, V, Ni and so on, often appear as impurities in the commercial Al alloy ingots. It has been reported by some researchers that such trace levels elements can have a strong effect on the phase selection and fir-tree zones characteristics in dilute Al-Fe-Si alloys<sup>15</sup>, but this is still

under controversial.

Table 2.5: Effect of trace elements on the formation of Fe intermetallic phases<sup>12, 13, 47</sup>

Element	Phase Promoted	Alloy	Method
Mg	No major effect	Al-0.41%Fe-0.11Si	DC simulator
Ti	No major effect		
Mn	Al <sub>3</sub> Fe		
Cr	Al <sub>m</sub> Fe	AA5005	
V	Al <sub>m</sub> Fe	AA1050	
Ni	?	?	

Allen et al<sup>48</sup> found in their research that V impurity and Al-Ti-B grain refiner can affect the solidification behavior and play an important role in phase selection during industry DC casting processes, in addition to the effects of solidification rates and bulk Si content. Control of V and grain refiner content in industry Al alloys may therefore provide a means of influencing secondary phase content and ultimately material properties, without having to redesign the alloy composition or change the casting parameters.

S. Maggs et al<sup>13</sup> explained that the addition of trace elements can alter both the nucleation and growth kinetics of a certain phase and make it lose out to another phase. Impurities may be segregated to the growth front and produce solutal undercooling and hence suppress growth velocity. Conversely, impurities may promote twinning which in turn promote the growth of a faceted intermetallic as

$\text{Fe}_4\text{Al}_{13}$  by providing a higher density of re-entrant edges and corners to which atoms can attach more easily<sup>13</sup>.

In general, the effect of trace elements on the phase selection can be the following two reasons<sup>13</sup>:

1. Trace elements that are strongly partitioned to the interdendritic liquid during the final stages of solidification can affect solidification behavior, which cause a constitutional undercooling and makes the phase with higher nucleation temperature in the undercooling liquid easily nucleate and grow.
2. Trace elements may dissolve into the phase by substitute some fraction of the Fe atoms in the crystal structure. By altering the free energies and hence change the thermodynamic characteristics of the phases. For example, Mn and Cu can stabilize  $\text{Al}_6\text{Fe}$  by forming  $\text{Al}_6(\text{Fe}, \text{Cu})$  and  $\text{Al}_6(\text{Fe}, \text{Mn})$ .

## 2.3 DC casting simulator techniques

In the industry practice, large DC cast Al ingots were cast, which is too expensive and impossible to carry out in the laboratory. Thus, in order to reproduce the cooling rate near the casting surface of industry DC cast Al ingot, some lab-scale researches have been carried out in DC casting simulators<sup>12, 13</sup>. In this method, the melt Al liquid is poured into a cylindrical insulating mold with removable chill plate. initially (about 20 seconds) the cooling rate is slow due to poor contact with the mold, later fast when the water impinge directly on the bottom surface of the ingot, and then the cooling rates decrease due to the increasing conduction path. Thus, long

cylindrical alloy rod samples directionally solidified by chilling from the bottom.

During the solidification process, the growth occurs parallel and opposite to the heat flow direction, the control of sample solidification conditions can be carried out by monitoring the local cooling rates got from the thermal couples inserted into the insulating mold<sup>12</sup>.

In the DC simulator casting Al ingots, although it is difficult to obtain a microstructure exactly the same as industry DC casting ingot, it can still be viewed that a range of cooling conditions are along the height of an ingot, which cause Fe intermetallic phases transition from the chill end to the top of an ingot.

When compare the DC simulator technique that was used in the present research with the Bridgeman furnace, we can clearly found that the DC simulator is easier to build and more economic used in the lab.

## **2.4 EBSD technique**

The Electron Backscatter Diffraction (EBSD) is based on diffraction technology, which is valuable when the chemical inspection is inaccurate, the phase is non-equilibrium or the phase can formed in different crystallographic systems<sup>49</sup>. EBSD can be used to identify the crystal structure of a phase and to evaluate the crystallographic orientation.

EBSD obtains crystallographic information from tilted polished samples in a scanning electron microscope (SEM). The electron beam strikes the sample and the electrons are elastically scatter beneath the surface. Electrons diffracted according to

Bragg's law form a pattern on a fluorescent screen. Each lattice plane is represented in the diffraction pattern by a Kikuchi bands<sup>50</sup> (Figure 2.12). By comparing to theoretical data, the crystallographic system of the phase and orientation can be identified<sup>51</sup>.

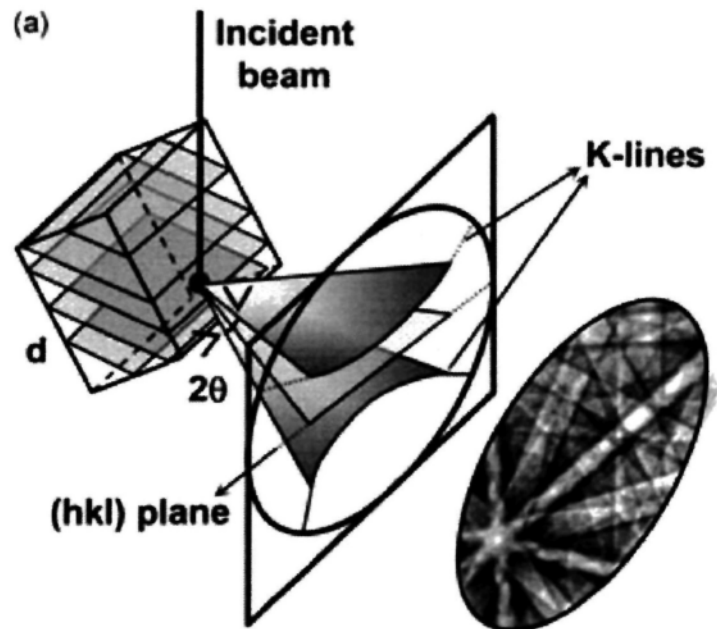


Figure 2.12: Formation of Kikuchi bands by back-scattered Electrons<sup>52</sup>.

---

## Chapter 3 EXPERIMENTAL PROCEDURES

### 3.1 Alloy preparation

In this study, both the commercial and experimental AA5657 alloys will be used, the chemical composition of the as-received commercial DC cast AA5657 ingot is shown in Table 3.1. The material was supplied in slice form that cut from the cross section of a commercial ingot from Alcan Laterriere plant, the dimension of the DC cast ingot is about 635 mm × 2030 mm in cross-section.

Table 3.1: Chemical Composition of the Industrial DC cast AA5657 ingot

Alloy	Element (wt%)											
	Si	Fe	V	Ni	Mg	Cu	Ti	Mn	Cr	Zn	B	Al
AA5657	0.04	0.07	0.0175	0.007	0.82	0.05	0.02	0.003	0.001	0.01	0.001	Bal.

The Al-5wt% V and Al-20% Ni master alloy are used to change the V and Ni levels in AA5657 base alloy.

### 3.2 Melting and Casting

The alloy ingots are melted in a crucible using an electrical resistance furnace. The melting temperature is kept at about  $740 \pm 5^\circ\text{C}$ . At this temperature, the master alloy of V and Ni are added in the liquid to give different levels of V and Ni content. After V and Ni was total melt, the liquid was kept for 15 minutes for homogenate.

In the industry practice, Al alloy ingots always cast with a dimension as much as 635 mm x 2030 mm in cross-section and 7620 mm in length<sup>9</sup>, which is impossible to duplicate in the lab. Thus, a DC casting simulator (Figure 3.1 and Figure 3.2) is build



and used in the casting of AA5657 alloy ingots, which consists of mainly five parts: security cover, insulating mold, thermocouples, removable copper plate and water jet. This apparatus can produce a similar solidification condition on the sub-surface region of the ingots.

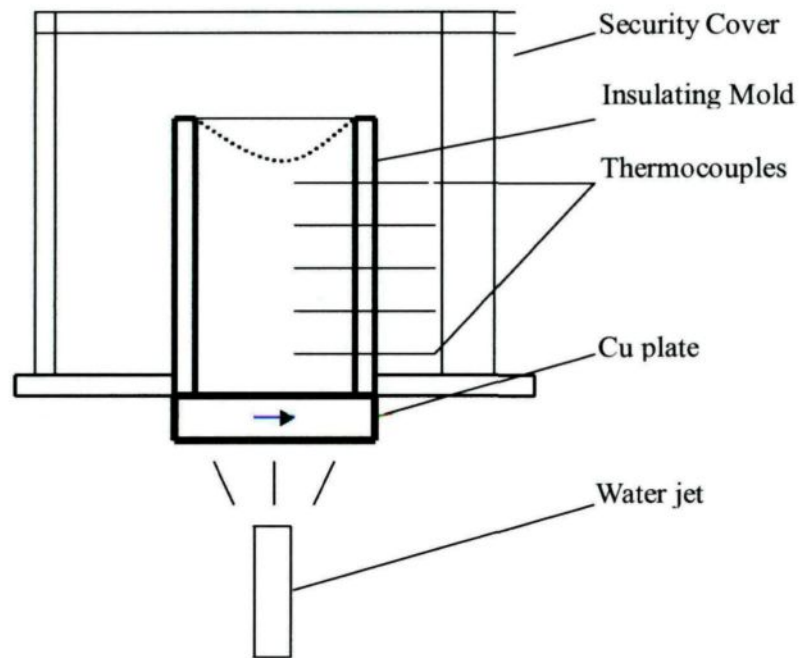


Figure 3.1: Schematic illustration of DC simulator apparatus

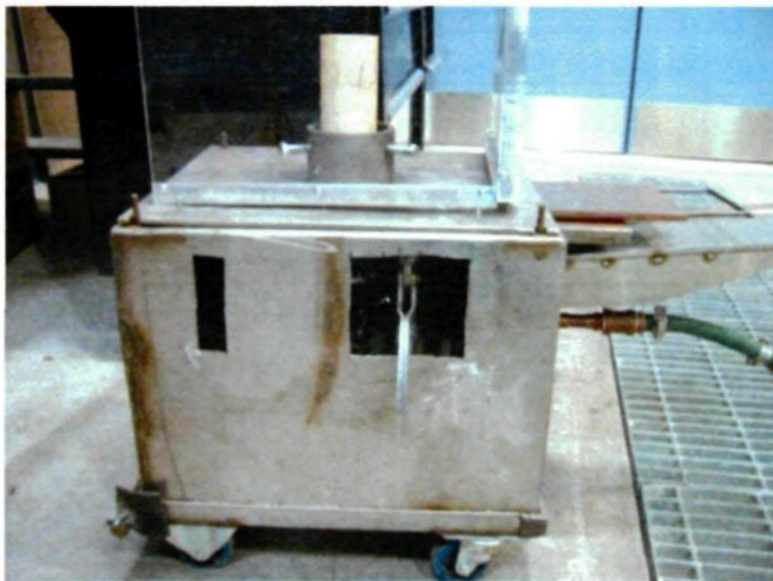


Figure 3.2: DC casting simulator used in present research.

Before casting, the insulating mold was heated to 500°C to remove moisture content. The AA5657 base alloy was melt in an electric furnace (Figure 3.3).



Figure 3.3: The electric furnace used in the lab.

The molten metal was poured into the mold fixed in the DC simulator. After about 20 seconds when the Al skin on the bottom was strong enough to hold the Al liquid, the Cu plate was pulled away to allow water to impinge directly onto the bottom surface of the ingot. During the casting process, the holding time is of great importance to the ingots microstructure, therefore impact on the position of the Fir-tree zone. There is no grain refiner addition during the casting process, the grain refiner remaining is coming from the DC cast ingot that was melted. The ingots cooling conditions during solidification process were measured by using five thermocouples insert into the center of the mold (Figure 3.1).

A Thermal Analysis test was carried out to study the solidification behavior of AA5657 alloy: poured the melting liquid into a thin wall steel crucible, two

thermocouples were inserted into the center of the crucible (Figure 3.4), the Al liquid in the crucible was cooled slowly to room temperature. The cooling curve can be obtained from the computer connected to the thermocouples.

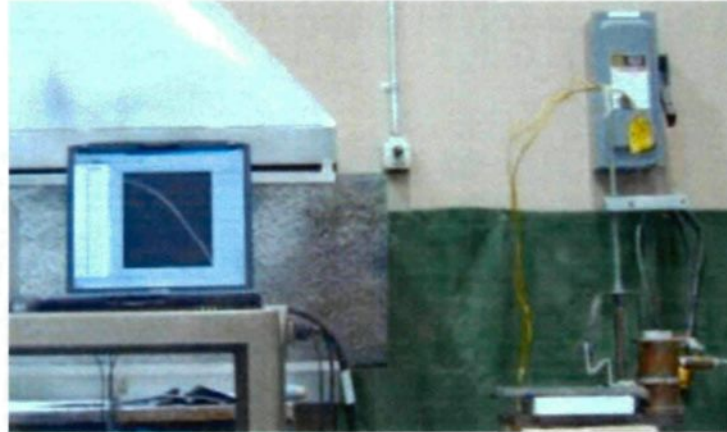


Figure 3.4: Cooling curve test apparatus used in the lab.

The ingots cast via DC simulator are with a dimension of 38 mm in diameter and 150 mm in length. In order to reduce the effect of cooling rates from the top and around, analysis samples are only taken from the center of the ingots within 120 mm from the chill end.

### **3.3 Sample analysis and Characterization**

#### **3.3.1 Chemical analysis**

Alloy discs for chemical analysis were cast every time just after the sample ingots were cast. The work of chemical analysis was done in the lab of ARDC Rio Tinto Alcan. The alloys chemical composition results are given in Table 3.2:

Table 3.2: Chemical compositions of the DC simulator cast alloys (wt. %).

Alloys	Elements								
	V	Ni	Fe	Si	Mg	Cu	Mn	Ti	Al
*A01	<b>0.017</b>	<b>0.007</b>	0.071	0.045	0.82	0.047	0.003	0.018	Bal.
A02	<b>0.024</b>	<b>0.007</b>	0.075	0.049	0.82	0.049	0.003	0.019	Bal.
A03	<b>0.033</b>	<b>0.007</b>	0.072	0.064	0.81	0.056	0.003	0.02	Bal.
A04	<b>0.048</b>	<b>0.008</b>	0.078	0.049	0.83	0.049	0.003	0.02	Bal.
A05	<b>0.017</b>	<b>0.015</b>	0.07	0.045	0.81	0.047	0.003	0.021	Bal.
A06	<b>0.018</b>	<b>0.027</b>	0.072	0.044	0.79	0.051	0.003	0.021	Bal.
A07	<b>0.018</b>	<b>0.039</b>	0.072	0.044	0.79	0.047	0.003	0.021	Bal.
A08	<b>0.017</b>	<b>0.057</b>	0.077	0.047	0.84	0.049	0.003	0.024	Bal.
A09	<b>0.026</b>	<b>0.024</b>	0.072	0.052	0.82	0.053	0.003	0.023	Bal.
A10	<b>0.038</b>	<b>0.025</b>	0.07	0.044	0.78	0.045	0.003	0.02	Bal.

\* A01 is base DC simulator cast AA5657 alloy.

### 3. 3.2 Optical Microscopy

After the ingots were casted, the ingots was cut into two parts longitudinally. One half was used to examine the macrostructure as growth direction and Fir-tree zones. The other half was for microstructure observation.

For metallographic examination, the specimens were taken from different position of the ingots, mounted using epoxy resin and hardener mixture. The grinding was first carried out on silicon carbide papers on a rotating wheel automatically. The grit size is decreasing, (120, 220, 320, and 500). After grinding, diamond abrasive of  $6\mu\text{m}$  and  $1\mu\text{m}$  are used to eliminate the scratches on the sample surface. The final step



0.05 $\mu\text{m}$  of polishing is done with a colloidal silica suspension.

In the present study, a system of CLEMEX image analysis with Nikon Eclipse Me 600 optical microscope (Figure 3.5) was used.



Figure 3.5: Clemex image analysis system with Nikon Eclipse Me 600 optical microscope.

### 3.3.3 Deep-etching of metallographic sample

In order to reveal the original morphology of Fe intermetallic particles, deep-etching and SEM technique are used. This technique can also be useful for the study of nucleation and growth behaviour of the Fe intermetallic phases. There were two different etchants used in the present study. One is 10% NaOH solution at 60~70°C, the other is 20% HCl at room temperature. The former is mainly used for AA5657 alloy ingots, while the latter was used in the study of 1xxx-series ingot. Put the surface of a finely grounded metallographic specimen in the etchant solution. The etching time varies from 5~10 minutes, after that the aluminum matrix on the surface layer of the specimen was dissolved while leave the intermetallic particles unaffected.

The etched sample is studied by using Scanning Electron Microscope (SEM)

system under the secondary electron imaging mode. The SEM system is JEOM JSM-6480LV (Figure 3.6). The energy dispersive spectroscopy is also used to give a chemical composition analysis.



Figure 3.6: JEOM JSM-6480LV SEM system

### **3. 3.4 Electron Backscatter Diffraction (EBSD)**

After the metallurgical study, EBSD technique was used to further the identification study of Fe intermetallic phases. In the present research, EBSD was used as the principal technique for the phase identification.

In order to identify the Fe intermetallic phases, EBSD technique was employed in present study. Using EBSD technique, the four types of Fe intermetallic phases appearing in the cast ingot were identified. It was found that the crystal structure of the intermetallic compound with a feathery like morphology was similar to  $\text{Al}_m\text{Fe}$ ; The crystal structure of the intermetallic phase with chinese-script morphology was agree well with  $\text{Al}_7\text{Fe}_2\text{Si}$ ; The crystal structure of the intermetallic phase with curved

plates morphology was agree well with  $\text{Al}_6\text{Fe}$  and the crystal structure of the intermetallic phase the needle like morphology can match well with  $\text{Al}_3\text{Fe}$ .

### 3. 3.4.1 Fe intermetallic phases database creation

The EDS spectra show that every intermetallic particle contain Al and Fe, so all the compound listed in Pearson's Handbook of Crystallographic Data for Intermetallic phases<sup>28</sup> containing Al and Fe were selected as possible phases for identification (See appendices A). The crystallographic data were entered into HKL Channel 5 Twist diffraction database creator.

For the identification of each intermetallic particle, the HKL software automatically suggests solutions for a given EBSD pattern ranked by lowest MAD (Mean Angular Deviation) as an index of 'goodness of fit'. For acceptable identification solutions, the MAD number should be less than 0.7 in the present study.

### 3. 3.4.2 EBSD sample preparation

The use of EBSD has quite high requirement of the sample quality. In the present study, a procedure for EBSD sample preparation was developed (Table 3.3).

Table 3.3: Four steps procedures for the EBSD sample preparation.

Steps	Load (N)	Speed rmp/Direction	Time (minutes)
120-500 grit SiC, water	slightly hand press	60/Same	Until plane
6- $\mu$ diamond abrasive	15	90-120/Same	8
1- $\mu$ diamond abrasive	15	90-120/Same	2
0.05 Microcloth with colloidal silica	10	60-90/Same	3.5

As illustrated in Figure 3.7, the dashed line on the EBSD sample is parallel to the casting surface/chill end, which stands for a position to be studied. Six fields with dimensions about  $150\mu\text{m} \times 150\mu\text{m}$  were chosen along the line under a magnification of 500X. On the corner of each field, four marks were made using Micro hardness in order to find the field easily under SEM:

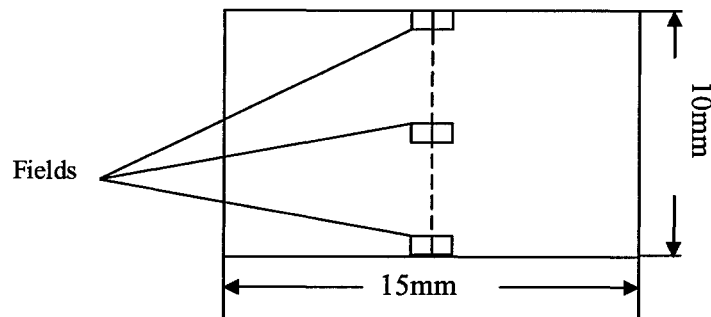


Figure 3.7: Schematic illustrates the 6 fields chosen in a sample.

The particles size smaller than  $0.5\mu\text{m} \times 0.5\mu\text{m}$  in dimension cannot be identified due to the poor quality of diffraction patterns, which take up about 5% of the total particles. Generally, there are totally 80 ~ 100 particles analyzed in the six fields of a sample.

### 3. 3.4.3 Fe intermetallic Phases quantafication

After all the Fe intermetallic particles were identified, phase quantafication was done by CLEMEX image analysis. In addition to the volume fraction, some other parameters of the Fe intermetallic particles such as Count, Perimeter, and Density were measured by CLEMEX image analysis.

By using CLEMEX Image Analyzer, there are two steps to calculate the area



percentage of each type of Fe intermetallic phases in one field. Firstly, all the Fe intermetallic phases appear on the image are selected automatically according to the brightness difference between Fe intermetallic particles and Al matrix. Secondly, each type of Fe phase is distinguished and selected manually according to the EBSD identification results.

The routine of CLEMEX Image Analyzer used in the present study see appendices B.

## Chapter 4 Results and Discussion

### 4.1 Phase characterization in an AA5657 DC cast ingot

#### 4.1.1 Ingot microstructure

The microstructure of AA5657 DC cast ingot is shown in Figure 4.1.

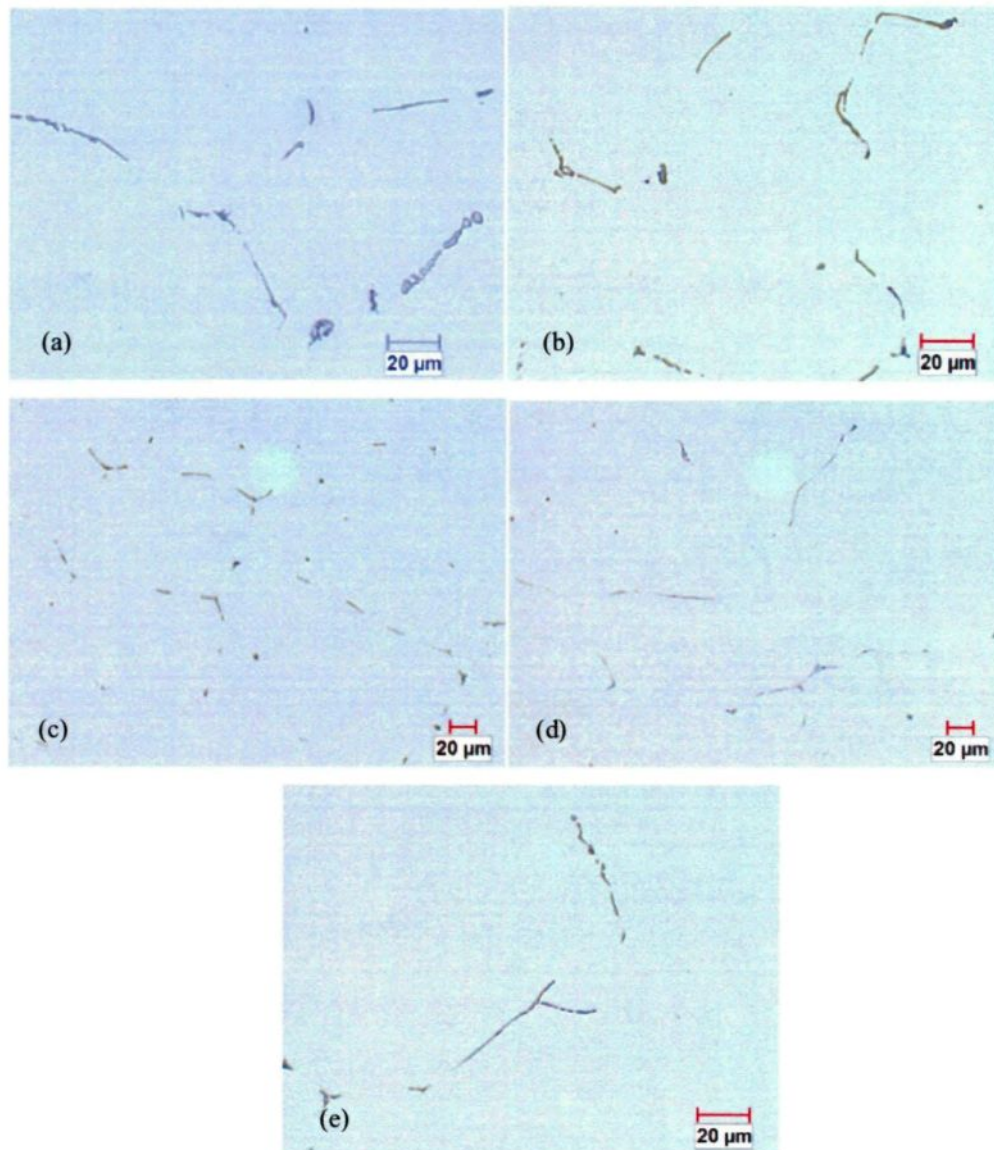


Figure 4.1: Microstructure of AA5657 cast ingot at the position away from casting surface at 10 mm (a), 40 mm (b), 90 mm (c), 140 mm (d) and 300 mm (e).

The microstructure of AA5657 alloy ingot show that the Fe intermetallic phases are grow along the interdendritic regions of aluminum cells, which indicates that the Fe intermetallic phases are form in the last stage of solidification process.

#### 4.1.2 Fe intermetallic phases morphology and EDS results

In the DC cast AA5657 ingots, four kinds of typical morphologies of Fe intermetallic phases were found. The morphologies of the Fe intermetallic particles under Optical Microscope and SEM were shown in Figure 4.2 and Figure 4.3, Figure 4.4 shows the phase morphologies in deep-etching samples:

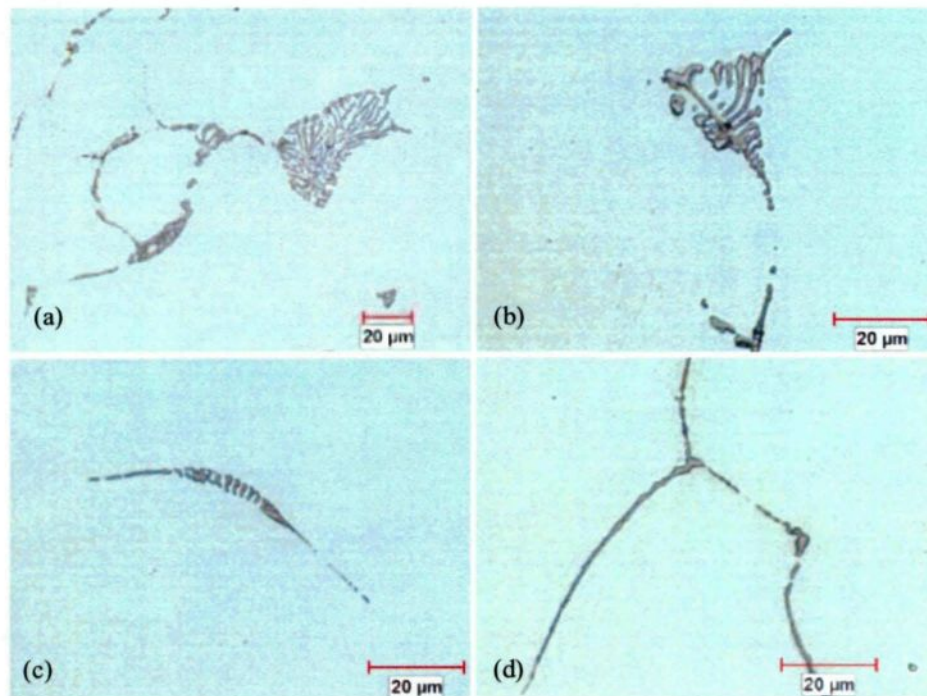


Figure 4.2: Typical Fe phases morphologies in the AA5657 cast ingot: (a) fine feathery like, (b) Chinese script, (c) curved plates with swings, (d) needle like.

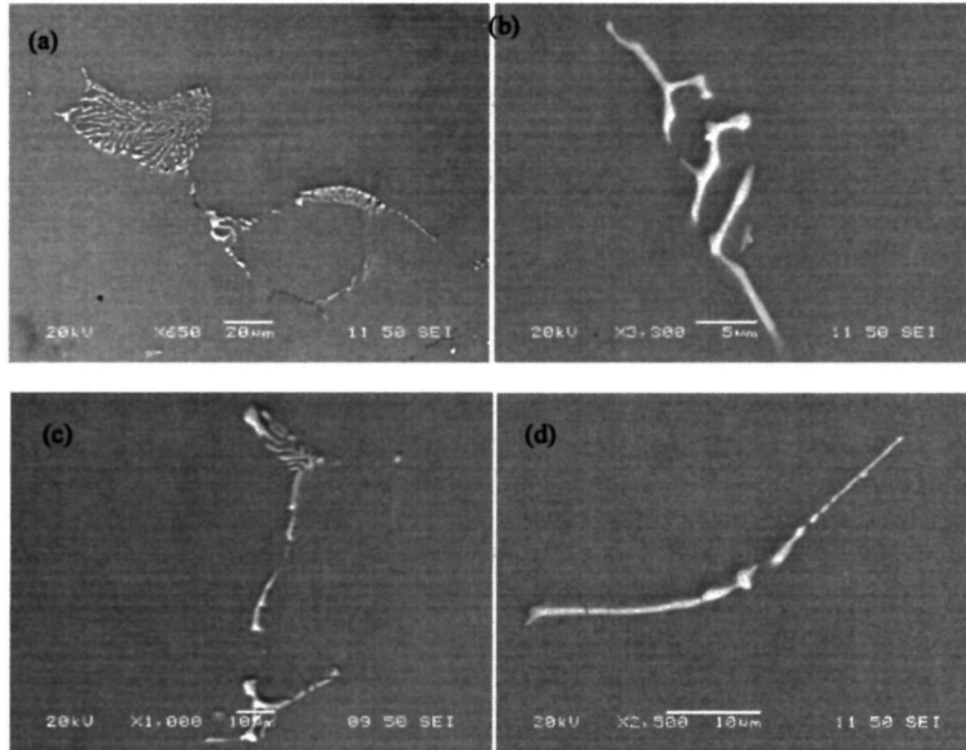


Figure 4.3: Fe intermetallic phases morphology under SEM. (a) fine feathery like, (b) Chinese script, (c) curved plates, (d) needle like.

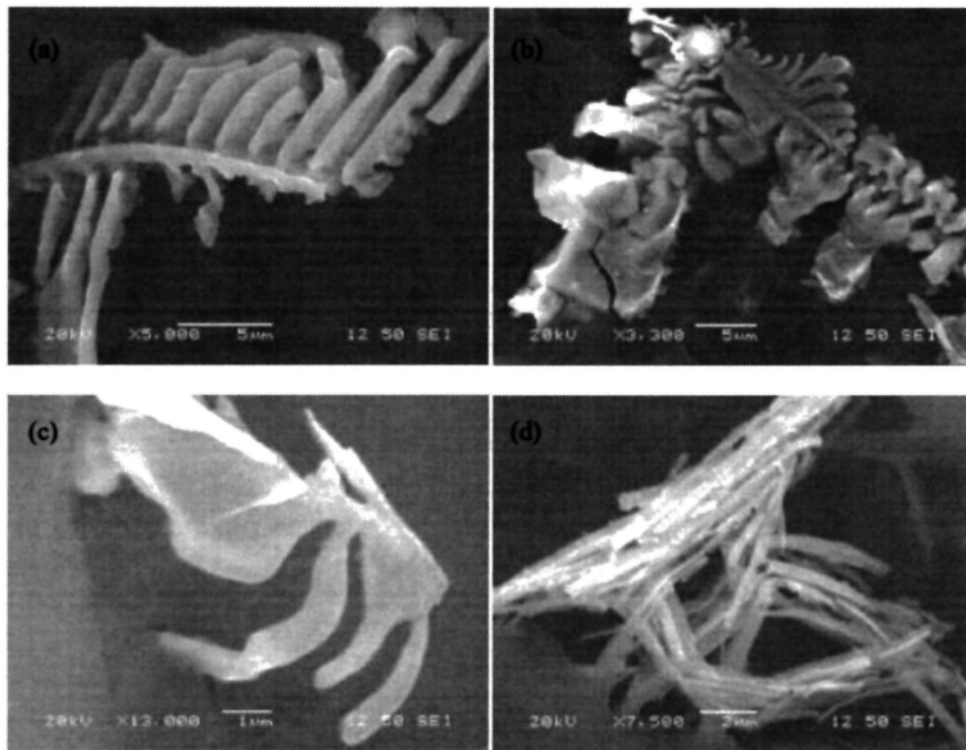


Figure 4.4: Fe intermetallic phases morphology (deep-etching) under SEM. (a) fine feathery like, (b) Chinese script, (c) curved plates, (d) needle like.

The EDS results of different phases are shown in Figure 4.5:

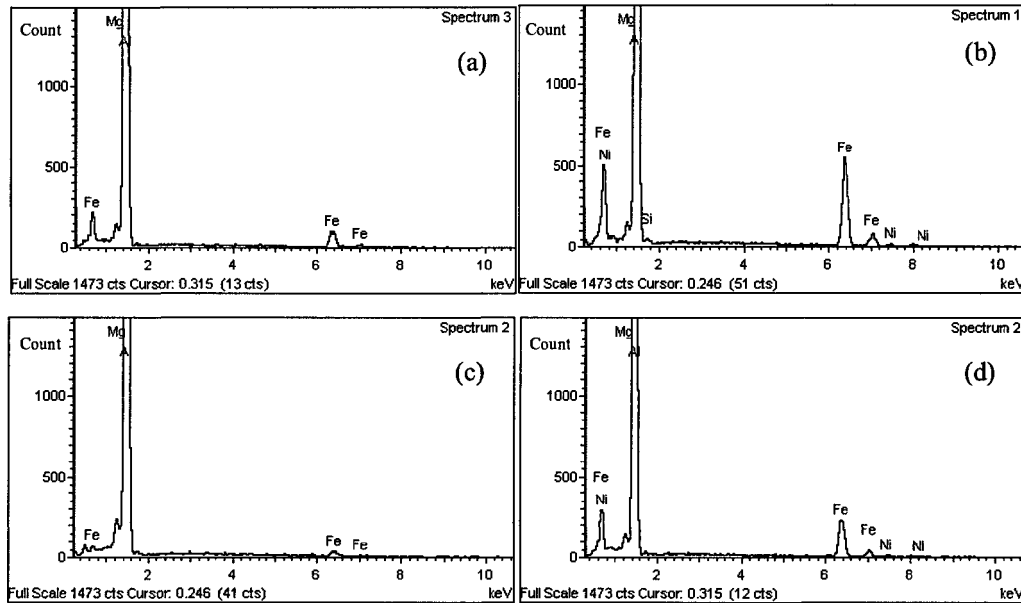


Figure 4.5: Typical EDS results of Fe intermetallic phases. (a) Fine feathery like, (b) Chinese script, (c) curved plates, (d) needle like.

From the EDS results in Figure 4.5, we can know clearly that these particles are Fe containing phases. Moreover, Mg was detected in each particle of Fe intermetallic phases, because AA5657 alloy contains 0.82 wt% Mg. In addition, in some Chinese script and needle like Fe intermetallic phases, some amount of Ni content can be frequently found (Figure 4.5 (b) and Figure 4.5 (c)). Especially, in Figure 4.5 (b), we can see that the Chinese script particles always contain some Si, which makes it easier to be distinguished from other phase.

Although it is possible to identify some Fe intermetallic phases according to their typical morphology and EDS spectra, it is still not sufficient, sometimes may even cause misidentification due to two reasons:

(1) As found in the present study only a small part (about 20%) of Fe intermetallic particles appears the typical morphology. In addition, according to the

work of M.V. Kral<sup>53, 54</sup> et al and Y.J. Li et L. Arnberg<sup>55,56</sup>, a certain Fe intermetallic phase can have different morphologies.

(2) EDS can give a semi-quantitative compositional analysis of the particle, the stoichiometry of Fe phases is still uncertain according to EDS results. Moreover, the Fe intermetallic particles often adopt relatively small size (i.e. 1 ~ 5  $\mu\text{m}$ ), which may cause the EDS signal be obtained from the matrix and make the results at least partially incorrect.

#### **4.1.3 Phase identification using EBSD technique**

By using EBSD technique, the four types of Fe intermetallic phases appearing in the cast ingot were identified. It was found that the crystal structure of the intermetallic compound with a feathery like morphology was similar to  $\text{Al}_m\text{Fe}$ ; The crystal structure of the intermetallic phase with chinese-script morphology was agree well with  $\text{Al}_7\text{Fe}_2\text{Si}$ ; The crystal structure of the intermetallic phase with curved plates morphology was agree well with  $\text{Al}_6\text{Fe}$  and the crystal structure of the intermetallic phase the needle like morphology can match well with  $\text{Al}_3\text{Fe}$ . The following images show the diffraction patterns and its corresponding solutions of different intermetallic phases given by EBSD.



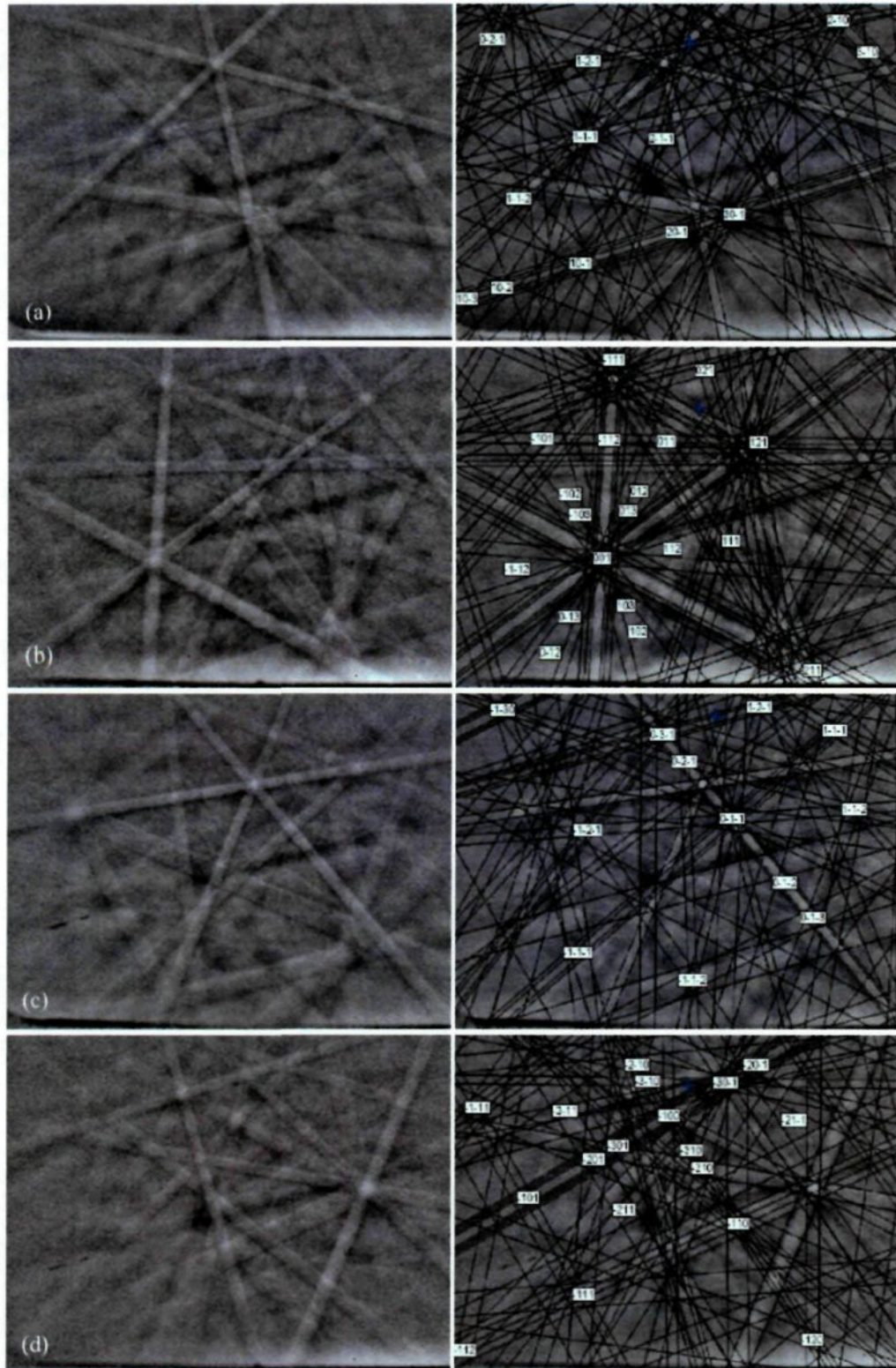


Figure 4.6: Four types of EBSD patterns and corresponding solutions. (a)  $\text{Al}_m\text{Fe}$ , (b)  $\text{Al}_7\text{Fe}_2\text{Si}$ , (c)  $\text{Al}_6\text{Fe}$ , (d)  $\text{Al}_3\text{Fe}$ .

#### 4.1.4 Phase quantification

5 samples with different distance from the casting surface were taken across the thickness of a commercial AA5657 DC cast ingot from Rio Tinto Alcan (as shown in Figure 4.7).

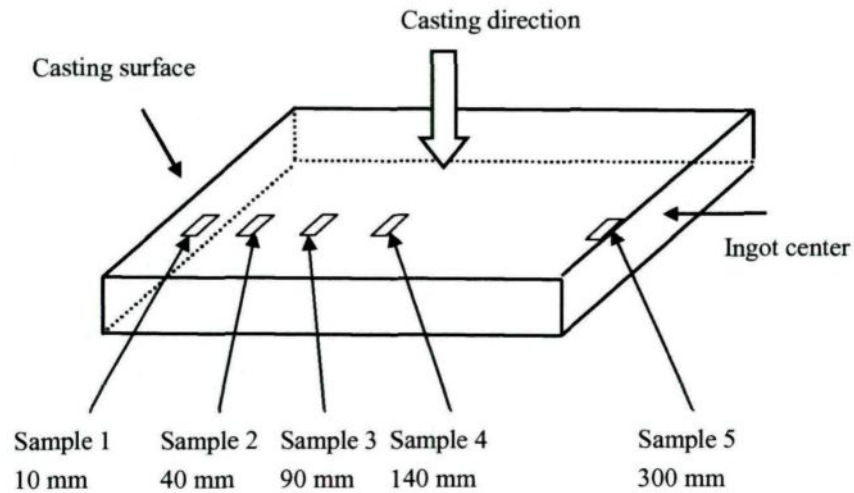


Figure 4.7 Schematic shows the sampling position in an AA5657 DC cast ingot.

The distribution of Fe phases in the ingot is shown in Figure 4.8.

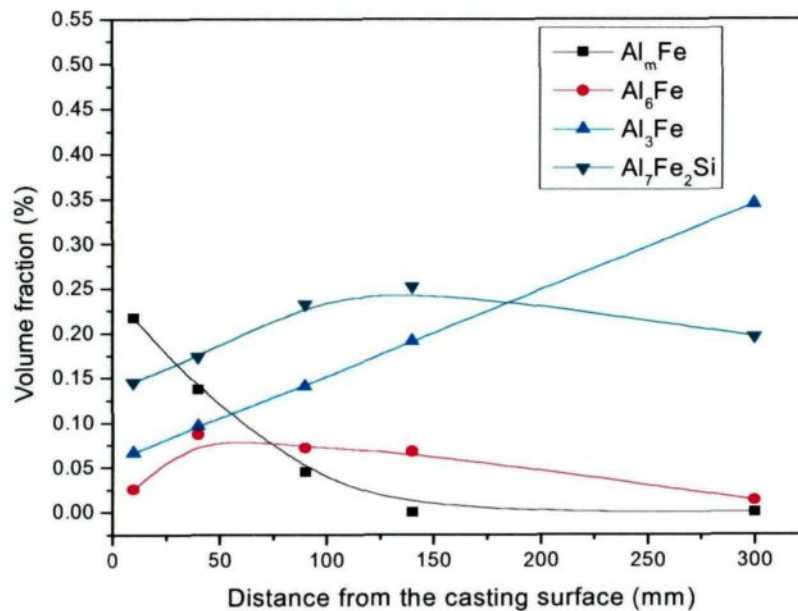


Figure 4.8: Fe intermetallic phases distribution AA5657 cast ingot.



As shown in Figure 4.8,  $\text{Al}_m\text{Fe}$  is a dominant phase in the position near the casting surface. It decreases with the increase of the distance away from the casting surface to the ingot center.  $\text{Al}_3\text{Fe}$  increase with the distance increase, approximately linear, and it becomes a dominant phase after the position of 140 mm away from the casting surface in the ingot. The  $\text{Al}_7\text{Fe}_2\text{Si}$  can be frequently seen from the casting surface to the ingot center. It increases from the casting surface up to 140 mm and then remains almost constant. A small amount of  $\text{Al}_6\text{Fe}$  was found in the surface and it increase at first and then decreases with the distance away from the casting surface to the center.

The distribution of each phase can be explained by the cooling rates change in the ingot. At the position 10 mm from the casting surface, because the secondary cooling in the DC casting process, it has quite high local cooling rate. Thus, the phase  $\text{Al}_m\text{Fe}$ , which has the highest undercooling forms. With the distance increase, the cooling rates gradually decrease due to longer thermal diffusion paths. In the ingot center, the cooling rates can be as low as less than 1 K/s, where forms preferentially the equilibrium phase  $\text{Al}_3\text{Fe}$ . As reported by X.-G. Chen<sup>12</sup>, the  $\text{Al}_7\text{Fe}_2\text{Si}$  phase becomes a major intermetallic phase at higher level of Si content. It is the first time in the present study to find that the hexagonal  $\text{Al}_7\text{Fe}_2\text{Si}$  phase is one of the dominant phase across the AA5657 DC cast ingot, which may be caused by the high amount of Mg content. Because the element Mg also has hexagonal crystal structure<sup>57</sup>, it is possible to promote the formation of hexagonal  $\text{Al}_7\text{Fe}_2\text{Si}$  particles. As found in the present study, there are no visible FTZs revealed in AA5657 DC cast ingot, which

maybe has some relationship with the  $\alpha$ -AlFeSi phase distribution. The phenomenon that increase of  $\alpha$ -AlFeSi phase can make the FTZs invisible was also found by S.J. Maggs et al<sup>13</sup> in the alloy with Fe/Si of 2.

By using the methods that has developed in the present research, the Fe intermetallic phases present in the industry DC cast AA5657 alloy ingot were characterized. The methods that have been used in this study solved the problem of quantification limit of the Fe phases, which can be quite useful in the future study of this field.

## 4.2 Phase characterization in an AA1050 DC cast ingot across the FTZs

A lot of research has been carried out to study the FTZs formation in 1xxx-series alloy ingots, and it is more or less clear that the formation of  $Al_mFe$  is the main factor of FTZ. However, all the results were given based on qualitative or semi-quantitative analysis. It is still not clear about the transition of Fe intermetallic phases across the FTZ. Thus, in order to better understand the Fe intermetallic phases in the ingot with visible FTZs, a slice of an industry DC cast AA1050 ingot from Rio Tinto Alcan was studied based on EBSD technique and EDS. Its chemical composition was analyzed and shown in Table 4.1:

Table 4.1 Chemical composition of an AA1050 DC cast ingot (wt.%).

Alloy	Elements									
	Fe	Si	V	Ni	Mg	Cu	Mn	Gr	Zn	Al
AA1050	0.26	0.04	0.015	0.034	0.001	0.003	0.003	0.002	0.002	BAL

For this DC cast AA1050 ingot, the FTZs were clearly revealed by using caustic soda (NaOH) etching method, as shown in Figure 4.9:

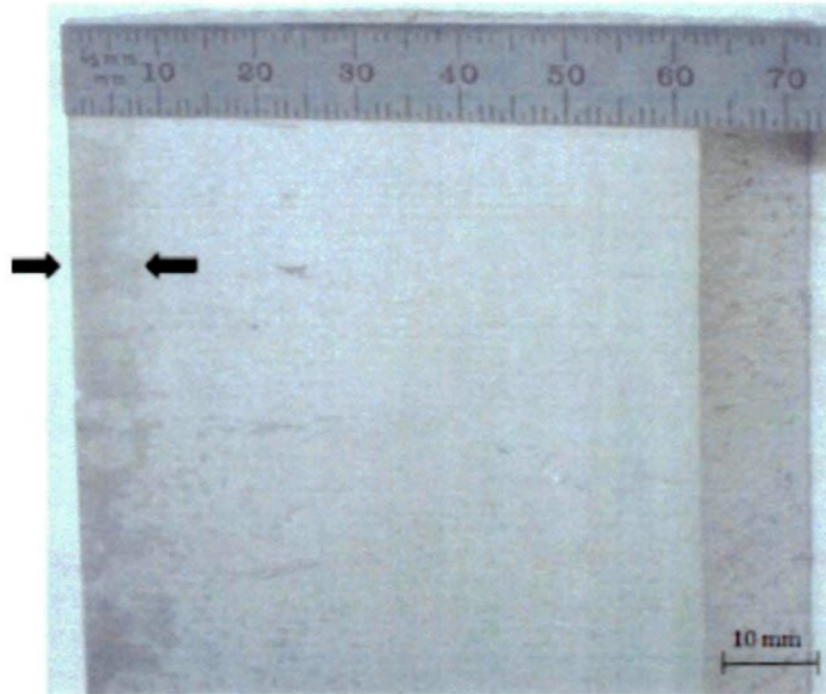


Figure 4.9: FTZ revealed in AA1050 alloy ingot. FTZ is shown between the 2 arrows. The thickness of FTZ is about 6~8mm. Etched in 15% NaOH heated at 60~70°C for 5 minutes.

In the present study, six positions are chosen across the FTZs, which are 3mm, 6mm, 9mm, 12mm, 18mm, and 24mm away from the ingot casting surface. Similarly with the phase characterization in AA5657 cast ingot, the Fe intermetallic phases appearing in the fields were identified by the combination of EBSD and EDS.

### 4.2.1 Ingot microstructure

Under the Optical Microscope, the microstructure appears obviously difference in and out of the FTZs (Figure 4.10). This difference is caused by the difference in Fe intermetallic phases content. Different type of Fe intermetallic phases have different response to a given etchant, which appear in macro observation as color difference between areas on the ingot surface.

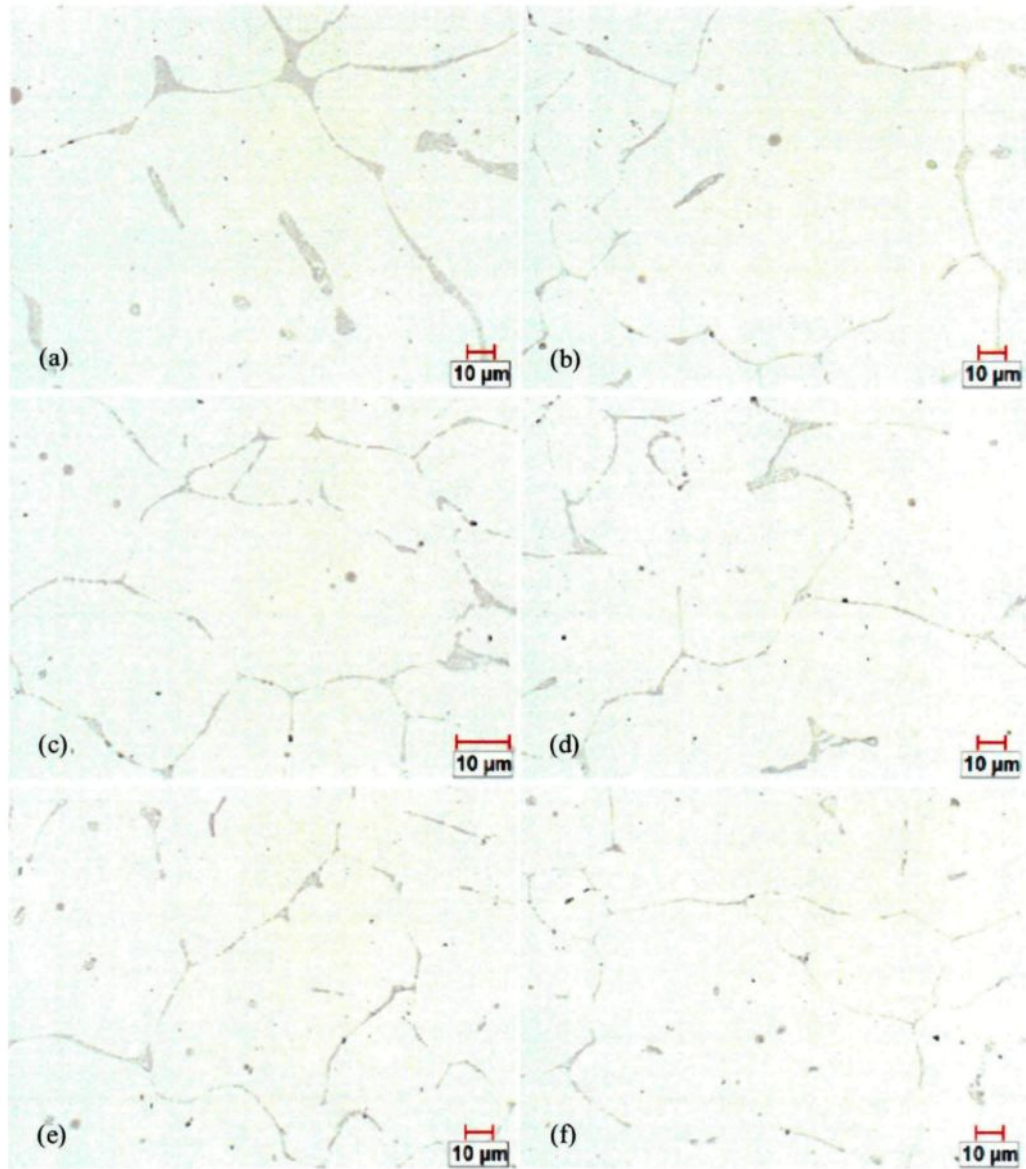


Figure 4.10: Microstructure of AA1050 ingot across the FTZs. (a) 3 mm, (b) 6 mm, (c) 9 mm, (d) 12 mm, (e) 18mm, (f) 24 mm.

#### 4.2.2 EDS and Deep-etching morphology

In the AA1050 ingot, the EDS results (Figure 4.11) of  $\text{Al}_m\text{Fe}$ ,  $\text{Al}_6\text{Fe}$ ,  $\alpha\text{-AlFeSi}$  and  $\text{Al}_3\text{Fe}$  phases appear similar with those in AA5657 alloy:  $\alpha\text{-AlFeSi}$  contains some Si and both  $\alpha\text{-AlFeSi}$  and  $\text{Al}_3\text{Fe}$  always has some Ni content.

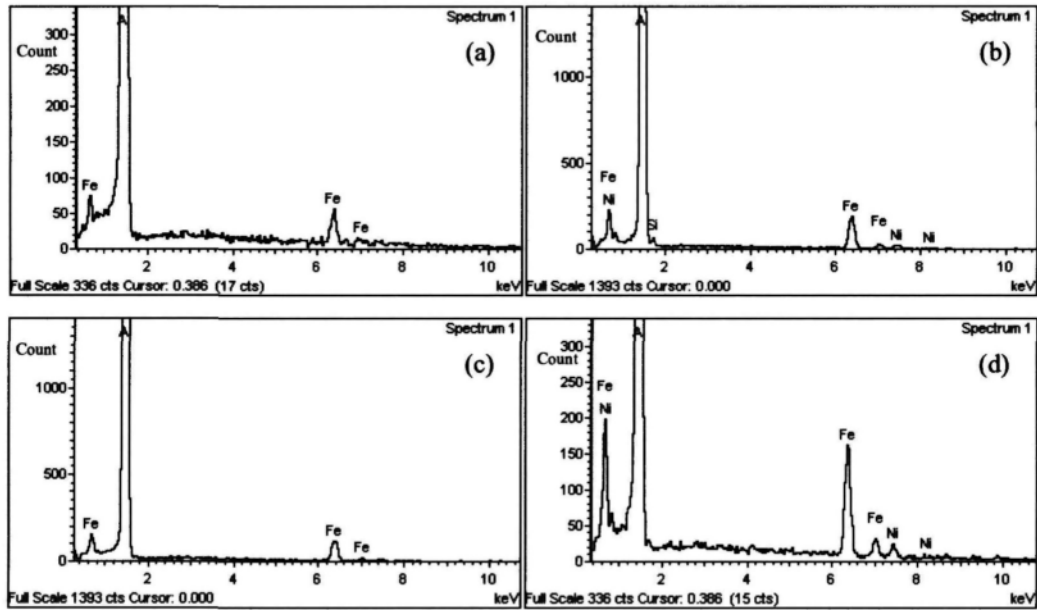


Figure 4.11: EDS results of Fe intermetallic phases in AA1050 ingot. (a)  $Al_mFe$ , (b)  $Al_7Fe_2Si$ , (c)  $Al_6Fe$ , (d)  $Al_3Fe$ .

Their morphologies of four types of Fe intermetallic phases after deep-etching are shown in Figure 4.12.

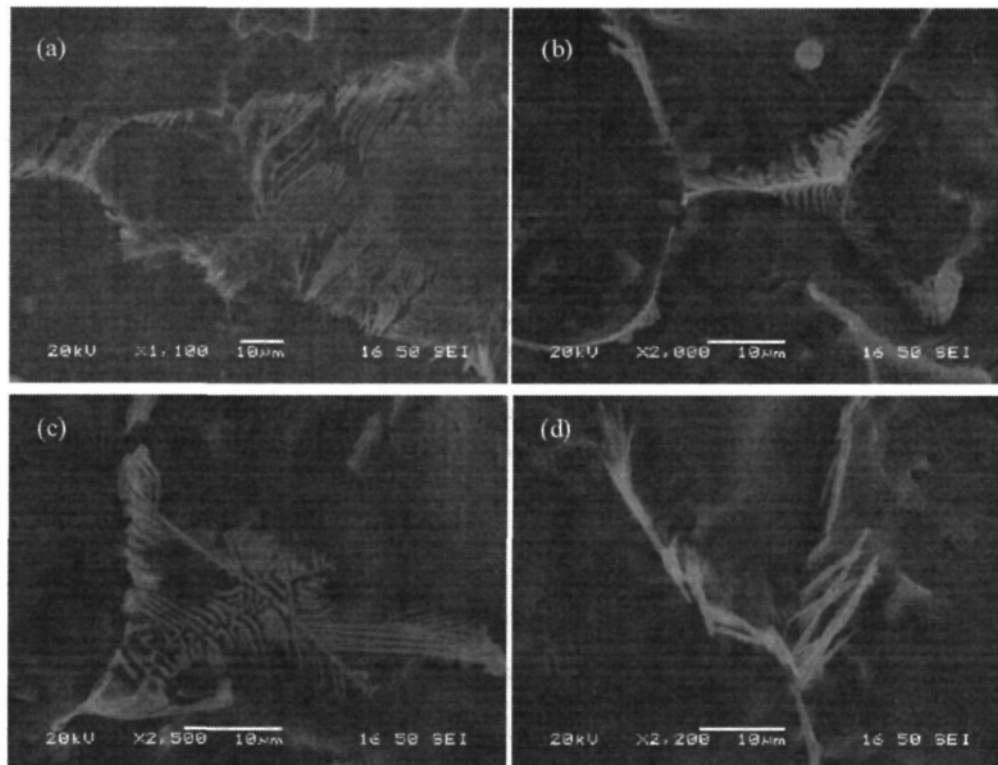


Figure 4.12: Morphologies of Fe intermetallic phases (Deep-etched). (a)  $Al_mFe$ , (b)  $Al_6Fe$ , (c)  $Al_7Fe_2Si$ , (d)  $Al_3Fe$ .

From Figure 4.12, we can find that the typical morphologies of Fe intermetallic phases in AA1050 alloy ingot appear quite similar with those in AA5657 alloy ingot:  $\text{Al}_m\text{Fe}$  has fine feathery like morphology,  $\text{Al}_6\text{Fe}$  grow into curved plate with swings,  $\alpha\text{-AlFeSi}$  has chinese-script morphology and  $\text{Al}_3\text{Fe}$  appears needle like morphology.

In addition to the four Fe intermetallic phases mentioned above, another Fe phase that containing high levels of Ni was also observed in this ingot. The morphology of this phase is quite unique (Figure 4.13).

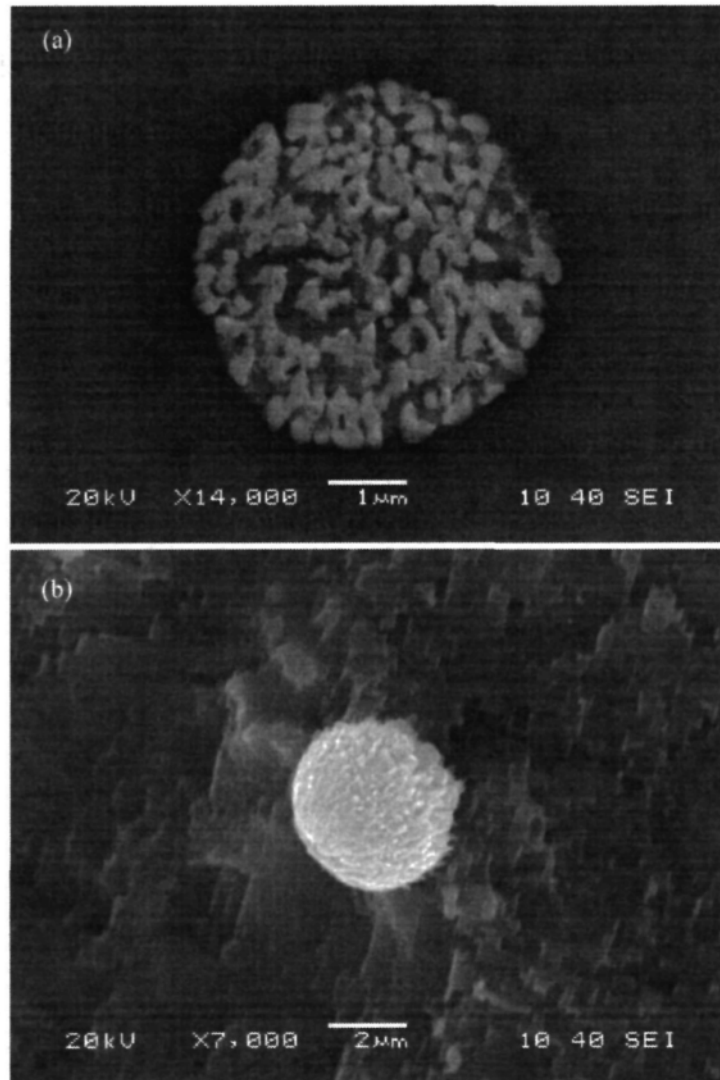


Figure 4.13: Morphology of Ni containing intermetallic phase under SEM in SEI mode. a) Before deep-etching, b) After deep-etching.

The Ni containing phase morphology often appears round particle with a diameter of about 2 ~ 3 $\mu\text{m}$ . The typical EDS spectra is shown in Figure 4.14, from statistic calculation we can get that the Fe/Ni ratio of this particle is about 7 (Table 4.2), while the Ni/Fe ratio of other types of Fe intermetallic particles  $\alpha\text{-AlFeSi}$  and  $\text{Al}_3\text{Fe}$  can be as low as 0.1%, which indicates that the Ni containing phase contains higher level of Ni.

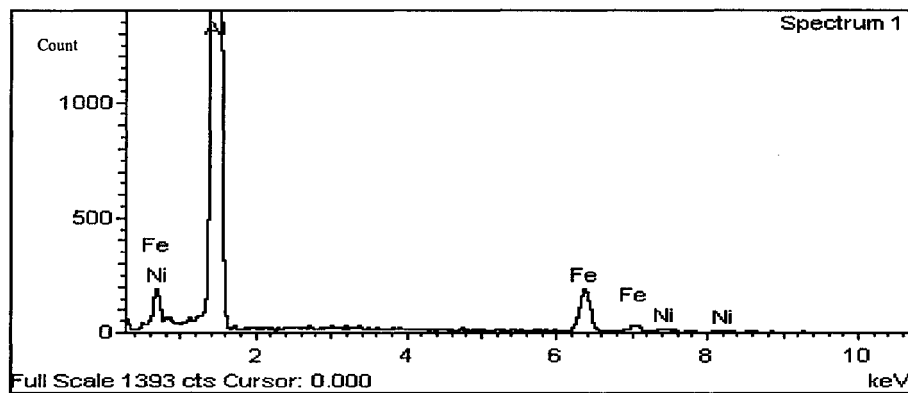


Figure 4.14: EDS results of a Ni containing particle.

Table 4.2: Chemical composition of Ni containing particles in 1xxx-series alloy ingot, atoms%

		Fe	Ni	Atoms ratio Fe/Ni	Average Fe/Ni
Particles	No. 1	5.43	0.78	6.96	6.87
	No. 2	3.43	0.52	6.59	
	No. 3	5.64	0.91	6.19	
	No. 4	5.34	0.82	6.51	
	No. 5	6.02	0.82	7.34	
	No. 6	6.05	0.84	7.20	
	No. 7	5.17	0.71	7.28	

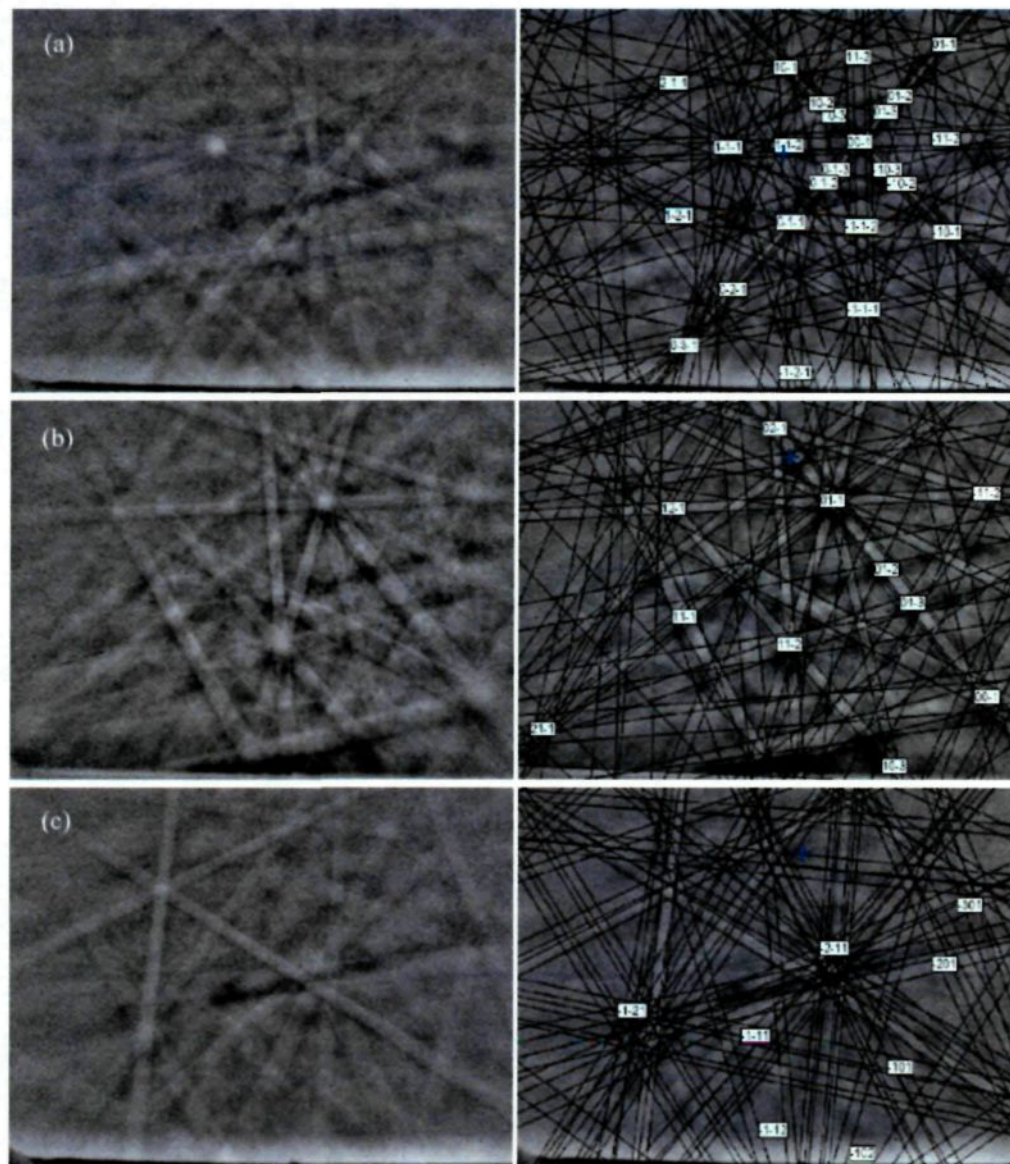
Since it cannot be matched with any known phase in ternary Al-Fe-Ni system, we denoted this Ni containing phase as  $\text{AlFeNi}$ . The formation of this intermetallic phase in this alloy ingot is caused by the high content of Ni (see Table 4.1). Similar with the Fe element, the solid solubility of nickel in aluminum is quite low, which is less than 0.04%, above this amount, it will present as an insoluble intermetallic phases,



usually in combination with iron.

### 4.2.3 Fe Phase characterization using EBSD technique

For the new Ni containing phase, it is very difficult to get good diffraction patterns, which was characterized based on its morphology and EDS results. The diffraction patterns and their corresponding solutions of four types of Fe intermetallic phases are shown in Figure 4.15:



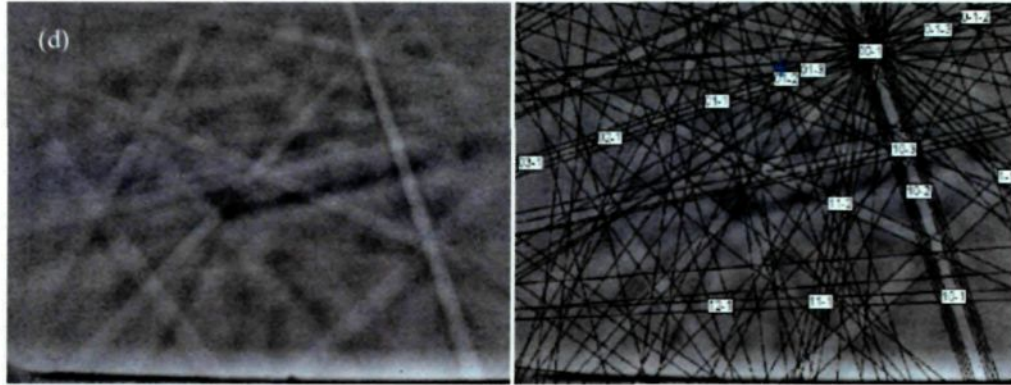


Figure 4.15: EBSD diffraction patterns and corresponding solutions of different type of Fe intermetallic phases in AA1050 alloy ingot, a)  $\text{Al}_m\text{Fe}$ , b)  $\text{Al}_6\text{Fe}$ , c)  $\text{Al}_7\text{Fe}_2\text{Si}$ , d)  $\text{Al}_3\text{Fe}$ .

#### 4.2.4 Phase quantification

The volume fraction of each phase was measured by using Image Analysis (Figure 4.16).

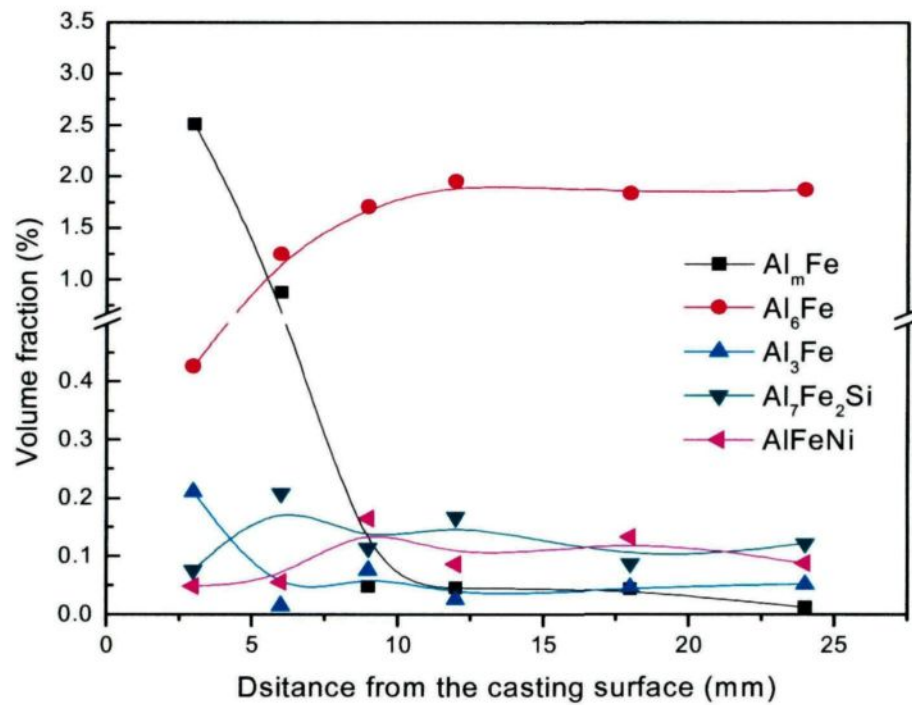


Figure 4.16: Fe intermetallic phase distribution across the FTZs in AA1050 alloy ingot.

From Figure 4.16, we can find that at the position 3 mm from the casting surface, the dominate phase is  $\text{Al}_m\text{Fe}$ , at the position 6 mm the dominate phases are  $\text{Al}_m\text{Fe}$  and

$\text{Al}_6\text{Fe}$ , while  $\text{Al}_6\text{Fe}$  become the predominant phase after 9 mm. Because  $\text{Al}_m\text{Fe}$  and  $\text{Al}_6\text{Fe}$  have different responses to a given etchant, the FTZs become visible after etching. Till now, it is quite clear that the transition from  $\text{Al}_m\text{Fe}$  to  $\text{Al}_6\text{Fe}$  is the main reason that causes the FTZ visible.

In addition to the transition of  $\text{Al}_m\text{Fe}$  and  $\text{Al}_6\text{Fe}$ , there also exist transitions of  $\text{Al}_3\text{Fe}$ ,  $\text{Al}_7\text{Fe}_2\text{Si}$  and  $\text{AlFeNi}$  phase. The amount of  $\text{Al}_3\text{Fe}$  was found decrease from the position 3 mm to 24 mm. The formation of  $\text{Al}_3\text{Fe}$  in 3 mm from the casting surface is caused by the air gap during DC casting process, due to the relative low cooling rates. The heat extraction in air gap region is slow and leads to the shell zone of the ingot reheating, or even re-melting partially from inside. Thus, the local cooling rates in air gap region can be slow enough due to form the equilibrium phase  $\text{Al}_3\text{Fe}$ . This 1xxx alloy ingot has very low Si containing (0.04 wt %), so the ternary phase  $\text{Al}_7\text{Fe}_2\text{Si}$  only appears in the trace level and most of it was found at the position 6mm and 9 mm. For the  $\text{AlFeNi}$  phase, it was found the most at the position 9 mm, it is great possible that the formation of  $\text{AlFeNi}$  is affect by the local cooling rates.

In general, the transition of Fe intermetallic phases across the FTZs was made quite clear in the present study, there is no doubt that the formation of FTZs is caused mainly by the phase transition between  $\text{Al}_m\text{Fe}$  and  $\text{Al}_6\text{Fe}$ .

## 4.3 DC simulator and Fe intermetallic phases in DC simulator cast AA5657 ingots

### 4.3.1 DC simulator

Using the DC cast simulator apparatus, AA5657 alloy ingots with different Ni and V levels were cast, the cast ingots are shown in Figure 4.17:

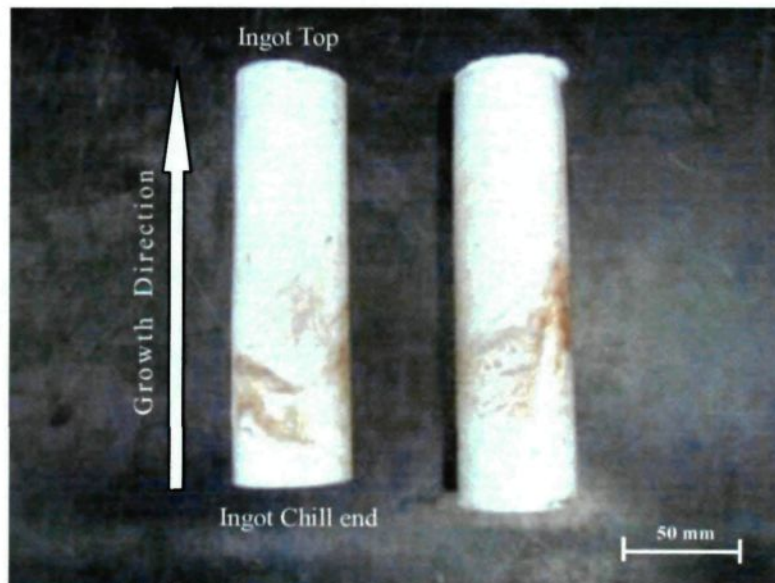


Figure 4.17: DC simulator casting ingots in the lab.

The dimension of the DC cast simulator Al ingots is about 38 mm in diameter and 150 mm in length. In the solidification process, cooling curves (Figure 4.18) were obtained from the thermocouples T1 ~ T5, which were located in the center of the DC cast mould. The position of the thermocouples from T1 to T5 were 20 mm, 45 mm, 70 mm, 95 mm and 120 mm away from the chill end.



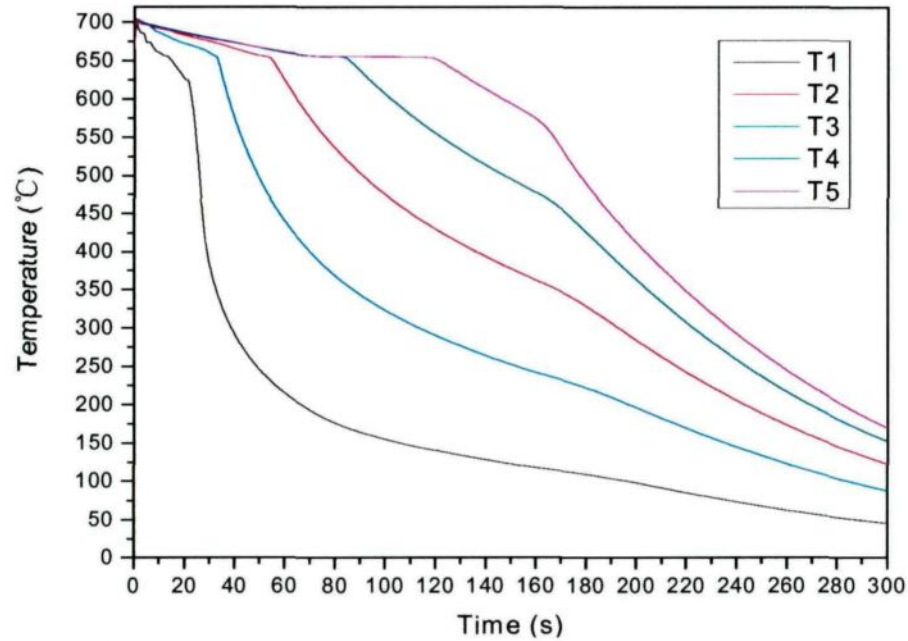


Figure 4.18: Cooling curves got from DC simulator casting AA5657 alloy.

From the cooling datas, the average cooling rates VS Distance were calculated and shown in Figure 4.19:

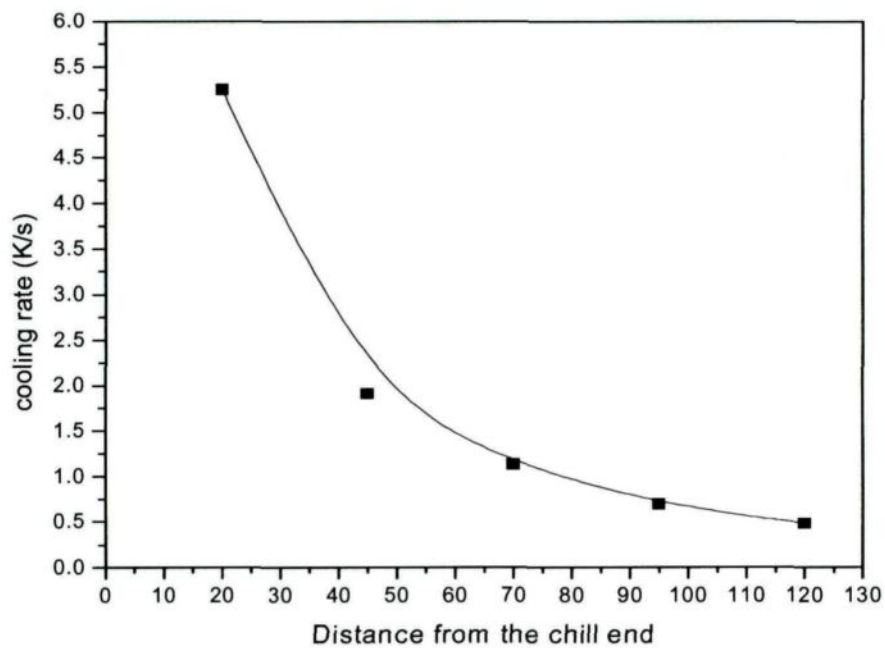


Figure 4.19: The average cooling rates in different position of the ingot from 700°C to 650°C.

From Figure 4.19 we can see that at the position of 20 mm from the chill end, the

cooling rate is about  $5.6^{\circ}\text{C/s}$ , while at the position of 120 mm, the cooling rate is as low as  $0.5^{\circ}\text{C/s}$ . The average cooling rates suggest that the cooling rate decrease greatly from the position near the chill end to the top of the DC simulator cast ingots, which provide different solidification conditions for the formation of Fe intermetallic phases to form.

A thermal analysis was carried out to study the solidification behavior of AA5657 alloy (see chapter 3.2). During the solidification process, the eutectic reaction of different Fe intermetallic phases cause heat release and cause local temperature gradient change, which may be reflected as peaks on the first derivation curve. Figure 4.20 shows a cooling curve and first derivation obtained by a thermocouple from the base AA5657 alloy cooled at  $1.28^{\circ}\text{C/s}$ . The peaks on the first derivation is great possible to be caused by the reaction of  $\alpha\text{-Al}$ ,  $\text{Al}_3\text{Fe}$ ,  $\text{Al}_6\text{Fe}$ ,  $\text{Al}_m\text{Fe}$  and  $\alpha\text{-AlFeSi}$  according to their eutectic temperature ( $650^{\circ}\text{C}\sim 610^{\circ}\text{C}$ )<sup>5, 59</sup>.

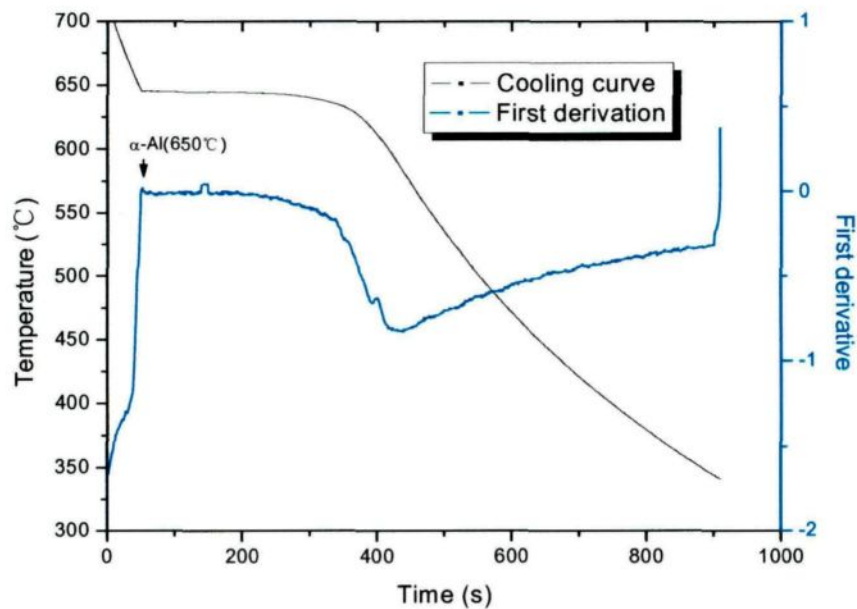


Figure 4.20: Cooling curve and first derivation obtained from the AA5657 alloy cooled at  $1.28^{\circ}\text{C/s}$ .

### 4.3.2 Fe intermetallic phases in the base material of DC simulator cast AA5657 ingots (A01 alloy in Table 3.2)

In order to characterize the Fe intermetallic phases content in A01 alloy, four samples with a distance of 20 mm, 40 mm, 60 mm and 100 mm from the chill end were taken from ingot A01.

#### 4.3.2.1 Ingot microstructure

The ingot microstructures of different positions are shown in Figure 4.21:

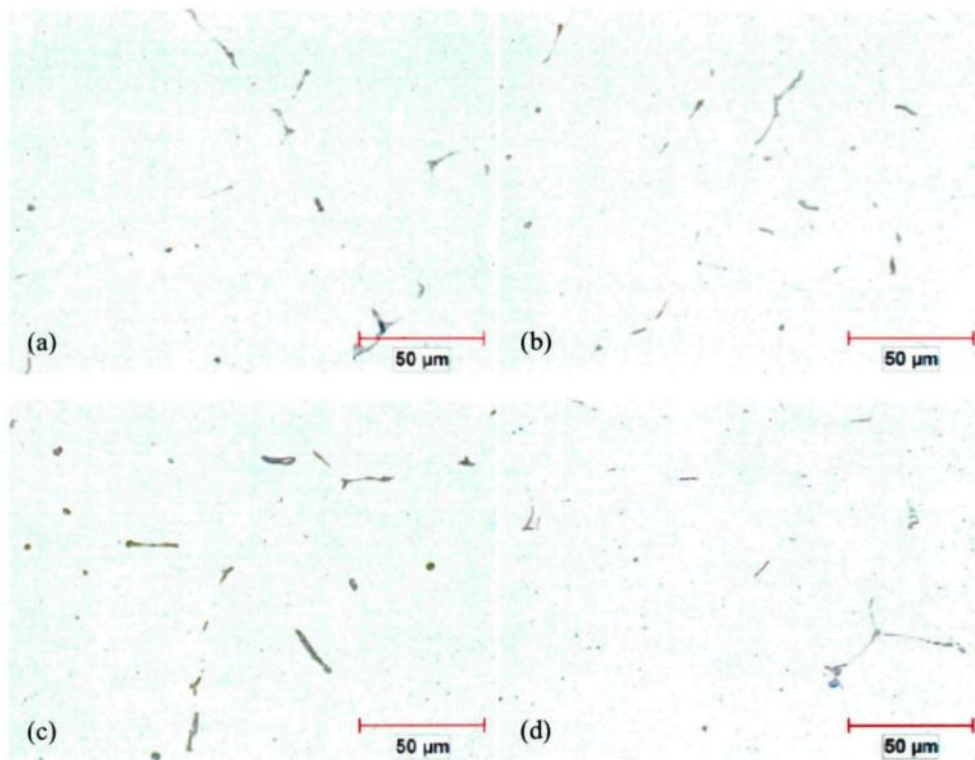


Figure 4.21: Microstructure of DC simulator casting AA5657 alloy taken from (a) 20 mm, (b) 40 mm, (c) 60 mm, (d) 100 mm from the chill end.

We can see from Figure 4.21 that the microstructure of DC simulator cast AA5657 alloy in different position has no major difference. As the Fe intermetallic

phases characteristics are similar to those in industry ingots, The Fe particles were firstly characterized by using Optical Microscope, Deep-etching method, and EDS technique. Four types of Fe intermetallic phases were found in A01 alloy ingot, the typical morphology and their corresponding EDS spectra are shown in Figures 4.22 - 4.24:

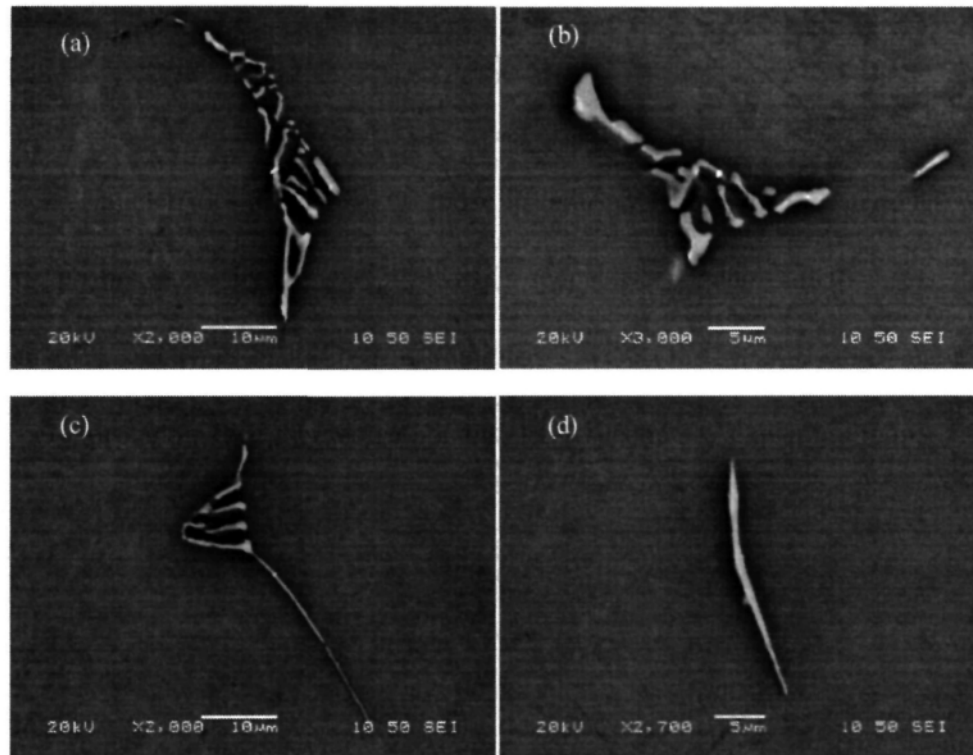


Figure 4.22: Fe intermetallic phases morphology under SEM. (a) fine feathery like, (b) Chinese script, (c) curved plates with wings, (d) needle like.

As mentioned before, the 2-D morphology of  $Al_mFe$ ,  $\alpha-AlFeSi$  and  $Al_6Fe$  mostly has the shape of interdendritic channels, and it is difficult to distinguish them from each other (Figure 4.22). The 3-D morphology revealed by using deep-etching method is more helpful for the four types of Fe intermetallic phases identification (Figure 4.23).



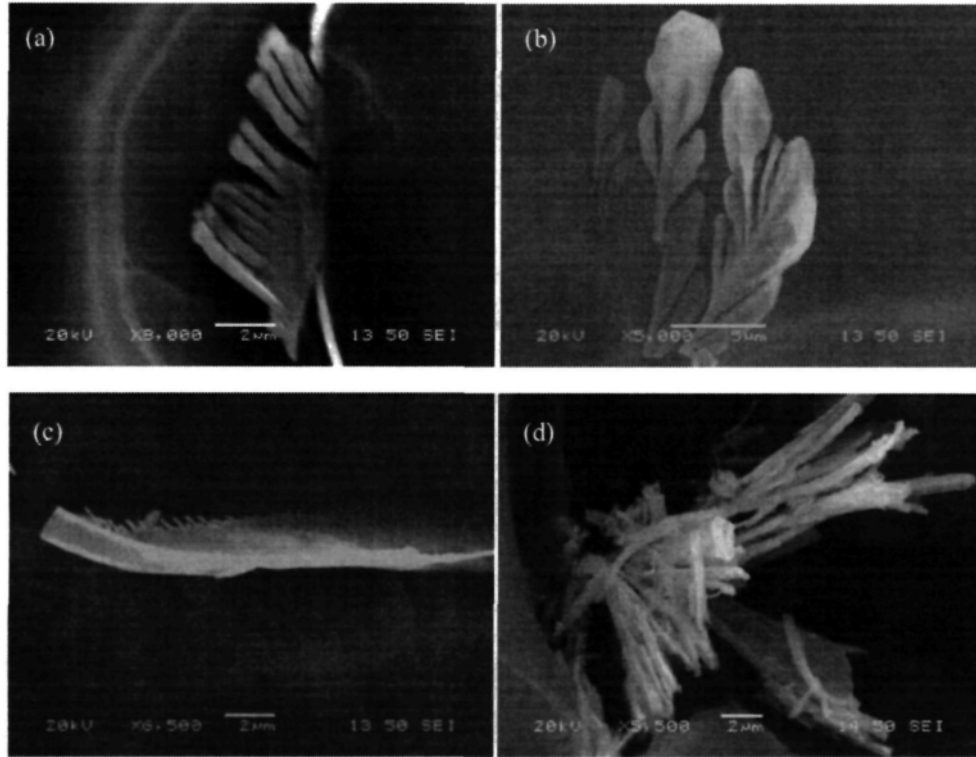


Figure 4.23: Fe intermetallic phases morphology under SEM (Deep-etching). (a) fine feathery like, (b) Chinese script, (c) curved plates, (d) needle like.

The EDS results of different phases are shown in Figure 4.24:

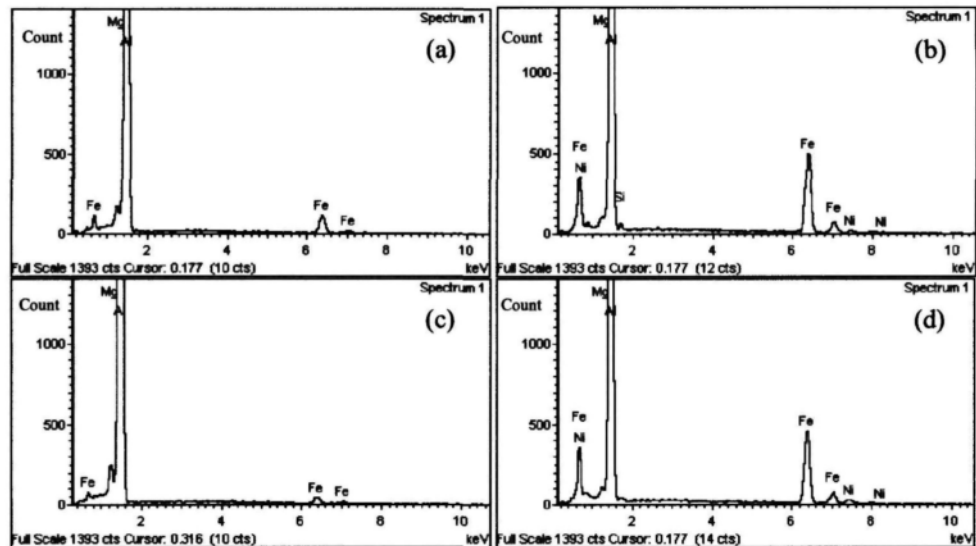


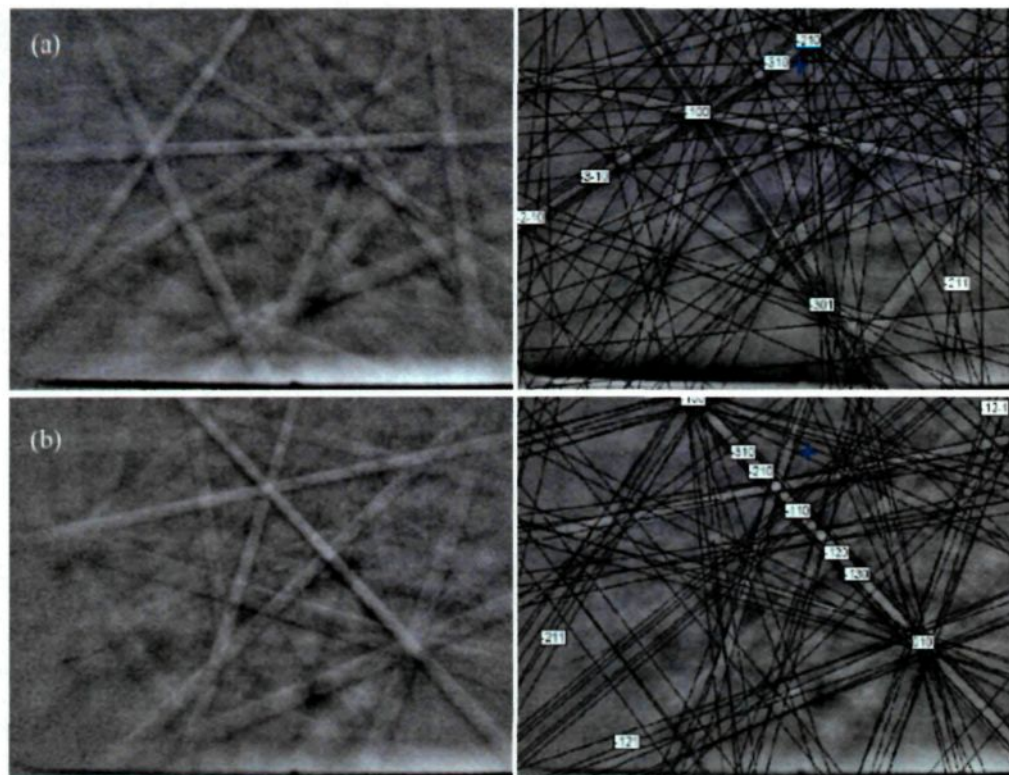
Figure 4.24: Typical EDS results of Fe intermetallic phases in A01. (a) Fine feathery like, (b) Chinese script, (c) curved plates, (d) needle like.

The EDS results of the Fe intermetallic particles with Chinese script and needle

like morphology show some amount of Ni content, which is similar with those in industry DC cast AA5657 alloy ingot (see chapter 4.1).

#### 4.3.2.2 EBSD diffraction patterns

Using EBSD technique, we found the similar results as those in industry DC cast AA5657 ingot: the four types of Fe intermetallic phases appearing in A01 ingot were identified as  $\text{Al}_m\text{Fe}$ ,  $\text{Al}_7\text{Fe}_2\text{Si}$ ,  $\text{Al}_6\text{Fe}$  and  $\text{Al}_3\text{Fe}$ . The following images show the diffraction patterns and their corresponding solutions of different intermetallic obtained by EBSD.



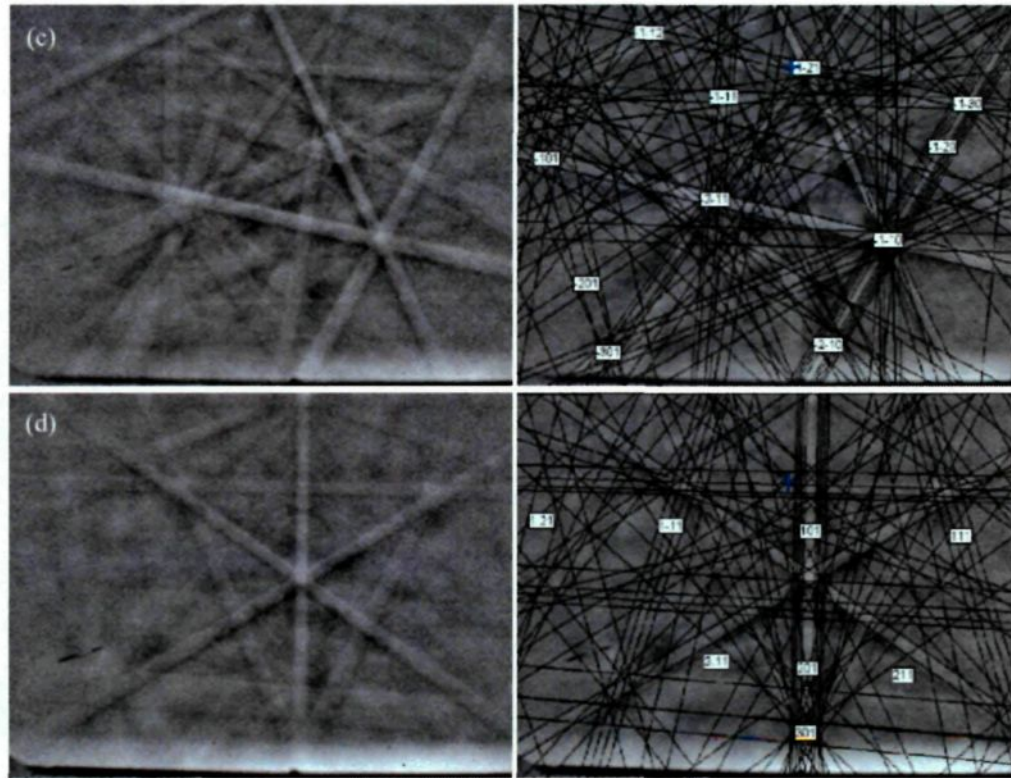


Figure 4.25:EBSD diffraction patterns and corresponding solutions of different type of Fe intermetallic phases in A01 alloy ingot, a)  $Al_mFe$ , b)  $Al_6Fe$ , c)  $Al_7Fe_2Si$ , d)  $Al_3Fe$ .

#### 4.3.2.3 Image analysis results

By using the Clemex Image analysis software, the Area Percentage (Volume fraction) and other parameters (perimeter, count, density) of Fe intermetallic phases were measured and analyzed.

The distribution of Fe phases in A01 alloy is used to make comparison with all Ni and V added alloys, it is very important for the accuracy of the results. Thus, we made a verification of the results by characterizing other 10 fields in the position of 20 mm, 30 mm, 40 mm, 50 mm, 60mm, 80 mm, and 100 mm in A01 alloy. The combined distribution results of the Fe intermetallic phases are shown in Figure 4.26:

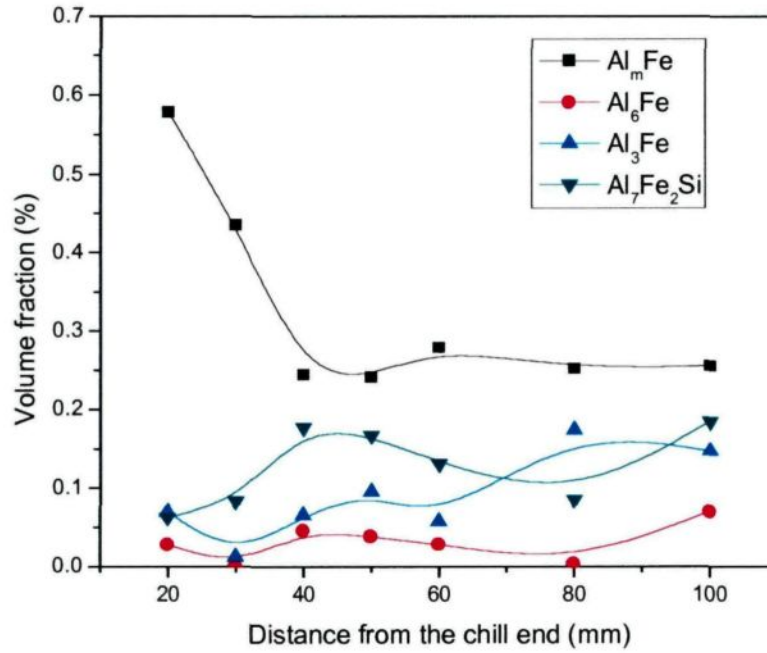


Figure 4.26: Fe intermetallic phase distribution in ingot A01.

As shown above, the volume fraction of  $Al_mFe$  decrease as the distances increase from the chill end; The  $Al_7Fe_2Si$  phase increase a little from position 20 mm to 40 mm, but from 40 mm to 80 mm, it decrease as the distance from the chill end increase, and it increase after 60 mm. For  $Al_3Fe$ , its volume fraction has a tendency to increase as the distance increase from the chill end. While for  $Al_6Fe$ , it was found only in trace level in the ingot. When compared the results with industry DC cast AA5657 ingot (See Figure 4.8), we can find that the biggest difference is that the relative amount of  $Al_7Fe_2Si$ ,  $Al_3Fe$  and  $Al_6Fe$  phases are lower than the industry ingot. Although difference is exist, we can still found that the Fe intermetallic phase distribution in DC simulator cast ingot is similar with that within 100 mm from the casting surface in the commercial DC casting ingot. Thus, the lab DC simulator cast ingot can reproduce the solidification conditions of the industry DC casting ingot in the sub-surface region.

The distribution of total phases is shown in Figure 4.27:



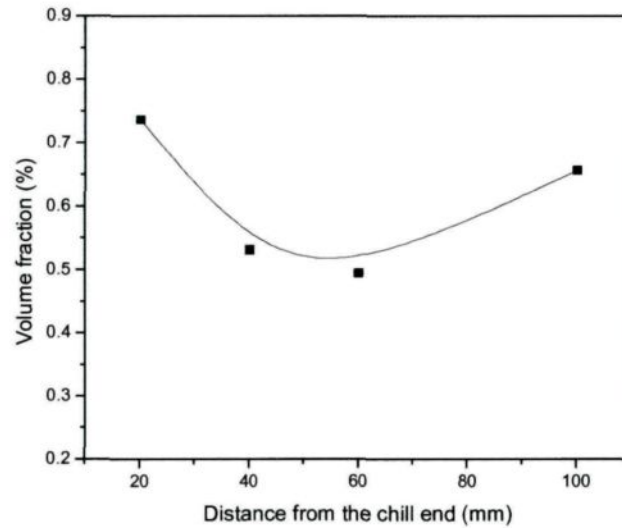


Figure 4.27: Distribution of total phase volume fraction in the ingot A01.

From Figure 4.27 we can find that the total volume fraction of Fe intermetallic phase in the position 20 mm from the chill end is a little higher than that in the other three positions, which is caused by the segregation during solidification process. The reason why the total volume fraction is high in the poaition of 100 mm is not clear.

The particle number in per unit area is defined as particle density of each Fe intermetallic phases, and it is shown in Figure 4.28:

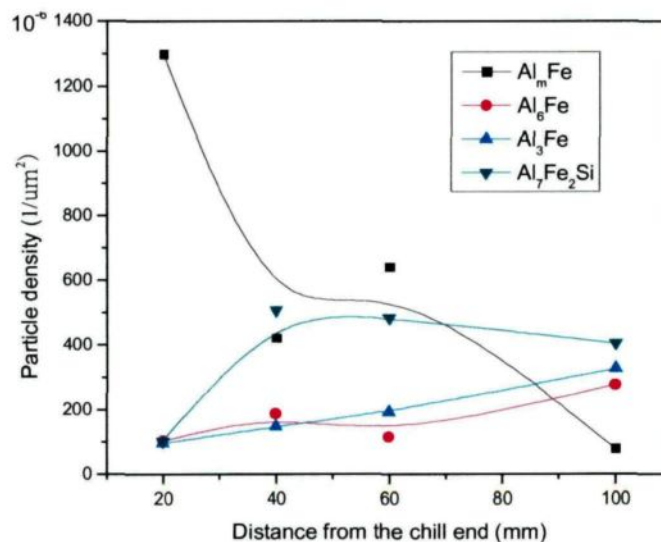


Figure 4.28: Particle density of each phase in A01 ingot.

The surface area of each particle has a liner relationship with perimeter, and has the following equation<sup>58</sup>:

$$S_v = 4L_A/\pi$$

Where  $S_v$  is surface area of the total particles per unit volume and  $L_A$  is popular average value of the total perimeter of particle per unit area. The surface area of each Fe intermetallic phases is shown in Figure 4.29:

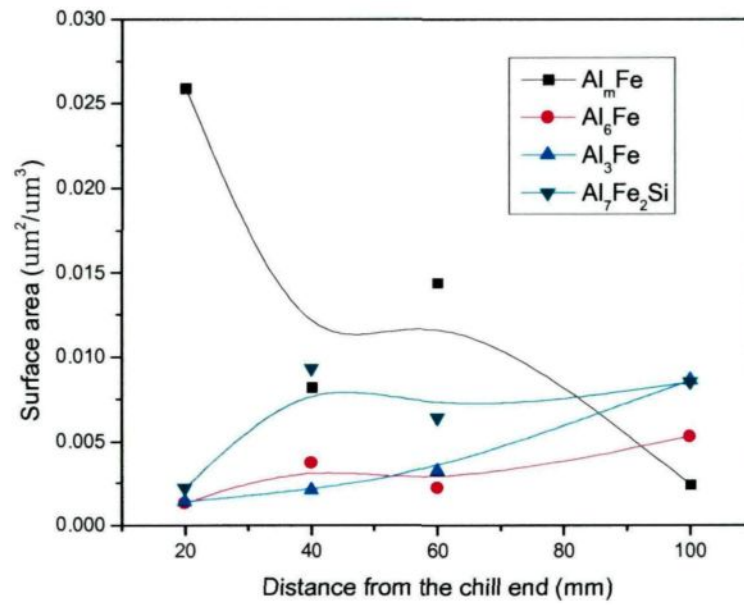


Figure 4.29: Surface area of each phase in A01 ingot.

When we compare Figure 4.28 and Figure 4.29 with Figure 4.27, we can find that the particle density and surface area of Fe phases have similar distribution tendency with the volume fraction, which means the particle number and surface area of Fe intermetallic phases have direct proportion to the volume fraction.

## 4.4 Effect of Ni on Fe intermetallic phases in DC simulator cast AA5657 ingots

For AA5657 alloy, which is an aluminium-magnesium based alloy, Ni is present as an impurity. It can not only cause accelerated corrosion, but also it has some effect on Fe intermetallic phases selection and give unwanted variation in anodizing response. In the recent years, the level of Ni content in the raw material and final products of Al is increasing. The continue trend of rising Ni may cause Al products not meet the specification. The present study is focused on the effect of Ni on Fe intermetallic phases selection in AA5657 alloy ingots produced by Lab DC simulator. Experimental alloys A05~A08 (Table 3.2), with different level of Ni content were casted and studied.

### 4.4.1 Ingots Microstructure

In the samples of ingots after Ni addition, high concentration of Ni was found in the interdendritic region of the ingots after Ni addition (Figure 4.30), which indicates that the addition of Ni was ejected to the rest liquid during the last stage of solidification.

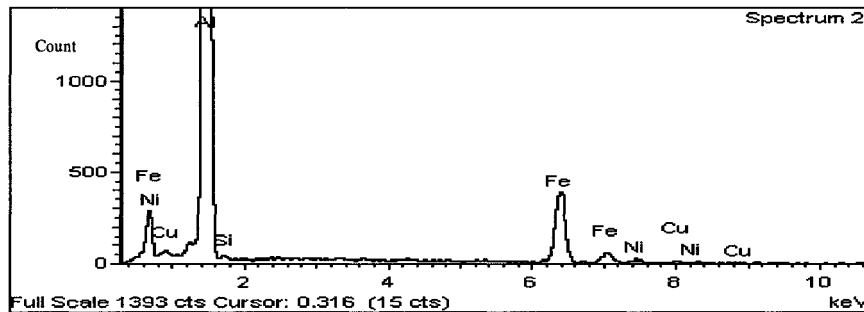


Figure 4.30: EDS shows the high content of Ni in the grain boundary after the addition of Ni in A10 ingot.

The enrichment of Ni in the interdendritic region may change the profile of the remaining liquid, which affect the nucleation and growth behavior of Fe intermetallic particles.

Figure 4.31 shows the Ingot microstructure of A05 (150 ppm Ni) to A08 (570 ppm Ni) with a same distance from the chill end.

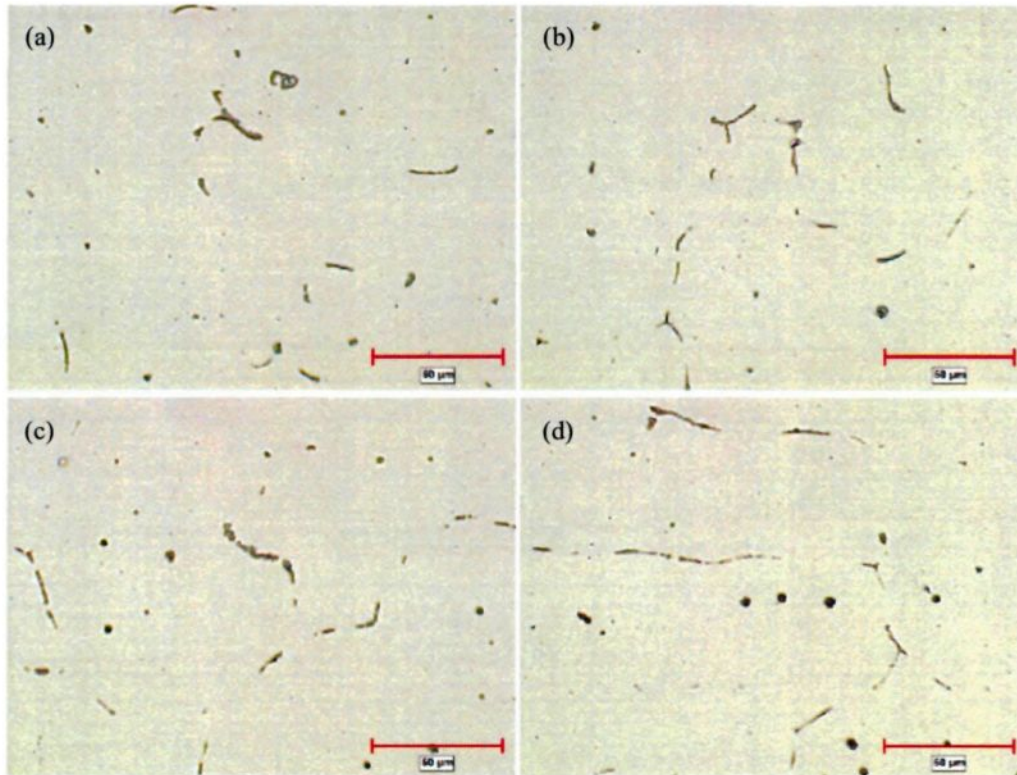


Figure 4.31: Photo microstructure taken from different Ni containing ingots with a distance of 40 mm from the chill ends. a) 150 ppm Ni, b) 240 ppm Ni, c) 390 ppm Ni, d) 570 ppm Ni.

It was found that low levels of Ni has no major effect on the ingots microstructure (Figure 4.31 (a) and (b)), while in the ingot with high Ni level over 390 ppm, some round particles seem appear and makes the microstructure different from others (Figure 4.31 (c) and (d)).

The Fe intermetallic phases under SEM in A08 alloy and their corresponding EDS spectra are shown in Figure 4.32 and Figure 4.33:



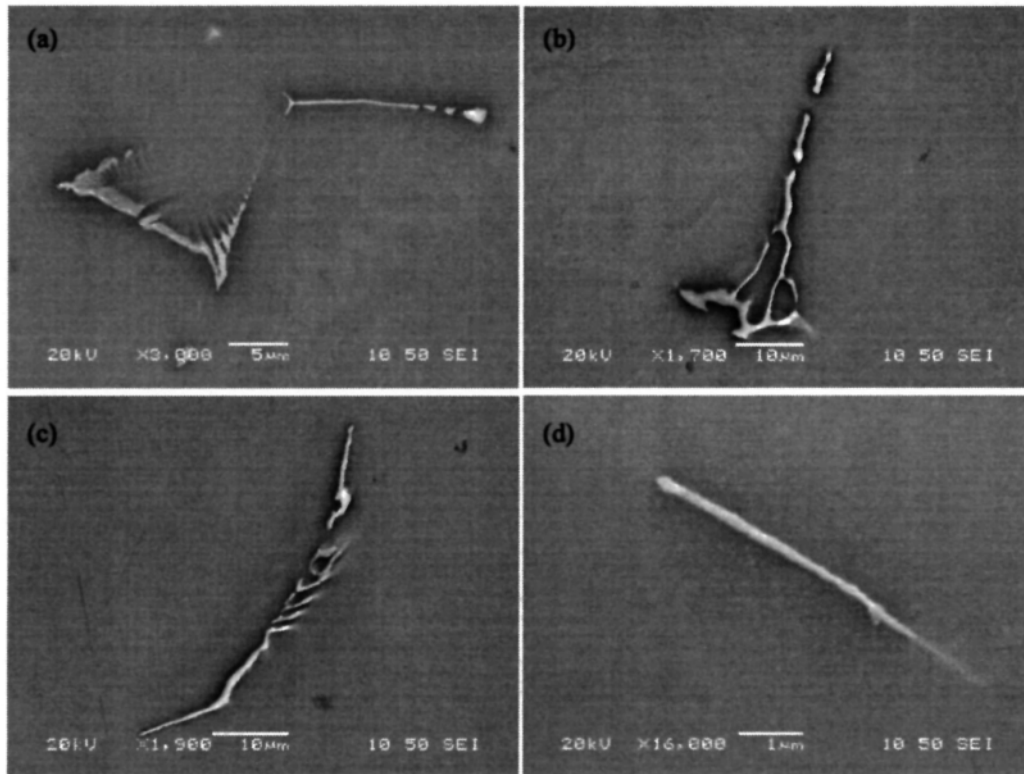


Figure 4.32: Fe intermetallic phases morphology under SEM in A08 alloy. (a) fine feathery like, (b) Chinese script, (c) curved plates with wings, (d) needle like.

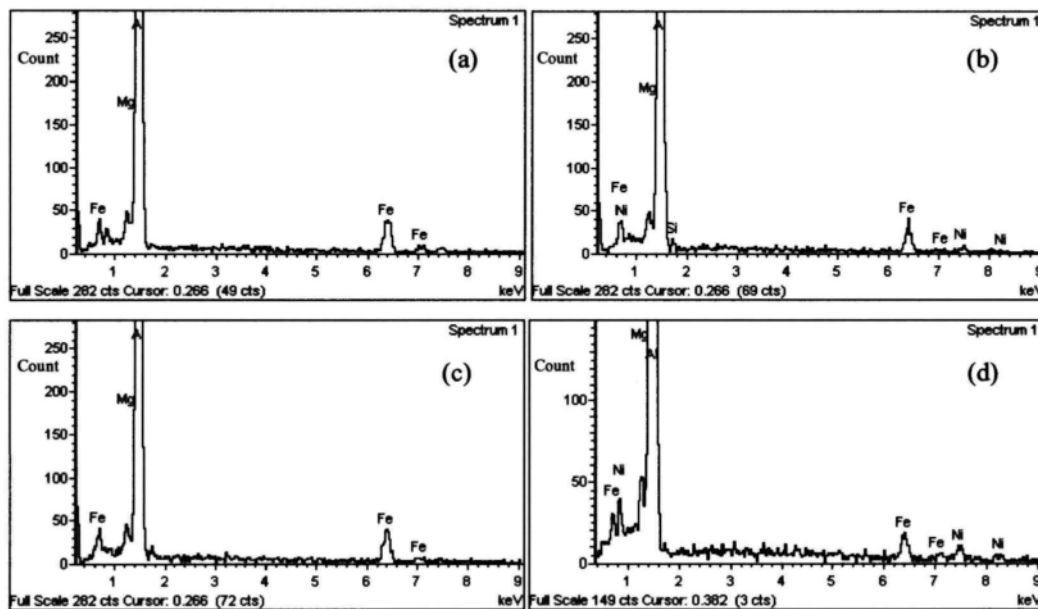


Figure 4.33: EDS spectra of Fe intermetallic particles in A08 alloy. (a) fine feathery like, (b) Chinese script, (c) curved plates with wings, (d) needle like.

In the ingot A07 and A08, some  $\text{AlFeNi}$  particles were observed frequently.

Figure 4.34 and Figure 4.35 shows the typical morphology and the EDS spectra of AlFeNi phase observed in an ingot with 570 ppm Ni content.

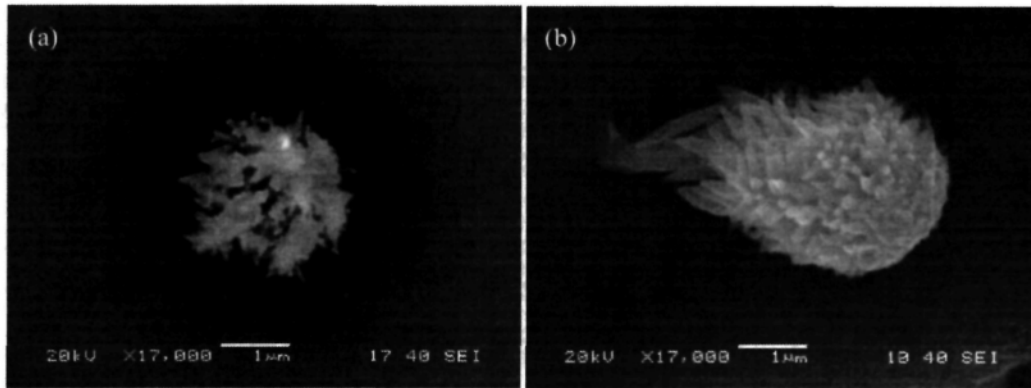


Figure 4.34: Typical morphology of AlFeNi in a DC simulator casting ingot under SEM. (a) Before Deep-etching, (b) After deep-etching.

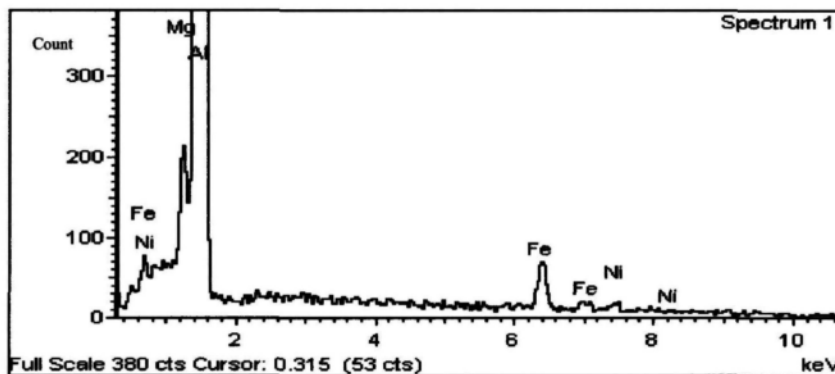


Figure 4.35: EDS spectra of AlFeNi in a DC simulator casting A08 ingot.

When refer to the findings of the AlFeNi particles in industry AA1050 alloy ingot, we can find that the AlFeNi particles in the lab DC simulator casting alloy ingots have similar characteristic with those observed in the AA1050 alloy ingot. Moreover, in some particles of Ni containing phases, white spots were frequently observed (Figure 4.36). The EDS results show that the ratio of Ni/Fe on the spots is about 3:2, which are much higher than other area of the particle (Figure 4.35). This phenomenon indicates that the high content of Ni is possible to be the cause of the white spots formation, which in turn promotes the formation of Ni containing phases.

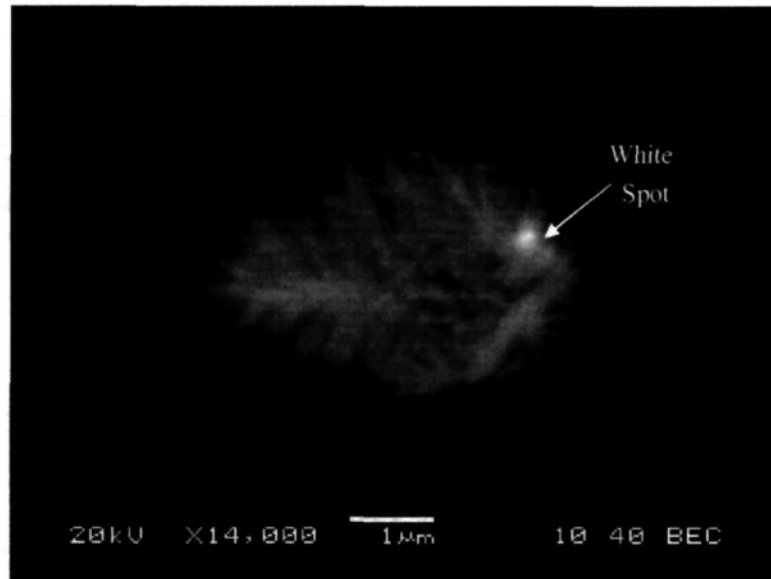


Figure 4.36: An AlFeNi particle under the SEM BEC mode, a white spot is clearly observed.

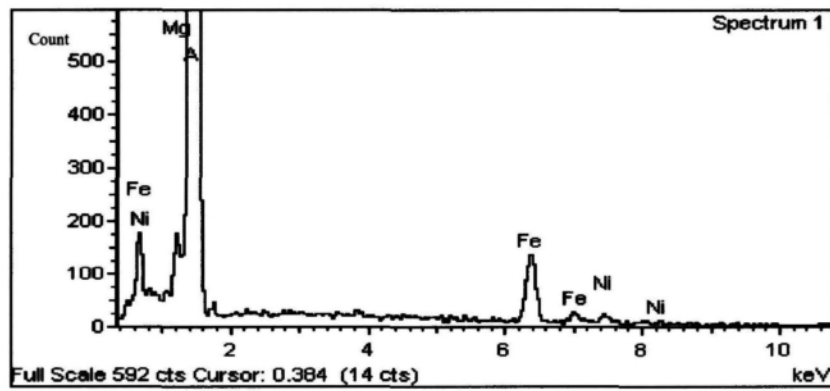


Figure 4.37: EDS shows high Ni content in the white spot of a AlFeNi particle.

The distribution of AlFeNi indicates the AlFeNi phase formation is affected by the cooling rates (Figure 4.38).

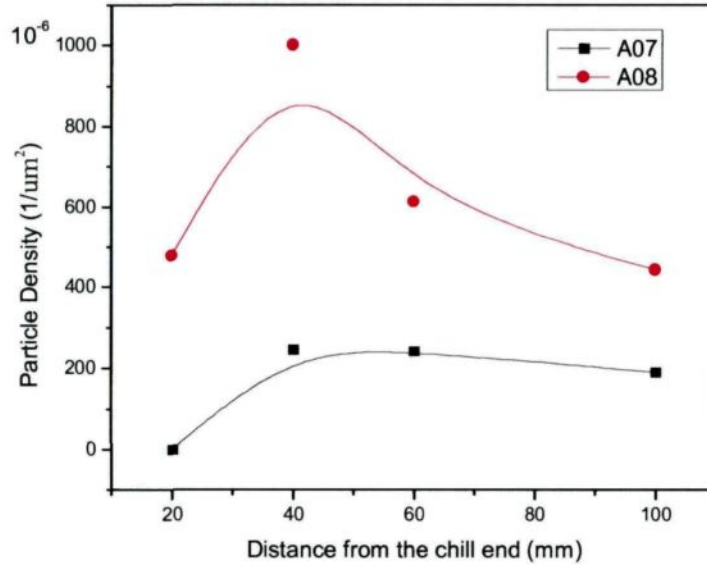


Figure 4.38: Distribution of AlFeNi particle density in A07, A08 alloy ingots.

As we can find, at the position 40 mm and 60 mm from the chill ends, the AlFeNi particle density appears the most. When refer to the average cooling rates in Figure 4.19, we can see the AlFeNi phase forms the most at the position with medium cooling rates.

#### 4.4.2 EBSD patterns

Because of the smaller size of AlFeNi particles, it is impossible to get diffraction patterns based on the methods used in present study. Thus, the new Ni-containing phase was identified according their morphology and the EDS results. EBSD diffraction patterns of the four conventional phases were found similar with those in commercial AA5657 cast ingot, which were identified as  $Al_mFe$ ,  $Al_7Fe_2Si$ ,  $Al_6Fe$  and  $Al_3Fe$ . The following images show the diffraction patterns and their corresponding solutions of different intermetallic in A08 alloy got by EBSD. It was found that the feathery like morphology particles are mostly  $Al_mFe$ , chinese script particles are

mostly  $\text{Al}_7\text{Fe}_2\text{Si}$ , curved plate particles are mostly  $\text{Al}_6\text{Fe}$  while needle like particles are mostly  $\text{Al}_3\text{Fe}$ .

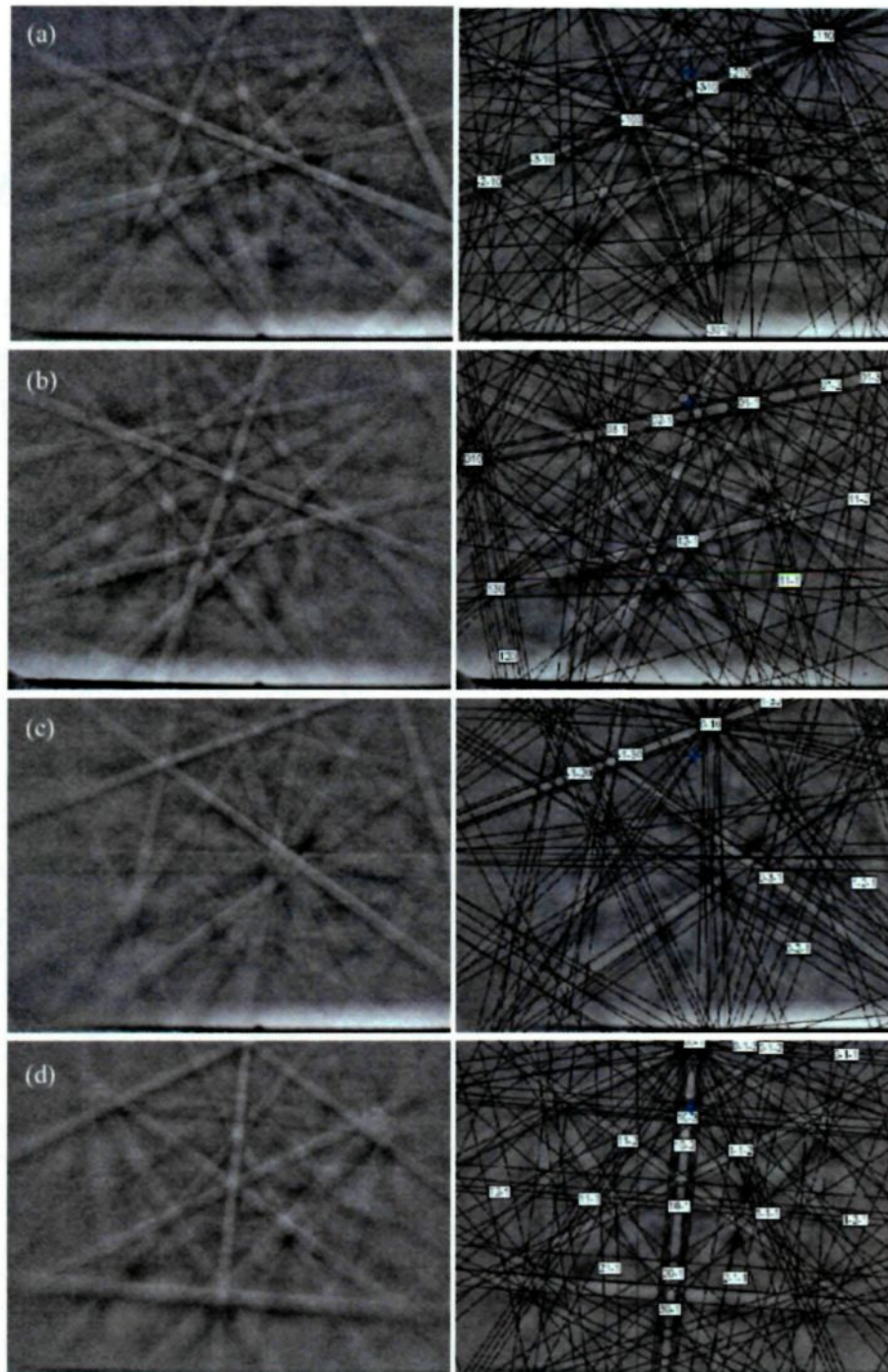
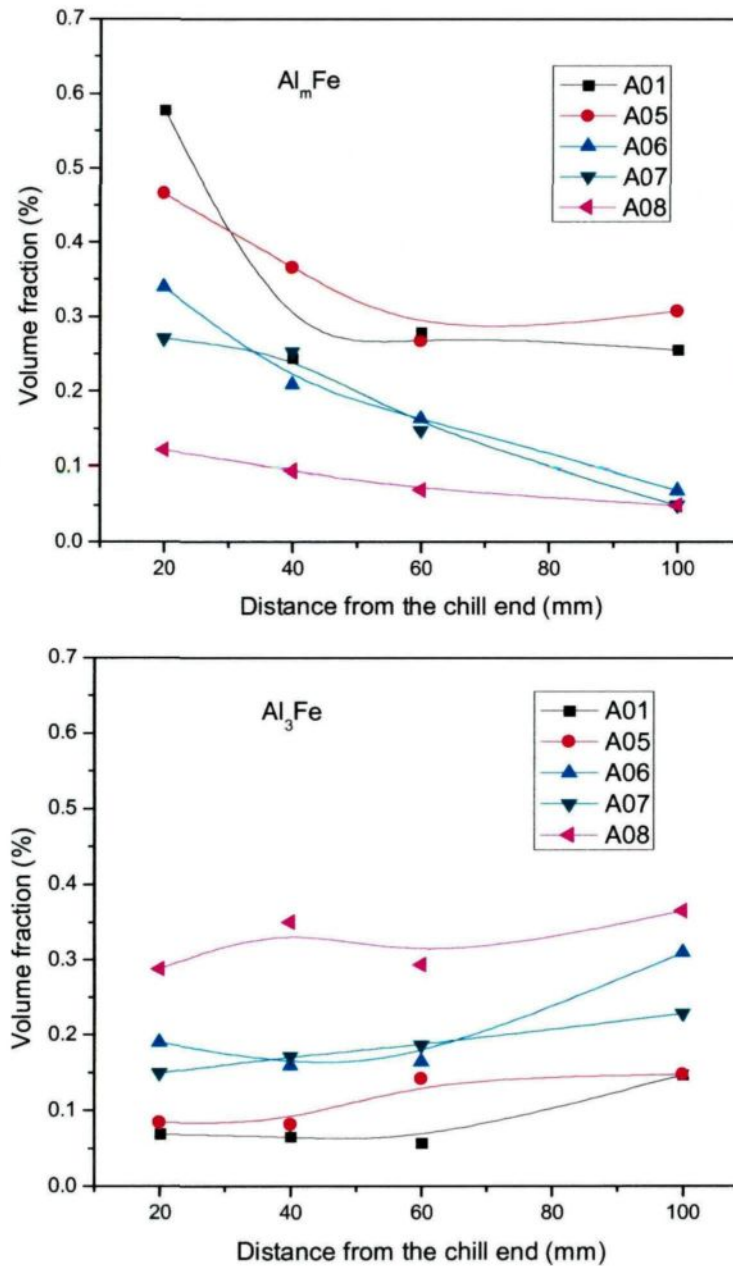


Figure 4.39:EBSD diffraction patterns and corresponding solutions of different type of Fe intermetallic phases in A08 alloy a)  $\text{Al}_m\text{Fe}$ , b)  $\text{Al}_6\text{Fe}$ , c)  $\text{Al}_7\text{Fe}_2\text{Si}$ , d)  $\text{Al}_3\text{Fe}$ .

### 4.4.3 Image analysis results

The distribution of each Fe intermetallic phase in the ingots A01, A05~A08 is plotted in Figure 4.40:





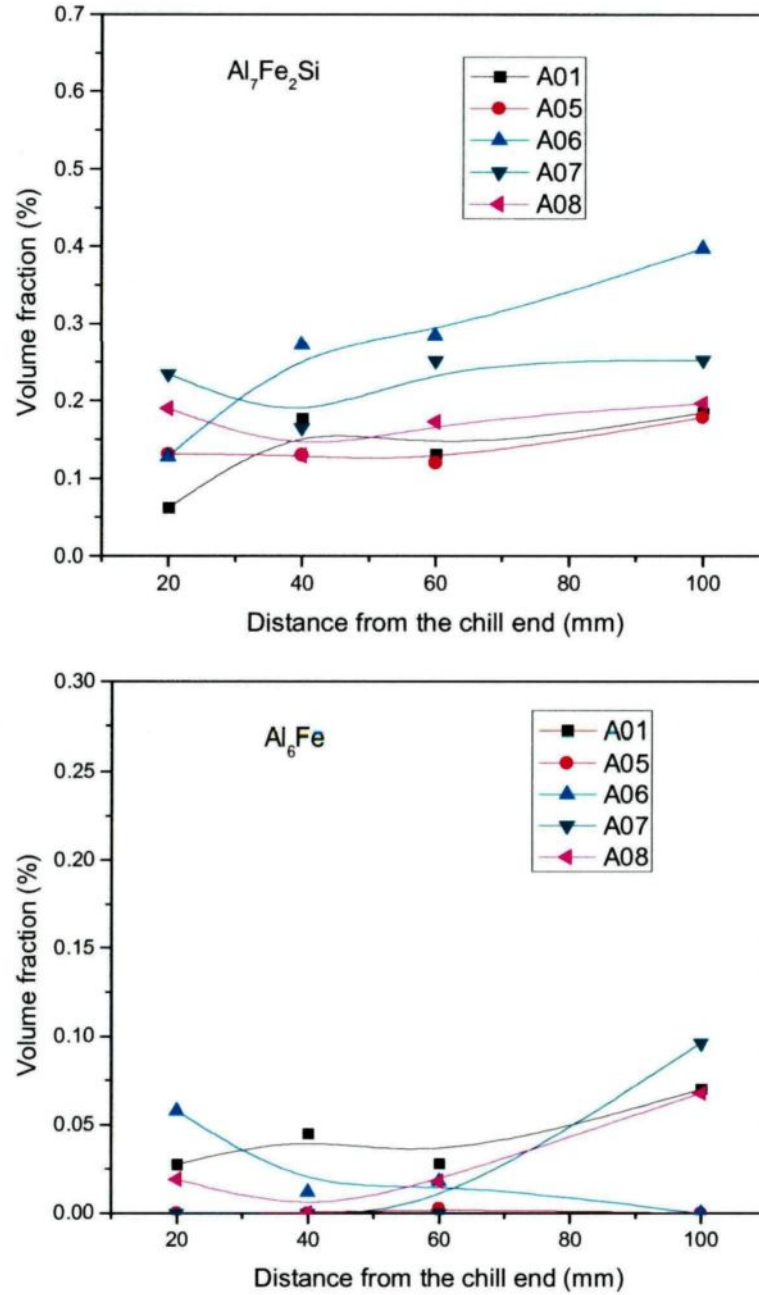


Figure 4.40: The distribution of Fe intermetallic phases in AA5657 alloy ingots with different Ni content. (a)  $Al_mFe$ , (b)  $Al_3Fe$ , (c)  $Al_7Fe_2Si$ , (d)  $Al_6Fe$ .

In Figure 4.40, we can find that the volume fraction of  $Al_mFe$  has a tendency to decrease with the Ni content in the ingot. On the contrary,  $Al_3Fe$  increase as the Ni level increase in the ingot.  $Al_7Fe_2Si$  has no major difference in these ingots. For  $Al_6Fe$ , it decreases obviously with the level of Ni content rising. In the low Ni content alloy

A01,  $\text{Al}_m\text{Fe}$  is the predominant phase in the fast solidification region, while  $\text{Al}_3\text{Fe}$  and  $\text{Al}_6\text{Fe}$  are dominant in the low solidification region. The main effect of Ni addition is the promotion of  $\text{Al}_3\text{Fe}$  and makes  $\text{Al}_3\text{Fe}$  a dominant phase from the fast solidification region to low solidification region.

The addition of Ni can not only has impact on the quantity of each type of Fe intermetallic phases, but also has impact on total Fe intermetallic phases volume fraction. Figure 4.41 shows the total volume fraction of Fe intermetallic phases in A01 and A05~A08 ingots.

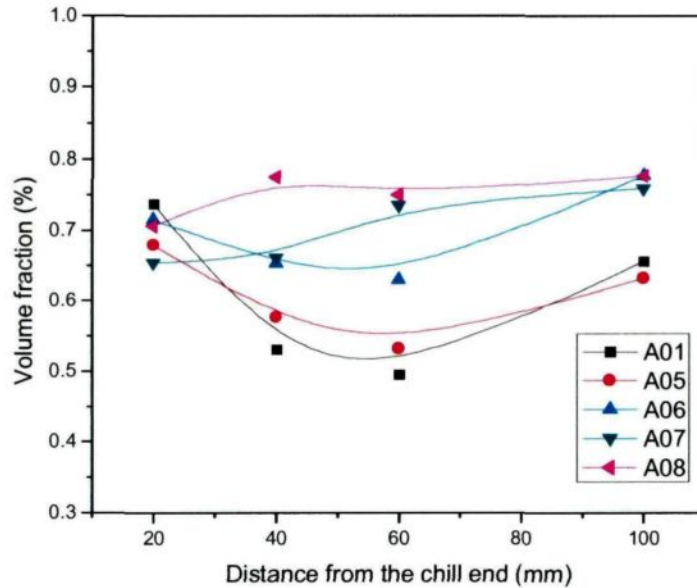


Figure 4.41: Total Fe phases volume fraction in the Ni containing ingots.

As we can see, the total Fe phases volume fraction has a tendency to increase with the Ni content increase, which indicates that the Ni addition may probably decrease the solid solubility of Fe, makes it segregate to the grain boundary and form secondary Fe intermetallic phases during DC casting process.

During solidification process, most of the Ni content was pushed towards the rest



of the liquid where the Fe intermetallic phases nucleate and grow<sup>12</sup>. The fact that raising the level of Ni in AA5657 cast alloys promotes  $Al_3Fe$  over  $Al_6Fe$  and  $Al_mFe$  can be explained by the effect of Ni addition on competitive nucleation and competitive growth of phases.

(1) The impact on competitive nucleation

In previous researches, people have found that the impurities present in the alloy or grain refiner additions made during casting process may provide nucleation sites for phases. For example,  $Al_mFe$  was found by X.-G. Chen nucleates directly on  $TiB_2$  and  $TiC$  particles in the sample with both  $AlTiB$  and  $AlTiC$  addition<sup>12</sup>. The findings by Hsu et al show that Ca promotes  $\alpha-AlFeSi$  in 6xxx-series Al alloys through the formation of  $CaAl_2Si_2$  during solidification<sup>59</sup>. The present study carried out in AA5657 cast alloy by using EDS shows that  $Al_3Fe$  particles usually contain some amount of Ni (See Figure 4.33), which indicates that the enriched Ni in the interdendritic regions may act as nucleation sites for  $Al_3Fe$ . In addition, for the faced eutectic  $Al_3Fe$ , it has the lowest branching ability among the four types of Fe intermetallic phases, and prefers a repeat nucleation rather than grow in a continuous way. The addition of Ni as potential nuclei for  $Al_3Fe$  makes the formation of  $Al_3Fe$  much easier than that of  $Al_mFe$ ,  $Al_6Fe$ . Thus, it is much easier for  $Al_3Fe$  to form and growth even in the fast solidification region. The particle density of  $Al_3Fe$  was found increase with the level of Ni content increase in the ingots (Figure 4.42), which provides an efficient support for this proposal.

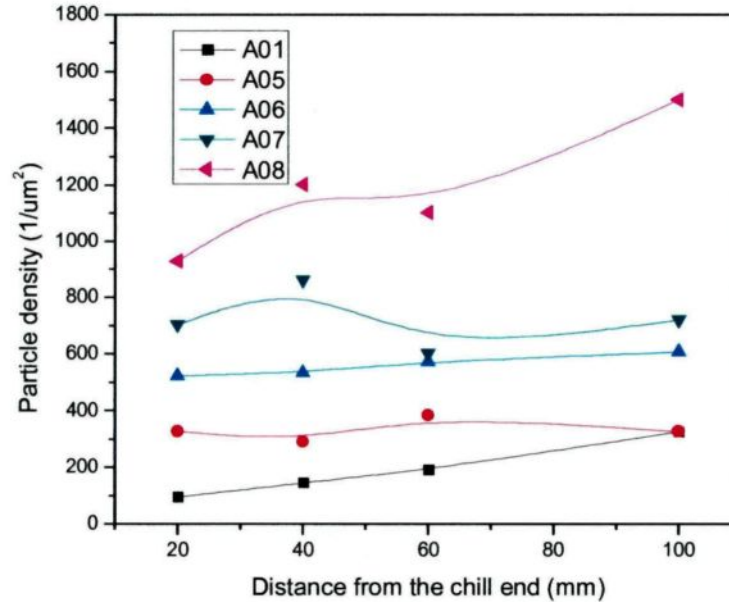


Figure 4.42: Effect of Ni on  $\text{Al}_3\text{Fe}$  particle density.

## (2) The impact on competitive growth

For the unit cell of  $\text{Al}_3\text{Fe}$ , it has frequently been reported probably has tendency to twinning<sup>60,61</sup>. In C.M. Allen et al's work<sup>59</sup>, they proposed that impurities may promote twinning, by providing a high density of edges and corners to which atoms can attach more easily, which in turn promote the growth of faceted eutectic  $\text{Al}_3\text{Fe}$ . This theory has good agreement with the present findings.

In conclusion, the increase of Ni in AA5657 alloy ingot promotes  $\text{Al}_3\text{Fe}$  and suppresses  $\text{Al}_m\text{Fe}$  and  $\text{Al}_6\text{Fe}$ . Ni content over the amount of 390 ppm forms new Ni containing intermetallic phase.

## 4.5 Effect of V on Fe intermetallic phases in DC simulator cast AA5657 ingots

V is present in the primary aluminium metal as an impurity, at present, its typical concentration in commercial Al alloys ranges between 10 – 200 ppm<sup>62</sup>. In the recent years, the levels of element V is increasing quite fast in aluminium alloys and may exceed some plant specifications, because of the rising levels in the raw materials (Figure 4.43). Unlike the low solubility of Ni, at a concentration below 1000 ppm, the V-containing intermetallic phases are difficult to form due to the high solubility of V in aluminium<sup>63</sup>. While according to X. G. Chen's findings, an insoluble particles (Ti,V)B<sub>2</sub> form directly in the melt in the case of AlTiB grain refiner addition<sup>12</sup>.

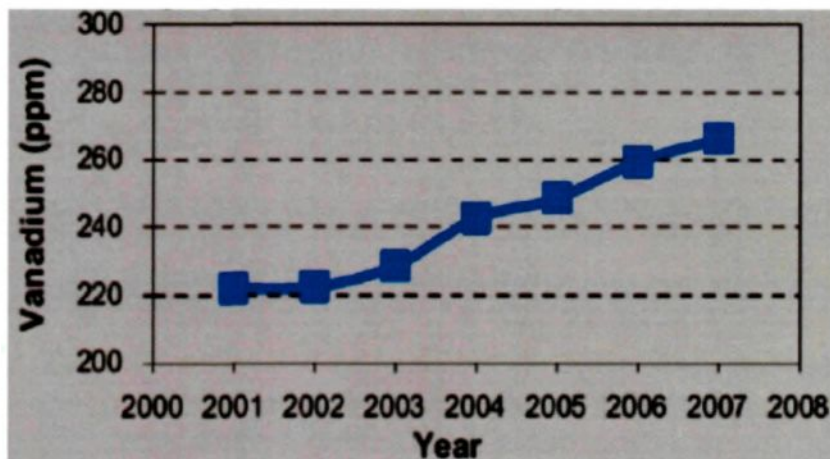


Figure 4.43: Increase in the vanadium content of coke over time<sup>64</sup>.

V is known to raise the recrystallisation temperature and has some grain refining effect and to promote the formation of cubic  $\alpha$ -AlFeSi in AlMgSi alloy as with Mn<sup>62</sup>. In addition, V was found to affect the Fe intermetallic phases selection and cause unwanted color variation on the anodized sheet<sup>62</sup>. In the present study, the goal is to make clear the effect of increasing V on Fe intermetallic selection in DC simulator

AA5657 cast ingots.

Three levels of V content ingots A02~A04 were cast (See Table 3.2), in which the V levels range from 240 ppm via 330 ppm to 480 ppm. Unlike the Ni addition ingots, V was not found concentrate on the interdendritic region due to its high solubility in Al matrix.

#### 4.4.1 Ingots structure

Figure 4.44 shows the DC ingot structure taken from different V containing ingots with a distance of 40 mm from the chill ends.

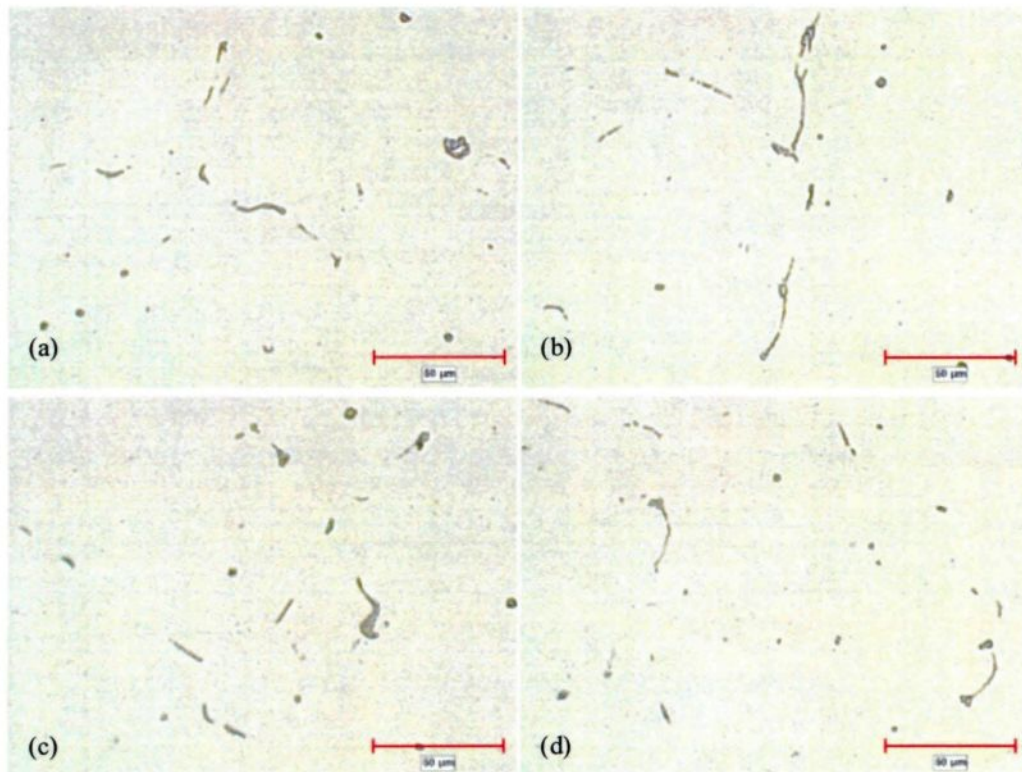


Figure 4.44: Photomicrograph taken from different V containing DC cast ingots with a distance of 40 mm from the chill ends. (a) 175 ppm V (A01), (b) 240 ppm V (A02), (c) 330 ppm V (A03), (d) 480 ppm V (A04).

From Figure 4.44, we can find most of intermetallic phase morphology in 2-D

takes an interdendritic shape, which makes it difficult to be identified based on their morphology. The characteristics of each type of Fe intermetallic phases obtained by using SEM and EDS are shown in Figure 4.45 and Figure 4.46.

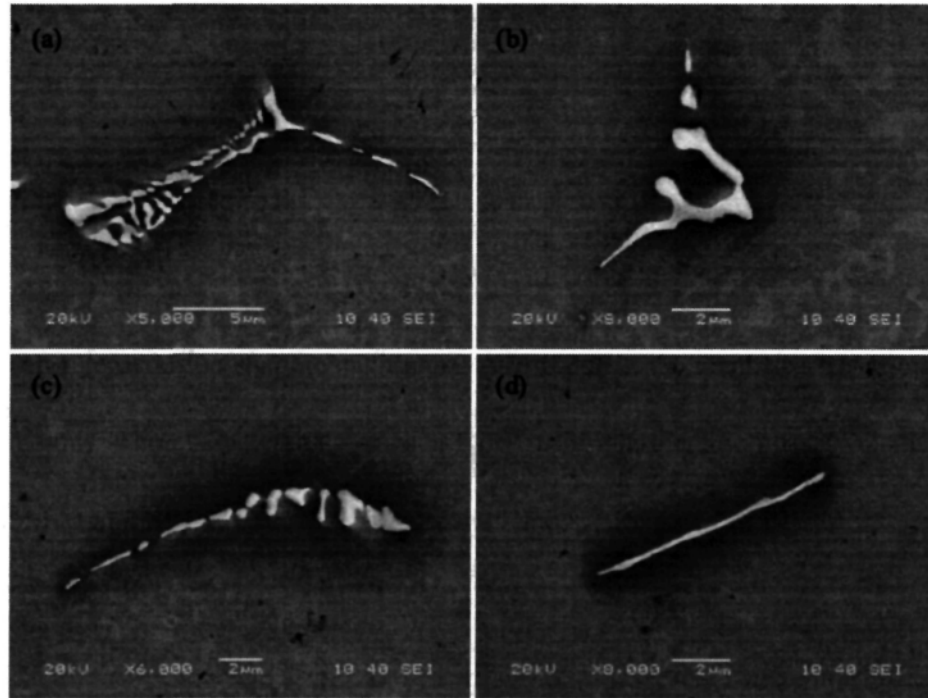


Figure 4.45: Fe intermetallic phases morphology under SEM in A04 alloy. (a) fine feathery like, (b) Chinese script, (c) curved plates with wings, (d) needle like.

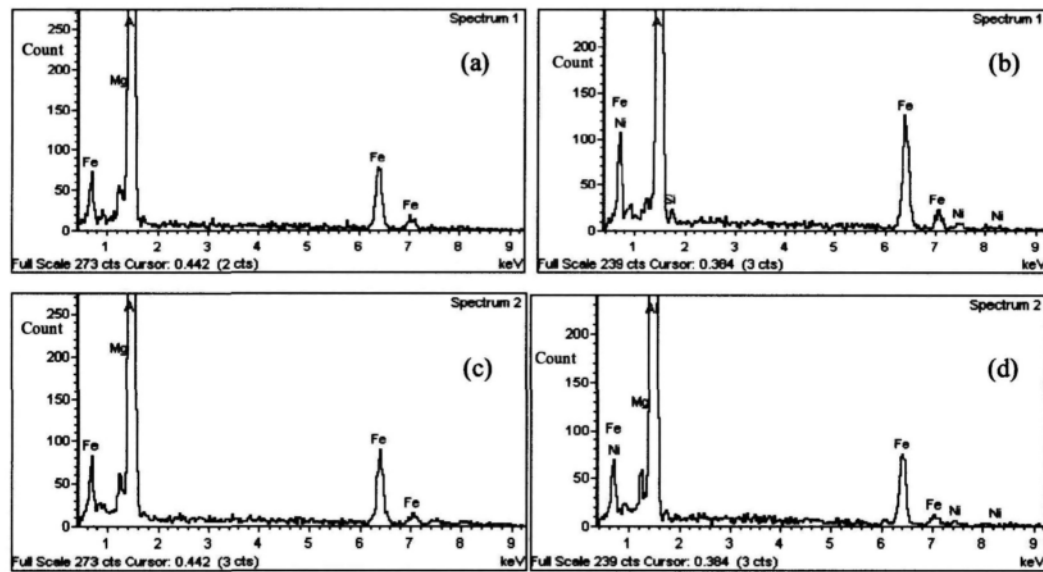


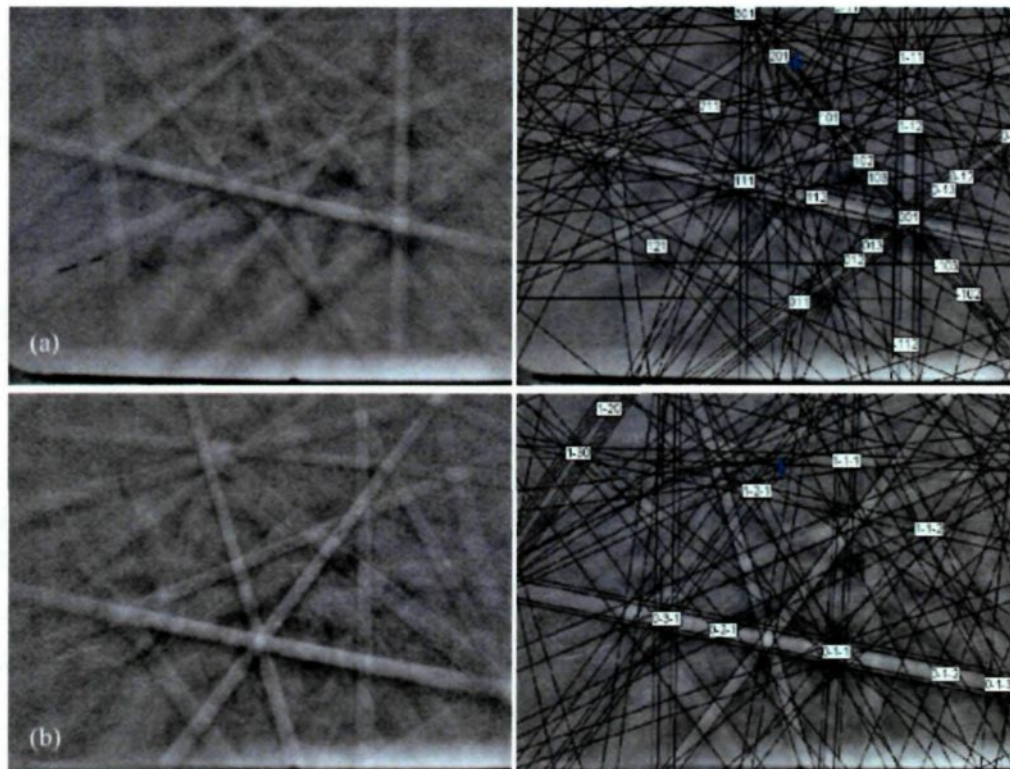
Figure 4.46: EDS spectra of Fe intermetallic particles in A04 alloy. (a) fine feathery like, (b) Chinese script, (c) curved plates with wings, (d) needle like.



From the results above, we can find that the typical morphologies, EDS results of the  $\text{Al}_m\text{Fe}$ ,  $\text{Al}_6\text{Fe}$ ,  $\text{Al}_3\text{Fe}$  and  $\text{Al}_7\text{Fe}_2\text{Si}$  were similar with those in industry AA5657 cast ingot (see chapter 4.1).

#### 4.5.2 EBSD patterns

EBSD diffraction patterns of the four conventional phases were found similar with those in commercial AA5657 cast ingot, which were identified as  $\text{Al}_m\text{Fe}$ ,  $\text{Al}_7\text{Fe}_2\text{Si}$ ,  $\text{Al}_6\text{Fe}$  and  $\text{Al}_3\text{Fe}$ . The following images show the diffraction patterns and their corresponding solutions of different intermetallic got by EBSD. It was found that the feathery like morphology particles are mostly  $\text{Al}_m\text{Fe}$ , chinese script particles are mostly  $\text{Al}_7\text{Fe}_2\text{Si}$ , curved plate particles are mostly  $\text{Al}_6\text{Fe}$  while needle like particles are mostly  $\text{Al}_3\text{Fe}$ .



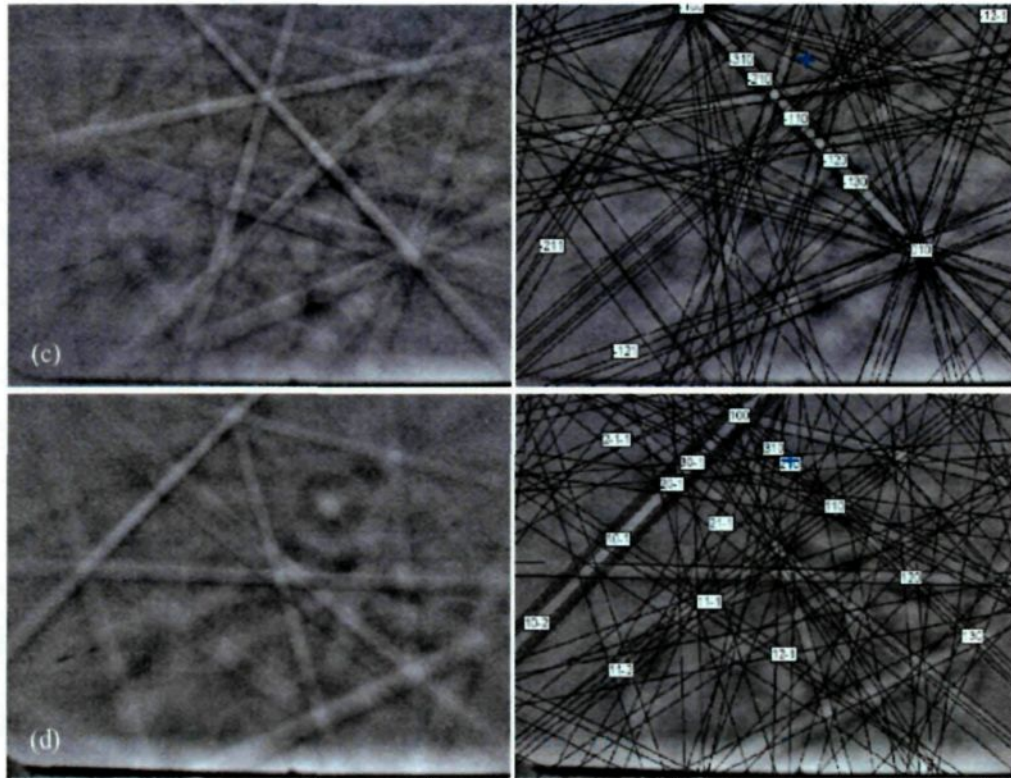
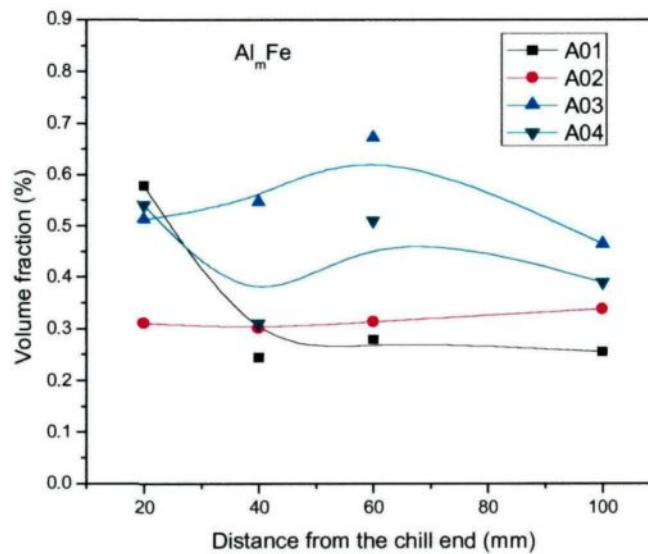


Figure 4.47: EBSD diffraction patterns and corresponding solutions of different type of Fe intermetallic phases in A04 alloy, a)  $\text{Al}_m\text{Fe}$ , b)  $\text{Al}_6\text{Fe}$ , c)  $\text{Al}_7\text{Fe}_2\text{Si}$ , d)  $\text{Al}_3\text{Fe}$ .

### 4.5.3 Image analysis results

The distribution of each phase in the ingots A01 ~ A04 is listing in Figure 4.48:



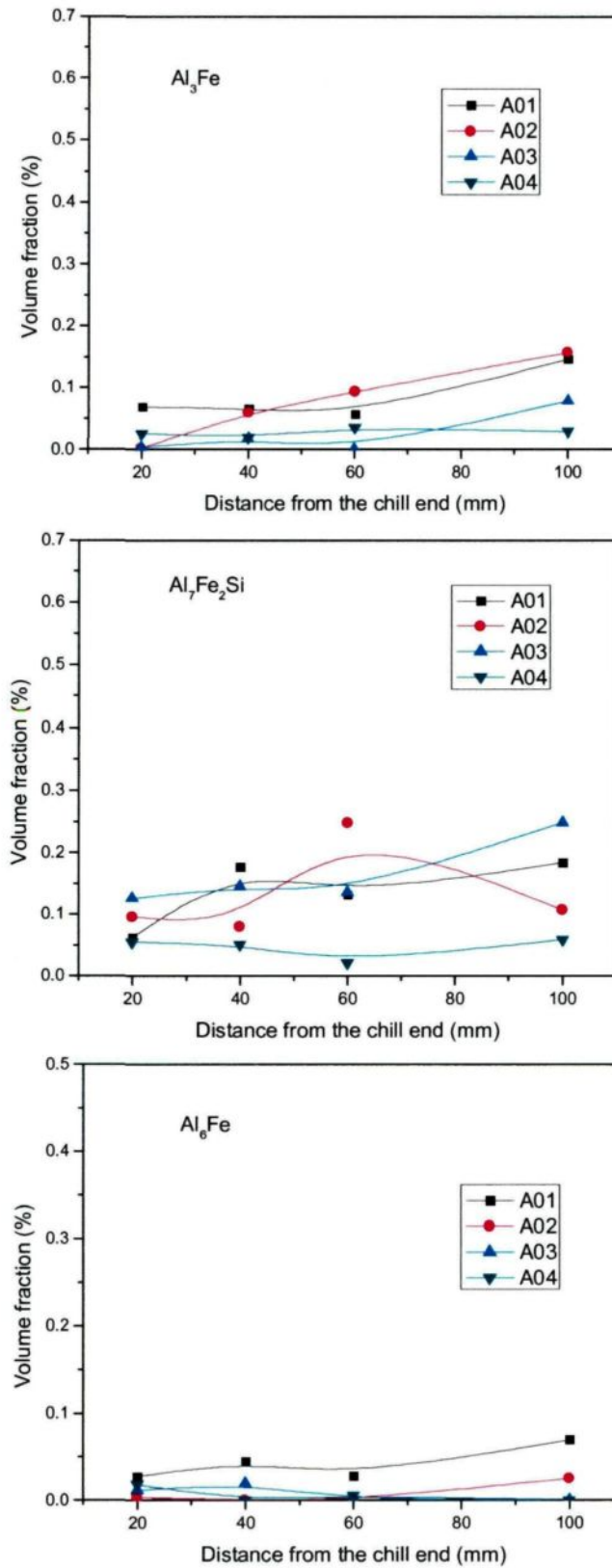


Figure 4.48: The distribution of Fe intermetallic phases in AA5657 alloy ingots with different levels of V content: (a)  $Al_mFe$ , (b)  $Al_3Fe$ , (c)  $Al_7Fe_2Si$ , (d)  $Al_6Fe$ .



In the figures above, we can clearly find that as the levels of V content in the AA5657 alloy ingot increase,  $Al_mFe$  has a tendency to increase in the location of the ingots with low cooling rates (Figure 4.48 (a)). On the contrary, the amount of  $Al_3Fe$ ,  $Al_6Fe$  and  $Al_7Fe_2Si$  has a tendency to decrease with the increasing levels of V in these ingots (Figure 4.48 (b-d)). These findings suggest that V can promote the formation of  $Al_mFe$  and makes it grow easier in the low cooling rate region, while it suppress the formation of  $Al_3Fe$ ,  $Al_6Fe$  and  $Al_7Fe_2Si$ .

The total volume fraction of Fe intermetallic phases in the V containing ingots is shown in Figure 4.49:

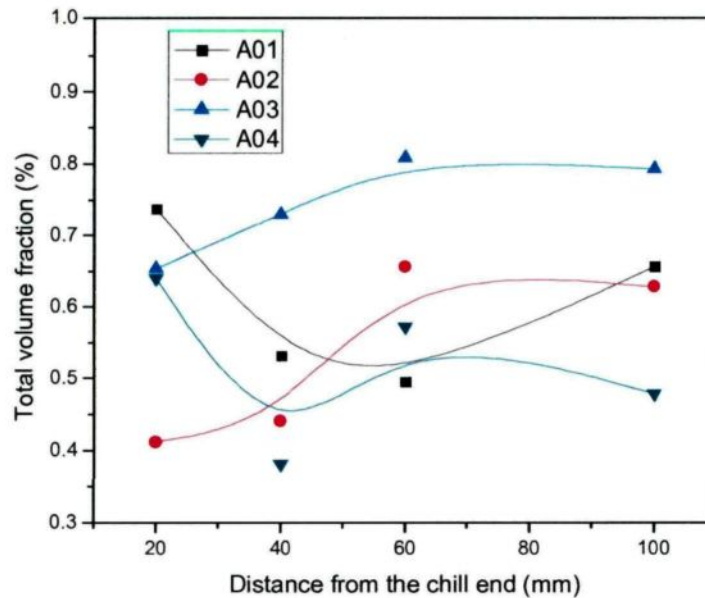


Figure 4.49: Total Fe phases volume fraction in the V containing ingots.

As we can see, unlike the effect of Ni on total Fe intermetallic phases volume fraction, the change of total Fe phases volume fraction after V addition is not uniform.

In order to understand the effect of trace element V on the phase selection in AA5657 alloy, it is necessary to consider both nucleation and growth aspects. It was

proposed in the previous research that under the condition of Al-Ti-B grain refinement addition, the addition of trace element V probably forms an insoluble particles  $(\text{Ti,V})\text{B}_2$  directly in the melt during solidification process<sup>12</sup>. As the solidification proceeds, these insoluble particles are pushed towards the rest of the interdendritic liquid, where the Fe intermetallic phases nucleate and grow. The enrichment of V particles may leads to the local solidification behavior change. Two possible mechanisms can be employed to explain the promotion of  $\text{Al}_m\text{Fe}$  over other intermetallic phases:

(1) Nucleation of insoluble V containing particles. In the AA5657 alloy used in present study, AlTiB or AlTiC was added during the industry DC casting process as grain refiner, some amount of Ti was found present in the AA5657 alloy (See Table 3.1). The  $\text{Al}_m\text{Fe}$  was found nucleate directly on  $\text{TiB}_2$  and TiC particles in X.-G Chen's research<sup>12</sup>. The addition of V in the DC simulator cast ingots forms an insoluble particles  $(\text{Ti,V})\text{B}_2$  which may act as efficient nuclei for  $\text{Al}_m\text{Fe}$ . The  $\text{Al}_m\text{Fe}$  particles form at higher cooling rates than the other phases, because it has the lowest eutectic temperature than  $\text{Al}_6\text{Fe}$ ,  $\text{Al}_3\text{Fe}$  and  $\alpha\text{-AlFeSi}$ . The exists of insoluble particles may lower the critical cooling rate and raise the nucleation temperature for  $\text{Al}_m\text{Fe}$ . The element V can change the nucleation temperature of Fe intermetallic phases in Al alloy has been proved in CM. Allen et al's research (Figure 4.50)<sup>65</sup>.

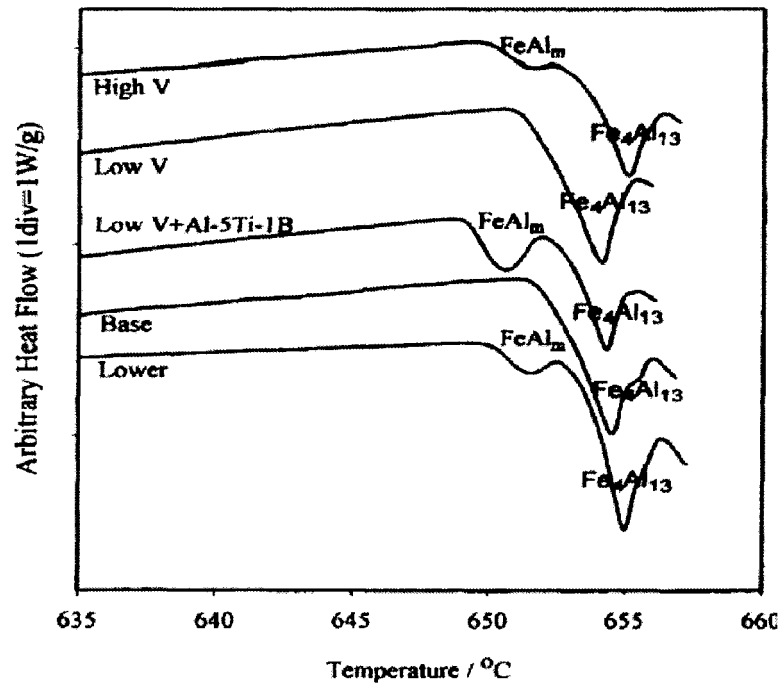


Figure 4.50: Entrained droplet melting differential scanning calorimeter traces from lxxx series aluminium alloys with a high purity base, a low purity base, high purity base plus high and low levels of vanadium, and high purity base with a combination of low vanadium and grain refiner addition<sup>65</sup>.

In Figure 4.50, the peaks represent the melting of aluminium-intermetallic eutectics. In a low purity material, two peaks are observed, representing the melting of the equilibrium  $\text{Al-Fe}_4\text{Al}_{13}$  eutectic and the metastable  $\text{Al-FeAl}_m$  eutectic. The high purity base material only contains the equilibrium  $\text{Al-Fe}_4\text{Al}_{13}$  eutectic. Additions to this base material of a combination of low levels of vanadium with Al-Ti-B grain refiner, lead to the formation of the metastable  $\text{Al-FeAl}_m$  eutectic, while the addition of high levels of vanadium, lead to the increase of  $\text{Al-FeAl}_m$  eutectic melting temperature (nucleation temperature) increase. In the present study, the AA5657 alloy was grain refined by Al-5Ti-B refiner, the addition of V may have similar effect on the  $\text{Al}_m\text{Fe}$  eutectic melting temperature.

Let us take  $\text{Al}_m\text{Fe}/\text{Al}_3\text{Fe}$  for example to explain how the raising level of V promotes  $\text{Al}_m\text{Fe}$  formation over other Fe intermetallic phases. As indicated in Figure 4.51, the nucleation temperature for  $\text{Al}_m\text{Fe}$   $T_2$  and  $\text{Al}_3\text{Fe}$   $T_1$ ,  $T_2 < T_1$ , the cooling rate  $T_{c2} < T_{c1}$ , the addition of V raising the nucleation temperature of  $\text{Al}_m\text{Fe}$  (the dotted line in the figure) while keep the nucleation temperature of  $\text{Al}_3\text{Fe}$  the same, this effect obviously lower the critical cooling rates from  $T_{c1}$  to  $T_{c2}$ , which makes it easier for  $\text{Al}_m\text{Fe}$  to form at lower cooling conditions.

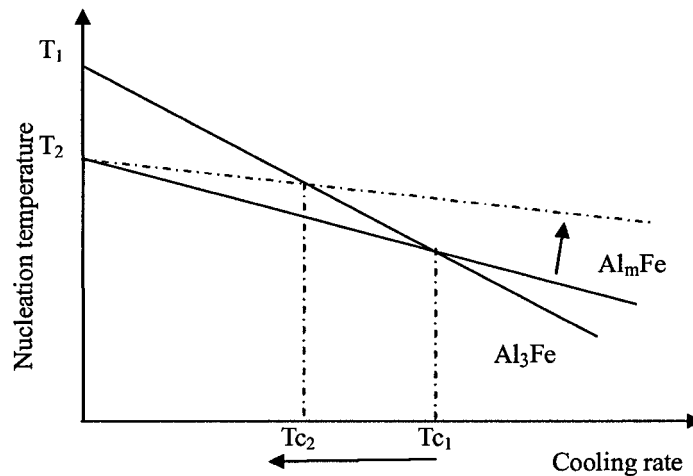


Figure 4.51: Schematic illustration of the formation of V containing particles act as preferential nucleation sites of  $\text{Al}_m\text{Fe}$ , raising the nucleation temperature and lower the critical cooling rate  $T_c$  for  $\text{Al}_m\text{Fe}$  formation.

(2) Impact on the growth behavior. S.J.Maggs<sup>13</sup> proposed in his study that the elements segregated into the remaining liquid in the solidification process tend to have big effect on the intermetallic phases even at very low trace level. For the intermetallic phase that grows in a faceted mode by step-wise growth rather than in a non-faceted continuous manner, the trace element could poison the site where the intermetallic particles attach the liquid, which can cause significant decrease in the growth temperature, and caused it lose out to another phase. Thus, faceted phase

Al<sub>3</sub>Fe lose out to the non-faceted phase Al<sub>m</sub>Fe in AA5657 alloy ingot after the V addition.

Recently, some researchers have found that the solidification velocity other than cooling rate is the more fundamental parameter that effects the Fe intermetallic phases selection<sup>59</sup>, it was found that Al<sub>m</sub>Fe forms in the growth condition with the fastest growth velocity, then are the phases  $\alpha$ -AlFeSi and Al<sub>6</sub>Fe. Al<sub>3</sub>Fe forms at the lowest growth velocity condition. According to Dong, Liang and Howard, Jones<sup>66</sup>, the growth temperature,  $T_g$ , with the solidification velocity, U, fit the form:

$$T_g = T_{EU} - BU^{1/2}$$

Where  $T_{EU}$  is the equilibrium solidification temperature (i.e.  $T_{EU} = T_g$  at  $U = 0$ ) and B is a constant varies from eutectic to eutectic. In the last stage of solidification, the intermetallic has to grow in an intergranular liquid, which has less space and complex shape. Thus, frequent branching ability is needed for a certain phase growth. Among the four intermetallic phases observed in AA5657 alloy ingot, Al<sub>m</sub>Fe mostly adopt a fine feathery morphology and has the branching ability than others<sup>4</sup>. So the Al<sub>m</sub>Fe has the most favorable condition to growth in this alloy ingot. Similarly, we will take Al<sub>m</sub>Fe/Al<sub>3</sub>Fe for example to explain the promotion of V on Al<sub>m</sub>Fe over other phases. As shown in Figure 4.52, the growth temperature of Al<sub>3</sub>Fe  $T_1$  and Al<sub>m</sub>Fe  $T_2$ ,  $T_1 > T_2$ , the solidification velocity  $V_1 > V_2$ . The main function of the grain refiner addition is change the primary aluminium structure from columnar to equiaxed. Moreover, the effect of grain refiner can be enhanced in the combination of some

alloying and trace elements. The addition of V in the DC cast alloy makes the aluminium further refined, which makes the growth condition for  $\text{Al}_3\text{Fe}$  more unfavorable due to its step-wise growth manner. This, in turn, leads to the growth temperature of  $\text{Al}_3\text{Fe}$  decrease (the dotted line in the figure), Thus, the range of growth velocity for  $\text{Al}_m\text{Fe}$  is extend from  $V_1$  to  $V_2$ , and make the  $\text{Al}_m\text{Fe}$  to grow in the low growth velocity region.

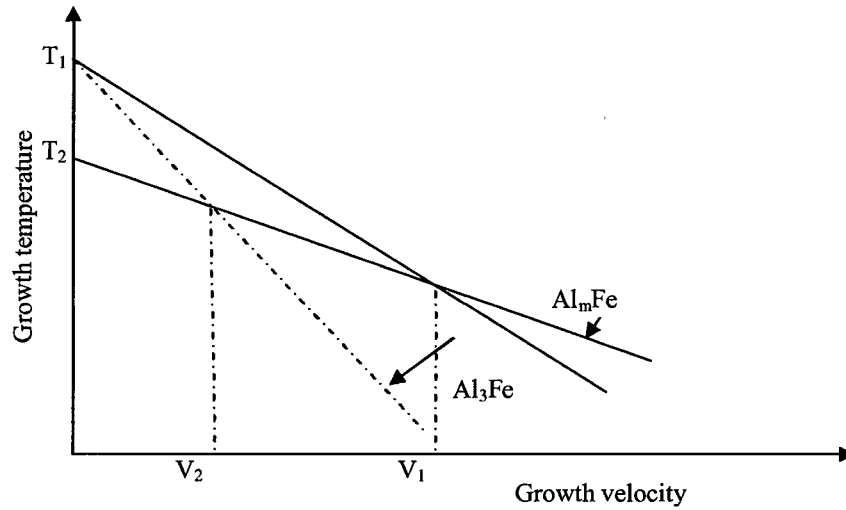


Figure 4.52: Schematic illustration of the V addition decrease the growth temperature of  $\text{Al}_3\text{Fe}$ , lower the critical growth velocity for  $\text{Al}_m\text{Fe}$ .

In conclusion, the effect of rising levels of V in AA5657 alloy ingot can heavily promote  $\text{Al}_m\text{Fe}$  and suppress  $\text{Al}_3\text{Fe}$ ,  $\text{Al}_6\text{Fe}$ , and  $\text{Al}_7\text{Fe}_2\text{Si}$ .

## 4.6 Effect of The combined addition of V and Ni on Fe intermetallic phases in DC simulator cast AA5657 ingots

In chapter 4.4 and 4.5, the effect of Ni or V is investigated in the lab. However, the levels of Ni and V could rise simultaneously in industry practice. Thus, it is quite necessary to understand the combined effect of Ni and V on Fe intermetallic phases. In the present research, two ingots A09, A10 were casted using the DC simulator with different amount of Ni and V addition simultaneously (See Table 3.2).

### 4.6.1 Ingots Microstructure

Figure 4.53 shows the DC ingot structure taken from different A01, A09 (260 ppm V and 240 ppm Ni) and A10 (380 ppm V and 250 ppm Ni) ingots.

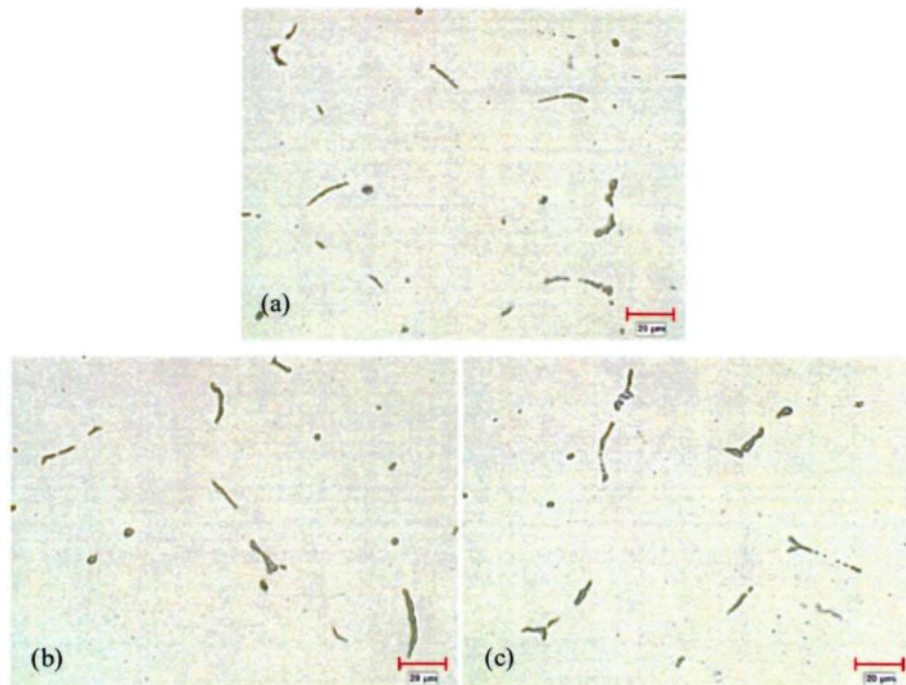


Figure 4.53: Microstructure taken from different V and Ni containing ingots with a distance of 40 mm from the chill ends. a) A01, b) A09, c) A10.

From the figures above, we can find that the 2-D morphology of intermetallic phases always appear interdendritic shape, there is no obvious change in the ingots microstructure with the V and Ni addition simultaneously. Further study of these intermetallic phases using SEM and EDS was carried out. The results are shown in Figure 4.54 and Figure 4.55.

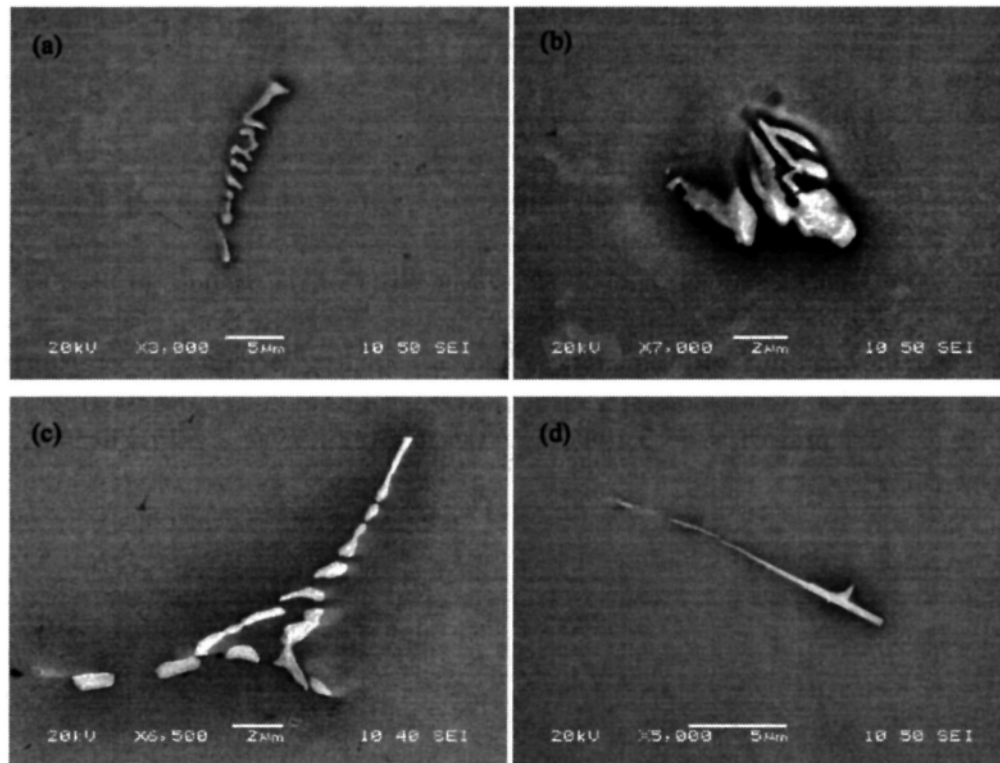


Figure 4.54: Fe intermetallic phases morphology under SEM in A10 alloy. (a) fine feathery like, (b) Chinese script, (c) curved plates with wings, (d) needle like.



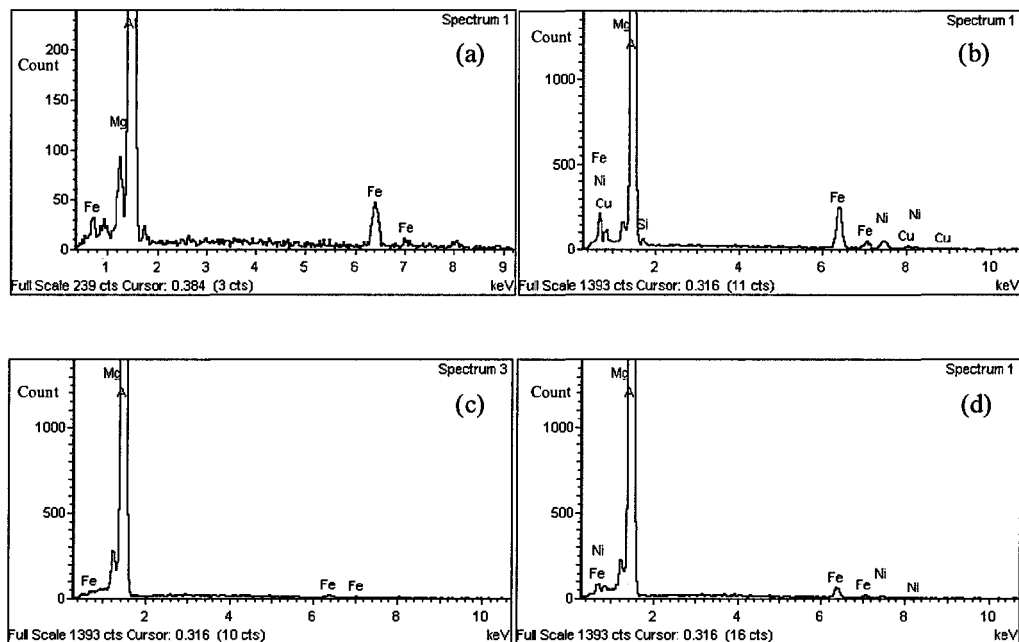


Figure 4.55: EDS spectra of Fe intermetallic phases in A10 alloy. (a) fine feathery like  $Al_mFe$ , (b) Chinese script  $Al_7Fe_2Si$ , (c) curved plates with wings  $Al_6Fe$ , (d) needle like  $Al_3Fe$ .

Form the results above, we can find that the typical morphologies, EDS results of the  $Al_mFe$ ,  $Al_6Fe$ ,  $Al_3Fe$  and  $Al_7Fe_2Si$  were similar with those in industry AA5657 cast ingot (see chapter 4.1).

## 4.2.2 EBSD patterns

The following images show the diffraction patterns and their corresponding solutions of different intermetallic got by EBSD. EBSD diffraction patterns of the four conventional phases in the V and Ni containing ingots were found similar with those in commercial AA5657 cast ingot, which were identified as  $Al_mFe$ ,  $Al_7Fe_2Si$ ,  $Al_6Fe$  and  $Al_3Fe$ .

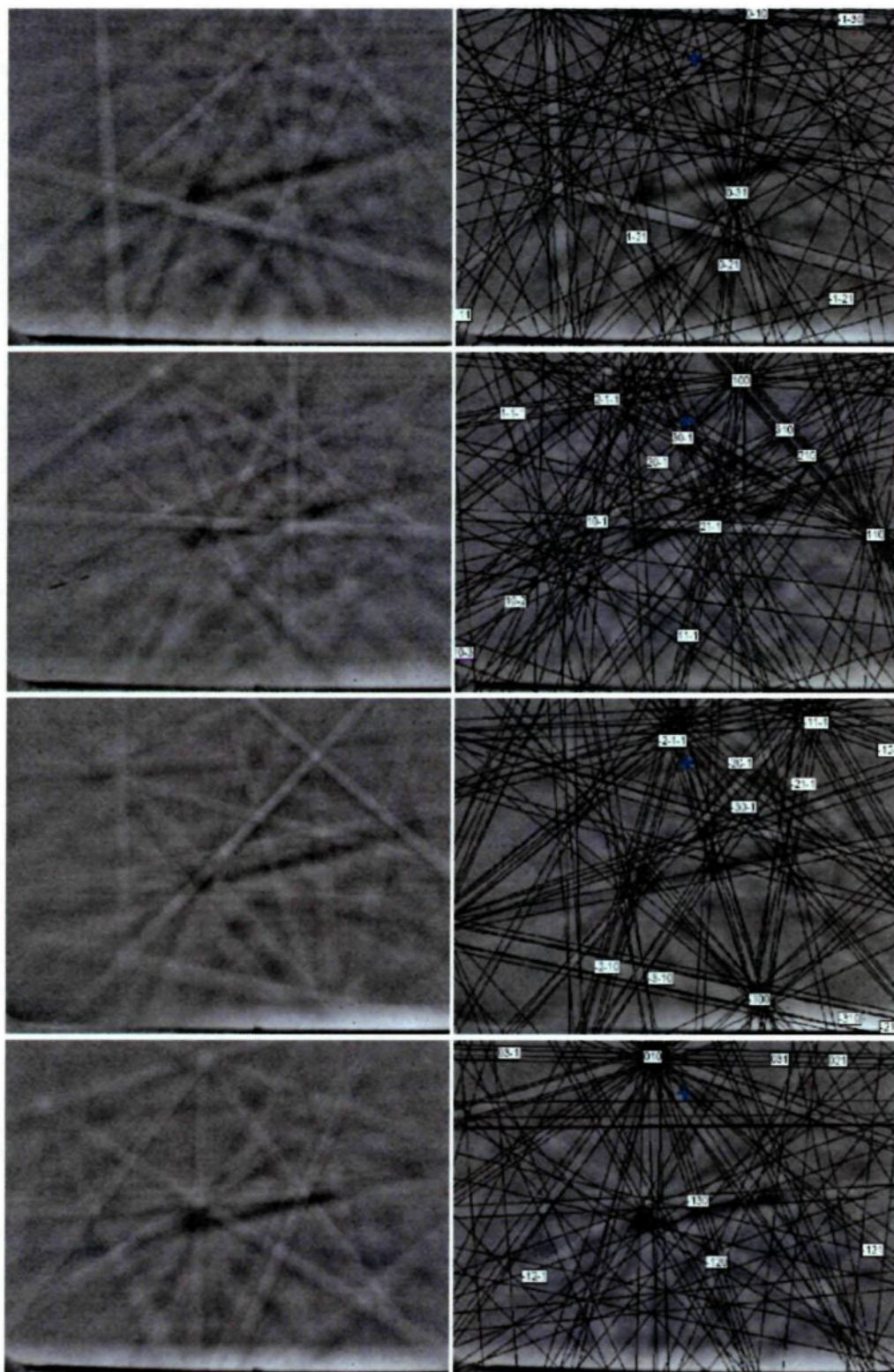
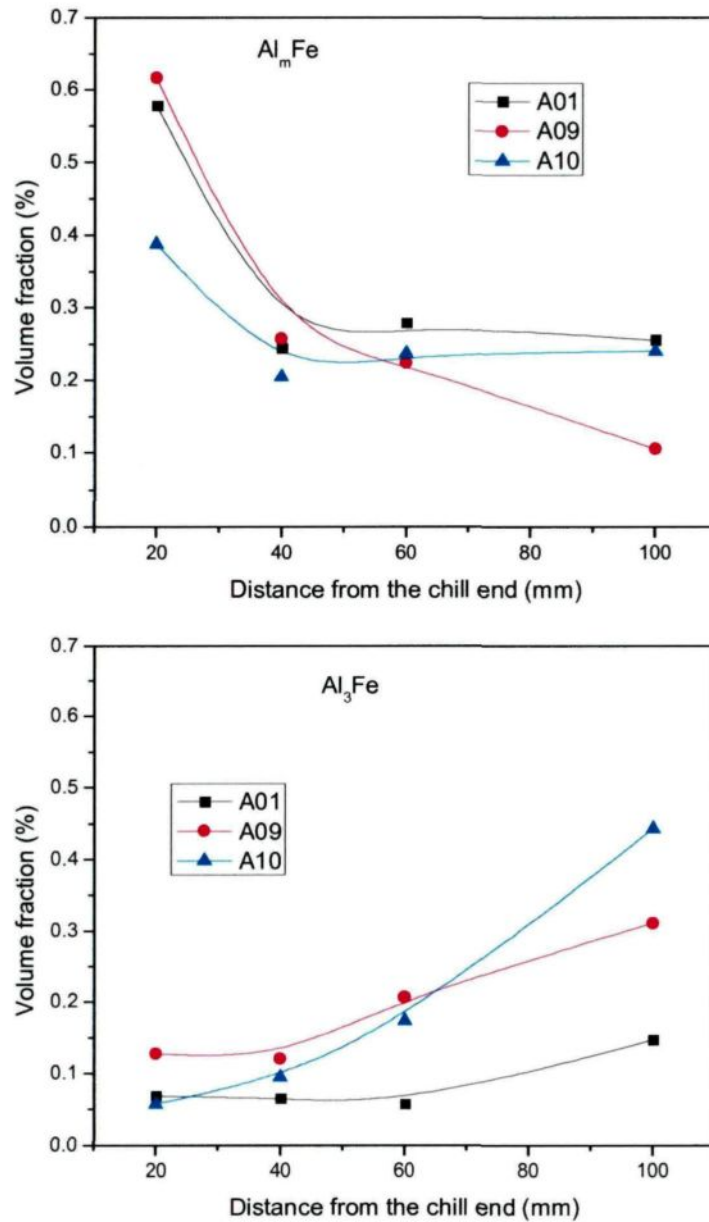


Figure 4.56: EBSD diffraction patterns and corresponding solutions of different type of Fe intermetallic phases in V containing ingots, a)  $\text{Al}_m\text{Fe}$ , b)  $\text{Al}_6\text{Fe}$ , c)  $\text{Al}_7\text{Fe}_2\text{Si}$ , d)  $\text{Al}_3\text{Fe}$ .

### 4.6.3 Image analysis results

The distribution of each phase in A09 and A10 compared with that in A01 is shown in Figure 4.57:



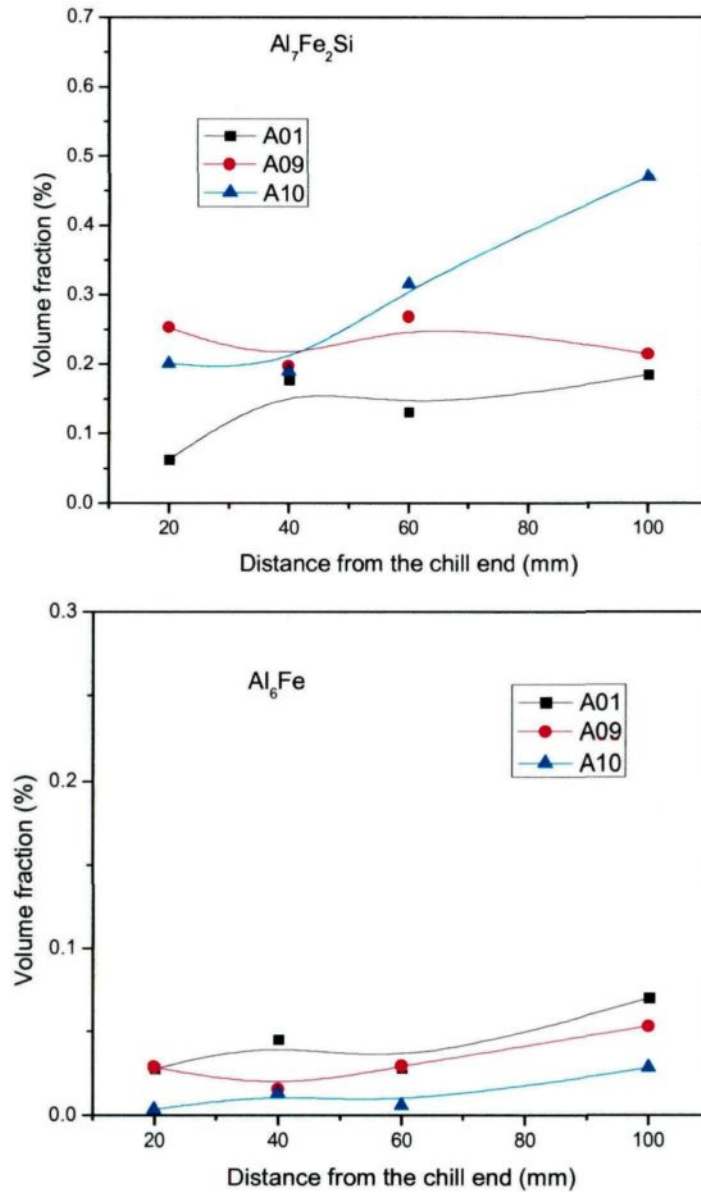


Figure 4.57: The distribution of Fe intermetallic phases in AA5657 alloy ingots with different levels of V and Ni content. a) Al<sub>m</sub>Fe, b) Al<sub>3</sub>Fe, c) Al<sub>7</sub>Fe<sub>2</sub>Si, d) Al<sub>6</sub>Fe.

From Figure 4.57, we can found that after the addition of V and Ni, the volume fraction of Al<sub>7</sub>Fe<sub>2</sub>Si and Al<sub>3</sub>Fe increase, while the volume fraction of Al<sub>6</sub>Fe decreases. There is no major effect of V and Ni addition on Al<sub>m</sub>Fe.

The total Fe intermetallic phases volume fraction in the ingots A01, A09 and A10 is shown in Figure 4.58:

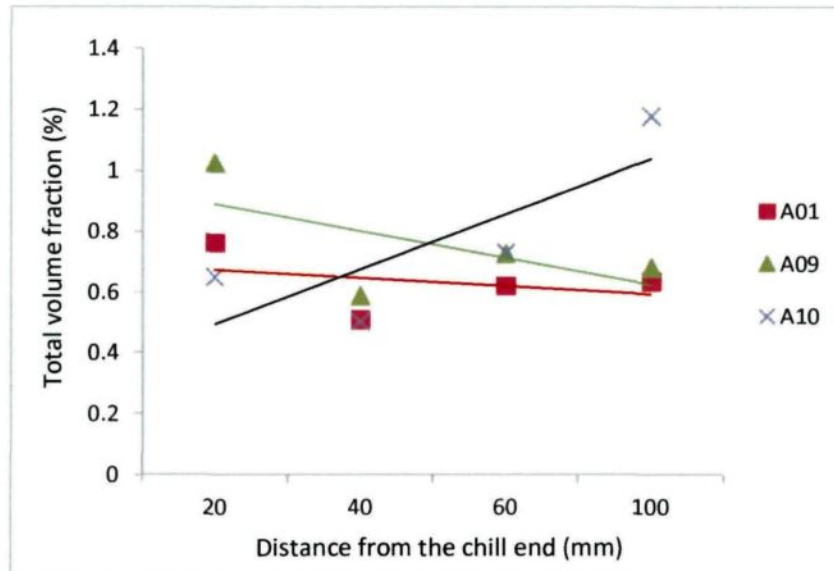


Figure 4.58: Effect of V and Ni on total Fe intermetallic phases volume fraction.

As we can see in Figure 4.58, there is no uniform tendency of total Fe intermetallic phases volume fraction when V and Ni are added simultaneously.

Although it is quite complicated to understand the combined effect of V and Ni on Fe intermetallic phases, we can try to explain some of the phenomenon by using the theory used in previous study. When refer to the previous findings, in which we find V can promote  $Al_mFe$  and Ni can promote  $Al_3Fe$ , when the level of V and Ni increase simultaneously in the DC casting ingot, the reverse effect of V and Ni on  $Al_mFe$  counteract their effect on  $Al_mFe$ , so it appears no big changes on the volume fraction of  $Al_mFe$ . The promotion of V and Ni addition on  $Al_3Fe$  reflect the effect of Ni on the Fe intermetallic phases, which indicates that Ni has advantage over V to show the effect on the Fe intermetallic phases in the ingots A09 and A10 used in this study. The mechanism of the effect that raising the level of V and Ni simultaneously promotes  $Al_7Fe_2Si$  over  $Al_6Fe$  is still not clear.

## Chapter 5 Conclusions and Suggestions for further work

### 5.1 Conclusions

1. Using a DC simulator, the solidification conditions in the sub-surface region of commercial DC cast ingots were successfully reproduced at the lab scale.
2. The transition of  $Al_mFe$ ,  $Al_6Fe$ ,  $Al_3Fe$  and  $Al_7Fe_2Si$  intermetallic phases were observed in both commercial and lab DC simulator casting AA5657 alloy ingots, but no visible FTZs were revealed as opposed to AA1050 alloy. The typical deep-etching morphology of  $Al_mFe$ ,  $Al_6Fe$ ,  $Al_3Fe$  and  $Al_7Fe_2Si$  were revealed by using deep-etching method.
3.  $Al_mFe$ ,  $Al_6Fe$ ,  $Al_7Fe_2Si$  and  $Al_3Fe$  intermetallic phases in DC cast Al ingots were successfully identified by using SEM, EDS and EBSD technique in combination.
4. A slice of AA1050 alloy ingot with a visible FTZ was studied. It was found  $Al_mFe$ ,  $Al_6Fe$ ,  $Al_3Fe$ ,  $Al_7Fe_2Si$  and a Ni containing intermetallic phases distribute across the FTZs. The quantitative analysis results of the Fe intermetallic phases show that the transition between  $Al_mFe$  and  $Al_6Fe$  is the main reason that causes the FTZs visible.
5. Raising the level of the trace element Ni promotes  $Al_3Fe$  in the whole ingot, suppress  $Al_mFe$  and  $Al_6Fe$ . High levels of Ni content more than 390 ppm promote the formation of a new Ni-containing intermetallic phase;
6. Increasing the level of the trace element V in AA5657 alloy heavily promotes  $Al_mFe$  and suppresses  $Al_3Fe$ ,  $Al_6Fe$ ,  $Al_7Fe_2Si$ .



7. Increasing the level of the trace elements V and Ni simultaneously suppress  $\text{Al}_6\text{Fe}$  and promote  $\alpha\text{-AlFeSi}$  and  $\text{Al}_3\text{Fe}$ ;
8. The mechanism of the effect of trace elements V or/and Ni on Fe intermetallic phases selection is relate to the fact that the trace element impurities can affect the nucleation and growth behavior of certain phases.

## 5.2 Suggestions for further work

This study concentrated on the Fe intermetallic phases characterization and the effect of trace element V or/and Ni on the Fe intermetallic phases in AA5657 alloys. A slice of AA1050 alloy ingot was also studied to better understand the transition of Fe intermetallic phases across the FTZs. Based on the results obtained in this research, it would be useful to investigate the following concepts further:

1. The detailed information of the Ni-containing intermetallic phase appears in the high Ni content ingots and the factors that affect its formation.
2. Evaluate reflectivity of AA5657 alloy products and correlation with the Fe intermetallic phases content.
3. Further the study of the combined effect of V and Ni on Fe intermetallic phases.



## APPENDICES

*Appendices A: Table of phase crystals input the Database used in EBSD identification<sup>28,32</sup>*

Phase	State	Bravais Lattice & Space Group	Lattice Parameter
Al		Cubic Fm -3 m(225)	a = 0.4049nm
Al <sub>m</sub> Fe	Metastable	Body centered tetragonal	a = 0.884 nm b = 0.2.16 nm
Al <sub>6</sub> Fe(Mn)	Metastable	C-centered orthorombic Cmcm (63)	a = 0.7437 nm b = 0.6492 nm c = 0.8788 nm
Al <sub>3</sub> Fe	Stable	C centered monoclinic C2/m (12)	a = 1.549 nm b = 0.808 nm c = 1.2476 nm $\beta = 107.72^\circ$
Al <sub>7</sub> Fe <sub>2</sub> Si	Stable	Hexagonal P6 <sub>3</sub> /mmc (194)	a = 1.23 nm c = 2.62 nm
Al <sub>4</sub> Fe <sub>2</sub> Si		Hexagonal P6 <sub>3</sub> /mmc (194)	a = 0.7509 nm c = 0.7594 nm
Al <sub>2</sub> FeSi		Cmmm (67)	a = 0.7995 nm b = 1.5162 nm c = 1.5221 nm
AlFe <sub>2</sub> Ti		Fm -3 m (225)	a = 0.5879 nm
Al <sub>8</sub> FeMg <sub>3</sub> Si <sub>6</sub>		Sp -6 2m (189)	a = 0.662 nm c = 0.792 nm $\gamma = 120^\circ$
AlFe <sub>2</sub> Ni		Fm -3 m (225)	a = 0.5758 nm
Al <sub>2</sub> FeNi		(221)	a = 0.2883 nm

**Appendices A (Continued)**

Phase	State	Bravais Lattice & Space Group	Lattice Parameter
AlFe <sub>2</sub> V		Fm -3 m (225)	a = 0.5761 nm
Al <sub>2</sub> Fe		P1 (1)	a = 0.4878 nm b = .6461 nm c = 0.8800 nm $\alpha$ =91.75 $\beta$ =73.27 $\gamma$ =96.89
AlFe		Pm -3 m(221)	a = 0.2908 nm
Al <sub>7</sub> Fe <sub>3</sub> Ni <sub>30</sub>		(221)	a = 0.3596 nm
AlFe <sub>2</sub>		Fd -3 m(227)	a = 0.7355 nm
AlFe <sub>3</sub>		Fm -3 m(225)	a = 0.58 nm
AlFe <sub>4</sub>		(229)	a = 0.2932 nm

***Appendices B: Routine for quantitative analysis of Fe intermetallic particles***

001 Grab  
002 Load Image '#' with Bitplanes  
    File: #.tif  
    Path: C:\Documents and Settings\Duygu Kocaefe\My Documents  
    \gaofeng\quantification\De simulator 5657\570 Ni cold mount\p4  
003 Clear => All  
004 Color Threshold -> BPL1  
    Hue: start = 251? delta = 359?  
    Saturation: 0%..99%  
    Intensity: 98..196  
    Pause On Run  
005 Pause Edit Draw BPL1  
    complete phases line  
006 Pause Edit Lasso BPL1  
    complete phases lasso  
007  
008 ' choose Al<sub>m</sub>Fe  
009 Hide => All  
010 Pause Edit Lasso BPL2  
    Choose Al<sub>m</sub>Fe  
011 (BPL1 AND BPL2) -> BPL2  
012 (BPL1 DIFF BPL2) -> BPL1  
013  
014 ' choose Al<sub>6</sub>Fe  
015 Hide => All  
016 Show => BPL2  
017 Pause Edit Lasso BPL3  
    Choose Al<sub>6</sub>Fe  
018 (BPL1 AND BPL3) -> BPL3  
019 (BPL1 DIFF BPL3) -> BPL1  
020  
021 ' choose Al<sub>3</sub>Fe  
022 Hide => All  
023 Show => BPL2, BPL3  
024 Pause Edit Lasso BPL4  
    Choose Al<sub>3</sub>Fe  
025 (BPL1 AND BPL4) -> BPL4  
026 (BPL1 DIFF BPL4) -> BPL1  
027  
028 ' choose Al<sub>8</sub>Fe<sub>2</sub>Si  
029 Hide => All  
030 Show => BPL2, BPL3, BPL4  
031 Pause Edit Lasso BPL5

Choose Al<sub>7</sub>Fe<sub>2</sub>Si  
 032 (BPL1 AND BPL5) -> BPL5  
 033 (BPL1 DIFF BPL5) -> BPL1  
 034  
 035 ' choose AlFeNi  
 036 Hide => All  
 037 Show => BPL2, BPL3, BPL4, BPL5  
 038 Pause Edit Lasso BPL6  
 Choose AlFeNi  
 039 (BPL1 AND BPL6) -> BPL6  
 040 (BPL1 DIFF BPL6) -> BPL1  
 041 Field Measures (BPL2) -> FLDM1  
     Perimeter  
     Area Percent  
     Count  
     Density  
 042 Field Measures (BPL3) -> FLDM2  
     Perimeter  
     Area Percent  
     Count  
     Density  
 043 Field Measures (BPL4) -> FLDM3  
     Perimeter  
     Area Percent  
     Count  
     Density  
 044 Field Measures (BPL5) -> FLDM4  
     Perimeter  
     Area Percent  
     Count  
     Density  
 045 Field Measures (BPL6) -> FLDM5  
     Perimeter  
     Area Percent  
     Count  
     Density  
 046  
 047 Square Grid 1x1 -> BPL12  
     Overall Grid Dimensions  
     760 x 572 pixels  
     1986 x 1497  
 048 Transfer (BPL2 SEL BPL12) -> None  
 049 Transfer (BPL3 SEL BPL12) -> None  
 050 Transfer (BPL4 SEL BPL12) -> None

051 Transfer (BPL5 SEL BPL12) -> None  
052 Transfer (BPL6 SEL BPL12) -> None  
053 Object Measures (BPL2, 3, 4, 5, 6) -> OBJM6  
Area  
Perimeter  
Length  
Feret Average  
Aspect Ratio  
End of fields

## References

---

1. "Metals Handbook", 10th ed., Vol. 2, ASM, 1990, p. 62.
2. E.F. Emley, *Int. Met. Rev.*, June 1976, 206, p.75.
- 3 ASM Handbook Volume 9: Metallography and Microstructures(2004).
- 4 . X.-G. Chen, "Growth Mechanisms Of Intermetallic Phases In DC Cast AA1XXX Alloys", *Light Metals*, 1998, 1071-1076.
5. Celil A. Aliravci, John E. Gruzleski and M. ö. Pekgülleryüz, "Calculation of Phase Diagrams and Verification of the Eutectic Temperature for the Solidfication of Metastable Al-Fe Phases in DC-cast Aluminium Alloys", In: *Proceedings of the 4th Decennial international conferrnce on solidification processing*, Sheffield, July 1997.
- 6 . P. Skjerpe, "Solidification structure and primary Al-Fe-Si particles on direct-chilled-cast aluminium alloys", *Ultramicroscopic* 22 (1987) 239-250.
- 7 . Katgerman et al, "Modeling of DC Casting of Aluminium Alloys," in *production, Refining , Fabrication and recycling of Light metals*, *Proc. 29th Annual Conf. of Metallurgists of CIM*, Hamilton, Ont., Pergamon, pp 96-110(26-30 Aug., 1990).
- 8 Westengen, H., "strusture inhomogeneities in direct chill cast sheet ingots of commerical purity aluminium", *Aluminium*, Jahrg (1982-7), 398-401.
- 9 Emley, E.F., "Continuous Casting, " *Int.Met.Rev.*, #206, pp 75-115 (June 1976).
- 10 Ceil A. Aliravic et all, "A thermodynamic study of metastable Al-Fe phase formation in direct chill (DC)-cast aluminium alloy ingots", *Light Metals* (1998), 1381-1389.
- 11 Trond Furu and Hans Erik Vatne, "Effect of as-cast microstructure and subsequent

---

processing on banding in rolled Al-sheets”, *Light Metals*, (1999), 749-754.

12 X.-G. Chen, “Effect of grain refiners on intermetallic phases in AA1XXX simulated DC casting”, *Light Metals*, 1999, 803-809.

13 S.J. Maggs et al, “The effect of trace elements on intermetallic phase selection in simulated DC castings”, *Light Metals*, 1995, 1039-1047.

14 M. W. Meredith et al, “The effect of grain refining additions on intermetallic selection in dilute aluminium alloys”, *Light Metals*, 1998, 977-982.

15 John Granfied et Johun A. Taylor, “The impact of raising Ni and V impurity levels in smelter grade aluminium and potential control strategies”, *Aluminium Cast House Technology*, 2009, 129-136.

16 S. Brusehaug, D. Porter and O. Vorren, “The effect of Process Parameters on the fir-tree strucrure in DC-cast rolling ingots”, proceedings of the 8th International Leichtmetalltagung, Leoben-Wien, (1987), 472-476.

17 Belov, N.A. et all, *Iron in Aluminium Alloys: Impurity and Alloying Element* 2002: Tayor and Francis.

18 Westengen, H., ”strusture inhomogeneities in direct chill cast sheet ingots of commerical purity aluminium”, *Aluminium*, Jahrg (1982-7), 398-401.

19 Langsrud, Y., “The use of phase diagrams for calculating Solidification Paths,” in user aspects of phase diagrams, ed. Hayes, F.H., the institute of metals, London, pp. 99-100 (1991).

20 Rhines, F.N., *Phase diagrams in metallurgy: Their development and application*, McGraw-Hill Book, Co., N.Y. (1956).



- 
- 21 Mondolfo, L.F., Aluminium Alloys: Structure and Properties, Butterworths (1976)
- 22 Dix EH, Heath AC. Trans AIME 1928; 76:164.
- 23 Philips HWL, Varley PC. J Inst Met 1943; 69:317.
- 24 Griger, A., Stefaniay, V., Lendvai, A., and Turmezey, T., "Possible modification of cast Structure by continues casting technology in AlFeSi alloys – parts III: Intermetallic phases," Aluminium, vol. 65, no. 10, pp. 1049-1056 (1989).
- 25 Y. J. Li and L. Arnberg, "Solidification structures and phase selection of iron-bearing eutectic particles in a DC-cast AA5182 alloy", Acta Materialia, Volume 52, Issue 9, 17 May 2004, Pages 2673-2681
- 26 M. V. Kral, H. R. McIntyre and M. J. Smillie, "Identification of intermetallic phases in a eutectic Al–Si casting alloy using electron backscatter diffraction pattern analysis", Scripta Materialia, Volume 51, Issue 3, August 2004, P215-219.
- 27 Langsrud, Y., "silicon in commercial Aluminium Alloys – what becomes of it during DC-Casting?" in Effect of Iron and Silicon in Aluminium and its Alloys, Key Eng. Mat., vols. 44 & 45, pp 95-116 (1990)
- 28 Villars, P. and Calvert, L.D., Pearson's Handbook of Crystallographic Data for Intermetallic phases, ASM, Metals Park Ohio (1991)
- 29 Skjerpe. P, "AN ELECTRON-MICROSCOPY STUDY OF THE PHASE AL<sub>3</sub>FE" BLACKWELL SCIENCE LTD 1987 JOURNAL OF MICROSCOPY-OXFORD 148: 33-50.
- 30 P. Skjerpe, "Intermetallic Phases Formed during DC-Casting of an Al-0.25 Wt Pct

---

Fe-0.13 Wt Pct Si Alloy”, Met. Trans. A,18A (1987), 189-200.

31 Turmezey, T et al, “AlFeSi phases in Aluminium,” in Effect of Iron and Silicon in Aluminium and its Alloys, Key Eng. Mat., vols. 44 & 45, pp 57-68 (1990)

32 P. Skjerpe, “Structure of AlmFe”, Acta Cryst., vol. B44, pp 480-486 (1988).

33 H. Wenstengen, “Formation of Intermetallic Compounds During DC Casting of a Commerical Al-Fe-Si alloy”, Z. Metallkde. 73 (1982), 360-368.

34 P. Skjerpe, “Intermetallic Phases Formed during DC-Casting of an Al-0.25 Wt Pct Fe-0.13 Wt Pct Si Alloy”, Met. Trans. A,18A (1987), 189-200.

35 Turmezey T, Stefaniay V, Griger A, In: internation workshop on the effect of iron and silicon aluminium and its alloy, May 1989 Balatonfured, Hungary, 57. Zurich, Switzerland: Trans Tech Publ.; 1990.

36 T. Turmezey et al., “Effect of Iron and Silicon in Aluminium and its Alloys”, Key Engineering Materials, 44-45, 57 (1991)

37 B. Dutta, M. Rettenmayr, “Effect of cooling rate on the solidification behaviour of Al-Fe-Si alloys,” Materials Science and Engineering A, Volume 283, Issues 1-2, 15 May 2000, Pages 218-224.

38 D. Panahi et all, “Influence of cooling rate and composition on formation of intermetallic phases in solidifying Al-Fe-Si melts,” Canadian Metallurgical Quarterly Volume 50, Issue 2, April 2011, Pages 173-180.

39 P. Skjerpe, “Intermetallic Phases Formed during DC-Casting of an Al-0.25 Wt Pct Fe-0.13 Wt Pct Si Alloy”, Met. Trans. A,18A (1987), 189-200.

40 S. Asami T. Tanaka, and A. Hideno, "Fir-Tree Structure in DC Cast fagots of Al-

---

Mg-Fe-Si Alloy", Journal of Japan Institute of Light Metals, 1978, vol. 28, pp. 321-27.

41 H. Kosuge and I. Mizukami, "Behavior of Fir-Tree Structure in Al-Fe-Si Alloy Ingots Soaking at Elevated Temperatures", Journal of Japan Institute of Light Metals, 1972, vol. 22, pp. 437-44.

42 R. M. Young and T. Clyne, "An Al-Fe Intermetallic Phase Formed During Controlled Solidification", Scripta Metallurgica, 1981, vol. 15, pp. 1211-16

43 I. Miki, H. Kosuge, and K. Nagahama, "Supersaturation and Decomposition of Al-Fe Alloys During Solidification", Journal of Japan Institute of Light Metals, 1975, vol. 25, pp. 1-9.

44 L. Backreud, "Kinetic aspects of the solidification of binary and ternary alloy systems," Jernkontorets Annaler, vol. 152, pp. 109-138 (1968).

45 Langsrud, Y., "silicon in commercial Aluminium Alloys – what becomes of it during DC-Casting?" in Effect of Iron and Silicon in Aluminium and its Alloys, Key Eng. Mat., vols. 44 & 45, pp 95-116 (1990)

46 B. Cantor, K. O'Reilly, "Solidification and Casting", Mater. Sci. and Eng: (UK, IOP Publishing Ltd, 2003), P 7-9.

47 D.A. Granger: Microstructure control in ingots of aluminum alloys with an emphasis on grain refinement, in Light Metals, edited by B.J. Welch (TMS, Warrendale, PA, 1998), pp. 941–952.

48 CM. Allen, K.A.Q. O'Reilly, P.V. Evans, and B. Cantor, "The Effect of Vanadium and Grain Refiner Additions on the Nucleation of Secondary Phases in 1XXX Al

---

Alloys", *Acta Materialia*, 1999, vol. 47, pp. 4387-403.

49 Klimek. L, "Phases identification by means of EBSD method – New possibilities of materials researches", *Archives of metallurgy and materials* Vol. 53(2008), num. 1, pg:151-155.

50 S. Kikuchi (1928). "Diffraction of Cathode Rays by Mica". *Japanese Journal of Physics* 5: 83–96

51 M. V. Kral, H. R. McIntyre and M. J. Smillie, "Identification of intermetallic phases in a eutectic Al–Si casting alloy using electron backscatter diffraction pattern analysis", *Scripta Materialia*, Volume 51, Issue 3, August 2004, P215-219

52 C. MAURICE & R. FORTUNIER, "A 3D Hough transform for indexing EBSD and Kossel patterns", *Journal of Microscopy*, Vol. 230, Pt 3 2008, pp. 520–529.

53 Kral, M.V. , McIntyre, H.R., Smillie, M.J., "Identification of intermetallic phases in a eutectic Al-Si casting alloy using electron backscatter diffraction pattern analysis", *Scripta Materialia* Volume 51, Issue 3, August 2004, Pages 215-219 .

54 Kral, M.V, "A crystallographic identification of intermetallic phases in Al-Si alloys", *Materials Letters* Volume 59, Issue 18, August 2005, Pages 2271-2276 .

55 Y.J. Li, L. Arnberg, "Solidification structures and phase selection of iron-bearing eutectic particles in a DC-cast AA5182 alloy", *Acta Materialia* Volume 52, Issue 9, 17 May 2004, Pages 2673-2681.

56 Y.J. Li, L. Arnberg, "A eutectoid phase transformation for the primary intermetallic particle from Al<sub>m</sub>(Fe,Mn) to Al<sub>3</sub>(Fe,Mn) in AA5182 alloy", *Acta Materialia* Volume 52, Issue 10, 7 June 2004, Pages 2945-2952 .

- 
- 57 C. B. Walker and M. Marezio, *Acta Met.*, 1959, 7, 769.
- 58 Gokhale AM (1990) in: Voort G (ed) *ASM handbook*, vol. 9, the materials information society OH, p 431.
- 59 C.M. Allen, K.A.Q'Reilly, B. Cantor, P.V. Evans, "Intermetallic phase selection in 1xxx Al-alloys", *Progress in Materials Science* 43 (1998), 89-170.
- 60 Mondolfo, L.F., *Aluminium Alloys: Structure and Properties*, Butterworths (1976).
- 61 Black, P.J., "The structure of  $Al_3Fe$  - I," *Acta Cryst.*, Vol. 8, pp.43-48 (1955).
- 62 John Granfield et John A. Taylor, "The impact of raising Ni and V impurity levels in smelter grade aluminium and potential control strategies", *Aluminium Cast House Technology*, 2009, 129-136.
- 63 Mannweiler, U., et al., High vanadium Venezuelan petroleum coke, a raw material for the aluminium industry?, *Light Metals: Proceedings of Sessions, AIME Annual Meeting* (Warrendale, Pennsylvania), 1989, Metallurgical Soc of AIME, 449-454
- 64 Vogt, F., et al., A preview of anode coke quality in 2007, *TMS Light Metals*, 2004, 489-493. CM. Allen, K.A.Q. O'Reilly, P.V. Evans, and B. Cantor, "The Effect of Vanadium and Grain Refiner Additions on the Nucleation of Secondary Phases in 1XXX Al Alloys", *Acta Materialia*, 1999, vol. 47, pp. 4387-403.
- 65 CM. Allen, K.A.Q. O'Reilly, P.V. Evans, and B. Cantor, "The Effect of Vanadium and Grain Refiner Additions on the Nucleation of Secondary Phases in 1XXX Al Alloys", *Acta Materialia*, 1999, vol. 47, pp. 4387-403.
- 66 Dong, Liang and Howard, Jones, "Effect of growth velocity on growth

---

temperature of the Al-Al<sub>3</sub>Fe and Al-Al<sub>6</sub>Fe eutectics”, Z. Metallkd. Volume 83, Issue 4, April 1992, Pages 224-226.